Mathematisches Forschungsinstitut Oberwolfach

Report No. 4/2019

DOI: 10.4171/OWR/2019/4

# Tomographic Inverse Problems: Theory and Applications

Organized by
Martin Burger, Erlangen
Bernadette Hahn, Würzburg
Eric Todd Quinto, Medford

27 January – 2 February 2019

Abstract. This was the tenth Oberwolfach conference on the mathematics of tomography. The field rests on the interplay between the theoretical and applied; practical questions lead to new mathematics and pure mathematics motivates new algorithms. This workshop encompassed classical areas such as X-ray computed tomography (CT) as well as new modalities and applications such as dynamic imaging, Compton scattering tomography, hybrid imaging, optical tomography or multi-energy CT and addressed inter alia the use of methods from machine learning.

*Mathematics Subject Classification (2010):* 44A12 Radon transforms, 92C55 Biomedical Imaging, 65Rxx Numerical analysis, 86A15 Seismology, 44XX Integral transforms.

## Introduction by the Organizers

Tomography is the broad field in which indirect data are used to image the internal properties of objects. Such problems are inverse problems because they require one to find what created the indirect data–to "invert" the data to characterize the object. The field has revolutionized diagnostic medicine and industrial nondestructive evaluation, allowing doctors to find tumors and map metabolism noninvasively, scientists to analyze molecular structures and engineers to detect damages inside of objects nondestructively.

Because of its connection to the real world, the field draws on science and engineering to acquire and model the data. It further draws on deep pure mathematics and numerical analysis to interpret this data and image the objects. Mathematical models describe the connection between the data and the desired properties of the object. For example, in classical X-ray computed tomography (CT), X-ray data

correlate with a mathematical model using line integrals–the Radon transform–of the density. In order to extract the desired properties from a given data set, regularization strategies have to be developed, i.e., the underlying inverse problems has to be solved. Deep pure mathematics has been fundamental to the field from the beginning and this strong interplay between the pure and the applied is one of the strengths of the field.

The first Oberwolfach workshop in 1980, in which pioneers in the field including Frank Natterer and Nobel Laureate Allan Cormack laid out the important problems of the time, was essential for the growth of the field. Decades after the successful integration of X-ray CT in everyday life, tomography is still a vibrant research field. Exploiting additional physical effects and engineering advances for imaging requires new mathematical models and numerical solution schemes. On the other hand, important problems are still unsolved even for the classical CT modalities.

This year's workshop, the tenth Oberwolfach workshop on tomography, brought together 53 participants from Europe and Asia as well as North and South America (including 17 women). Their expertise covered a broad range of areas from pure mathematics, numerical analysis and practical applications in medicine, science and industry. Besides international experts and young scientists, the group of participants included 10 graduate students whose talks were especially effective to introduce these up-coming new researchers to the field. Thus, in every aspect, this has been a diverse workshop. In particular, the discussions and the talks reflected the high quality of the young mathematicians in the field.

Several novel imaging modalities and their underlying inverse problems were presented and discussed at the conference, including terahertz tomography, superresolution imaging with internal sources, adaptive optics, magnetic particle imaging, magnetorelaxometry imaging or Compton scattering tomography (CST). In all of these cases, as scanners collect data in new ways, new reconstruction methods are required and new mathematics must be developed. CST, for instance, exploits the spectrum of the detected radiation as a source of information. Irradiating the body by photons of two or more energies- so called multi-energy imaging - brings up new issues which were addressed in several talks, for instance the problem of correlating the different types of tissues that are measured by the different energies, especially when they are obtained by different scans. A similar issue plays a role in multi-modality imaging for which a novel reconstruction approach based on similarity measures has been presented at the conference.

Vector tomography, seismic tomography, electrical impedance tomography and sonic reflection imaging were further among the discussed modalities. Speakers presented new models, inversion formulas or stable algorithms to solve the underlying inverse problems as well as potential new applications.

Limited data problems are among the earliest CT problems, such as limited angle X-ray CT. However, many general limited data problems constitute unsolved challenges in the field; standard reconstruction algorithms can create artifacts and

blur parts of the objects. Speakers used a priori information to create stable reconstruction algorithms or methods from microlocal analysis to explain the arising issues and guide the improvement of standard algorithms.

Another challenge involves imaging moving objects (e.g. breathing patients, flying insects, or tracking living cells) since the standard models and reconstruction techniques neglect the time-dependency during data acquisition. Several talks addressed related issues such as characterizing the resulting resolution, computational methods for large-scale problems or developing algorithms to compensate for the motion.

A big challenge in many modern imaging problems is to derive a mathematical model which accurately includes all physical factors (attenuation, motion, etc.) and which is easily invertible in the reconstruction step. Thus, data driven object identification and learning methods seem promising strategies in the field of tomography. These methods are used, for example, in electron microscope tomography, and they allow researchers to see molecular structures and where challenges include extremely noisy data and identifying objects among similarly shaped ones. Several speakers gave insights into various potential applications of machine learning techniques in the context of tomography and inverse problems while dealing with their advantages and weaknesses and presenting open problems.

In conclusion, the workshop reflected the current research areas related to tomography and demonstrated the potential and vibrancy of the field. The discussions among the participants stimulated a cross-fertilization among the different disciplines and we expect that joint research activities increase in these areas over the next years because of this.

*Acknowledgement:*
The organizers thank Prof. Dr. Huisken and the staff of the Mathematiches Forschungsinstitut Oberwolfach for creating a perfect environment to do serious mathematics. We thank the MFO for their efficient and very helpful organization that made the conference go smoothly and allowed us to focus on the mathematics. The MFO and the workshop organizers would like to thank the U.S. National Science Foundation for supporting the participation of junior researchers in the workshop by grant DMS-1641185. Lastly, we thank the participants themselves for sharing their mathematics and helping create a lively and stimulating workshop.

## Workshop: Tomographic Inverse Problems: Theory and Applications

## Table of Contents

# Abstracts

## On reconstruction of functions with discontinuities from discrete tomographic data

Alexander Katsevich

### 1. Introduction

In this talk we consider the question:

- *Why and how well does tomographic reconstruction from discrete data work?*

The question is easier if the function $f$ to be reconstructed is sufficiently smooth. It is harder if $f$ is not smooth, e.g. has jump discontinuities. The question has two parts:

(1) What reconstruction looks like near the singularities of $f$?
(2) What is the effect of "remote" singularities?

The accuracy of inversion from discrete data is usually studied using sampling theory. Most of the known results apply only in the classical settings: 2D Radon transform, parallel and fan beam data. See papers by F. Natterer, A. Faridani, L. Desbat, S. Izen, V. Palamodov, A. Rieder and others [1–3, 6, 8, 10, 14]. On the other hand, in many practically relevant situations the classical sampling theory is impossible to apply. For example, no sampling theory is available for cone beam CT with a complicated source trajectory and for scanning of a dynamic object. Interesting first results about the resolution of dynamic 2D tomography were obtained by B. Hahn [5].

Frequently, we are less interested in how the reconstructed image approximates the original object in some global norm. Instead, we would like to know how accurately and with what resolution the singularities of the original object are reconstructed. In this talk we will obtain the behavior of the reconstructed image in a neighborhood of edge singularity of the object. This neighborhood is shrinking appropriately as the sampling rate increases. We call it *transition behavior or edge response*. Both 2D (static and dynamic) and 3D cases (static) are considered. This part of the talk follows the paper [7].

A closely related question is why can we accurately reconstruct functions with discontinuities at all? The question turns out to be nontrivial. In 2D, convergence of reconstruction algorithms in the case of objects with discontinuities has been studied in the mid-80's and 90's by Gonchar, Palamodov, and Popov [4, 11–13]. We explore this question in 3D. This leads to a surprising connection with the theory of uniform distribution [9].

## 2. Analysis of reconstruction in 3D

The 2D case is described in detail in [7], so here we report about the ongoing research in the 3D case. The results reported here are provisional. The Radon transform of $f$ is given by $\hat{f}(\alpha, p) = \int_{\alpha \cdot x = p} f(x)dx$, where $dx$ is the area element on the plane $\Pi(\alpha, p) := \{x \in \mathbb{R}^3 : \alpha \cdot x = p\}$. The discrete data are $\hat{f}(\alpha_i, p_j),\ p_j = \epsilon j,\ j \in \mathbb{Z}$, where $i \in \mathbb{N}$, $i \leq O(\epsilon^{-2})$, is the index that enumerates the measured directions $\alpha_i \in S^2$. Let $\varphi$ be an interpolating kernel, which satisfies:

A1. $\varphi$ is exact up to the order 2, i.e.

$$\sum_{j \in \mathbb{Z}} j^m \varphi(t - j) = t^m, \quad 0 \leq m \leq 2,\ t \in \mathbb{R},$$

A2. $\varphi$ is compactly supported,
A3. The derivatives $\varphi^{(m)}$, $1 \leq m \leq 3$, exist,
A4. $\varphi^{(3)}$ is piecewise continuous with finite one-sided limits,
A5. $\int \varphi(t)dt = 1$.

The discrete inversion formula is given by

$$f_\epsilon(x) = -\frac{1}{8\pi^2} \sum_i c_i\ (\partial/\partial p)^2 \hat{f}_\epsilon(\alpha_i, p)\Big|_{p=\alpha_i \cdot x},$$

$$\hat{f}_\epsilon(\alpha_i, p) := \sum_{j \in \mathbb{Z}} \hat{f}(\alpha_i, \epsilon j)\varphi\left(\frac{p - \epsilon j}{\epsilon}\right),$$

where $c_i$ are integration weights.

Pick a point $x_0 \in S := \text{singsupp} f$, and suppose $S$ is a smooth surface with positive principal curvatures in a neighborhood of $x_0$. Let $\Theta_0$ be the unit vector normal to $S$ at $x_0$ pointing "inward". Consider the point $x_h := x_0 + \epsilon h \Theta_0$, where $h$ varies over a bounded set. Denote $\rho_0 := \lim_{\delta \to 0^+} (f(x_0 + \delta\Theta_0) - f(x_0 - \delta\Theta_0))$.

**Theorem 1.** *For a generic $x_0$, one has*

$$f_\epsilon(x_h) \to const_\epsilon + \rho_0 \int_{-\infty}^{h} \varphi(s)ds,\ \epsilon \to 0,\ \textit{and}\ \int_{-\infty}^{h} \varphi(s)ds \to \begin{cases} 0, & h \to -\infty, \\ 1, & h \to +\infty. \end{cases}$$

The hardest part of the proof is to show that "remote" singularities of $f$ do not contribute to the transition behavior. Suppose $S$ is tangent to $\Pi(\Theta_0, p_0(\Theta_0))$ at some $z_0$, $z_0 \neq x_0$. The function $p_0(\alpha)$ is defined locally by the condition that $\Pi(\alpha, p_0(\alpha))$ is tangent to $S$. Consider one generic situation: $S$ is strictly convex near $z_0$ and its Gaussian curvature is positive. We prove that the singularity at $z_0$ does not contribute to the transition behavior of the reconstruction at $x_0$. More precisely, we prove that in the limit $\epsilon \to 0$ the discretized reconstruction formula gives the same result as the exact reconstruction formula.

Generically, the equation $\alpha \cdot x_0 = p_0(\alpha)$ determines a piecewise smooth curve, which we denote $\Gamma$. Clearly, $\Theta_0 \in \Gamma$. To leading order, the contribution of the remote singularity to the image reconstructed at $x_0$ contains the following key

term:

$$\sum_{\mathrm{dist}(\alpha_i,\Gamma)=O(\epsilon)} \psi\left(\left\{\frac{\alpha_i\cdot x_0}{\epsilon}\right\}, \frac{\alpha_i\cdot x_0 - p_0(\alpha_i)}{\epsilon}\right),$$

where $\psi$ is a sufficiently smooth function, which is expressed in terms of the interpolation kernel $\varphi$. The sum is over an $O(\epsilon)$-wide strip around $\Gamma$. In order to get an expected answer, we need to prove that the distribution of grid nodes inside the strip is asymptotically uniform (as $\epsilon \to 0$). This is not easy to do, since the thickness of the strip is $O(\epsilon)$. The result does hold, i.e. the distribution of grid nodes inside the strip is indeed asymptotically uniform. The proof uses methods from the theory of uniform distribution (see, e.g. [9]). It appears that uniform distribution of nodes in some special domains is a key reason why we can accurately reconstruct functions with discontinuitiues.

## References


[1] A. Caponnetto and M. Bertero, *Tomography with a finite set of projections: singular value decomposition and resolution*, IEEE Transactions on Information Theory, **13** (1997), 1191–1205.

[2] L. Desbat, *Efficient sampling on coarse grids in tomography*, Inverse Problems,**9** (1993), 251–269.

[3] A. Faridani, *Sampling theory and parallel-beam tomography*, in Sampling, wavelets, and tomography, Birkhauser, Boston, MA. Applied and Numerical Harmonic Analysis **63** (2004), 225–254.

[4] S. I. Gonchar, *Convergence of computational algorithms for recovering discontinuous functions from the Radon transform*, Russian Mathematical Surveys, **41** (1986), 205–206.

[5] B. N. Hahn, *Null space and resolution in dynamic computerized tomography*, Inverse Problems, **32** (2016), Article ID: 025006 (21 pp).

[6] S. H. Izen, *Sampling in Flat Detector Fan Beam Tomography*, SIAM Journal on Applied Mathematics, **72** (2012), 61–84.

[7] A. Katsevich, *A local approach to resolution analysis of image reconstruction in tomography*, SIAM Journal on Applied Mathematics, **77** (2017), 1706–1732.

[8] H. Kruse, *Resolution of Reconstruction Methods in Computerized Tomography*, SIAM Journal on Scientific and Statistical Computing, **10** (1989), 447–474.

[9] L. Kuipers and H. Niederreiter, *Uniform Distribution of Sequences*. Dover Publications, Mineola, NY, 2006.

[10] F. Natterer, *Sampling in Fan Beam Tomography*, SIAM Journal on Applied Mathematics, **53** (1993), 358–380.

[11] V. P. Palamodov, *Some mathematical aspects of 3D X-ray tomography.* Proceedings of the Conference: Tomography, impedance imaging, and integral geometry (South Hadley, MA, 1993. Lectures in Applied Mathematics, Amer. Math. Soc., Providence, RI. **30** (1994), 199 – 210.

[12] D. A. Popov, *On convergence of a class of algorithms for the inversion of the numerical Radon transform*. Mathematical problems of tomography, Amer. Math. Soc. Translations of Mathematical Monographs, Providence, RI. **81** (1990), 7–65.

[13] D. A. Popov, *Reconstruction of characteristic functions in two-dimensional Radon tomography*, Russian Mathematical Surveys, **53** (1998), 109–193.

[14] A. Rieder and A Schneck, *Optimality of the fully discrete filtered backprojection algorithm for tomographic inversion*, Numerische Mathematik, **108** (2007), 151–175.

## Terahertz tomography as a parameter identification problem

Anne Wald
(joint work with Thomas Schuster)

Terahertz (THz) tomography is a relatively novel imaging technique that is mostly used for the nondestructive testing of dielectric materials such as plastics or ceramics. The goal is to detect defects such as cracks, inclusions, or the moisture content. Another objective is to characterize materials by their physical properties, i.e., their refractive index $n > 0$ as well as their extinction coefficient $\kappa > 0$. These quantities determine the propagation of electromagnetic radiation through the object. The refractive index determines the path along which the rays travel, while the extinction coefficient is responsible for the attenuation of the radiation [1, 6]. Terahertz radiation has a frequency of 0.1 to 10 THz, where $1\,\mathrm{THz} = 10^{12}\,\mathrm{Hz}$.

In THz tomography, the object is scanned with a Gaussian beam in the THz regime. We are interested in reconstructing the complex refractive index $\tilde{n} = n + i\kappa$ of an object from measurements of the resulting electric field of the THz radiation on a circle around the object. We assume that the radiation has a fixed wave number $k_0 > 0$. We let $\Omega \subseteq \mathbb{R}^2$ with $C^1$-boundary and set

$$m : L^\infty(\Omega) \cap L^2_{\mathrm{comp}}(\Omega) \to \mathbb{C},\ m(\mathbf{x}) := 1 - \tilde{n}^2(\mathbf{x}).$$

Then the $z$-component $u_\mathrm{t}$ of total electric field is determined by

$$\Delta u_\mathrm{sc} + k_0^2(1-m)u_\mathrm{sc} = k_0^2 m u_\mathrm{i} \quad \text{in } \Omega, \tag{1}$$

$$\frac{\partial u_\mathrm{sc}}{\partial \mathbf{n}} - ik_0 u_\mathrm{sc} = 0 \quad \text{on } \partial\Omega, \tag{2}$$

$$u_\mathrm{sc} + u_\mathrm{i} = u_\mathrm{t} \quad \text{in } \overline{\Omega}, \tag{3}$$

where $\mathbf{n}$ is the outward normal vector of $\partial\Omega$. The superposition principle (3) states that the total field $u_\mathrm{t}$ is the sum of the incident field $u_\mathrm{i}$ and the scattered field $u_\mathrm{sc}$. We show, see [1], that there is a unique weak solution $u_\mathrm{sc} \in H^1(\Omega)$ of (1), (2) fulfilling

$$\|u\|_{H^1(\Omega)} \le C_1 \|m\|_{L^\infty(\Omega)} \|u_\mathrm{i}\|_{L^2(\Omega)}$$

for a constant $C_1 > 0$. This result yields the well-definedness of the forward operator

$$S : \mathcal{D}(S) \to H^1(\Omega),\ m \mapsto u_\mathrm{t} = u_\mathrm{i} + u_\mathrm{sc},$$

where

$$\mathcal{D}(S) \subseteq \big\{ m \in L^\infty(\Omega) \cap L^2_{\mathrm{comp}}(\Omega) : \|m\|_{L^\infty(\Omega)} \le M,\ \mathrm{Im}(m) \le 0 \big\}$$

for a fixed $M > 0$, $u_\mathrm{i} \in H^1(\Omega)$, and $u_\mathrm{sc}$ is the weak solution of (1), (2).

The operator $S$ is Lipschitz-continuous on $\mathcal{D}(S)$, continuously Fréchet differentiable and fulfills the tangential cone condition

$$\|S(m_1) - S(m_2) - S'(m_1)(m_1 - m_2)\|_{L^2(\Omega)} \le C_3 \cdot \|S(m_1) - S(m_2)\|_{L^2(\Omega)},$$

for $m_1, m_2 \in \mathcal{D}(S)$, where $C_3 = C_3\big(k_0, \Omega, M\big)$, see [1].

During the measurement process, the tomograph, resp. the emitter and receivers, is rotated around the object. For different positions of the tomograph, indicated by $j = 1, ..., J$, the total field $u_\mathrm{t}$ is measured by the $N$ receivers $E_\nu^j$, $\nu = 1, ..., N$, on $\partial\Omega$. By consequence, the incident field $u_\mathrm{i}^j$ depends on the position $j$. The same holds for the scattered and total field and the scattering map $S^j$. Together with linear observation operators $Q^j$ and the trace operator $\gamma : H^1(\Omega) \to L^2(\partial\Omega),\ u \mapsto u|_{\partial\Omega}$, the (nonlinear) forward operator is

$$F = \big(F^1, ..., F^J\big) \,:\, \mathcal{D}(S) \to \mathbb{C}^{N\times J},$$

where

$$\big(F^j(m)\big)_\nu := \big(Q^j\gamma S^j(m)\big)_\nu = \big(Q^j\gamma u_\mathrm{t}^j\big)_\nu = \int_{\partial\Omega} \chi_{E_\nu^j}(\mathbf{x})\gamma u_\mathrm{t}^j(\mathbf{x})\,\mathrm{d}s_\mathbf{x}, \quad \nu = 1, ..., N.$$

The inverse problem of 2D THz tomography thus consists in the reconstruction of $m : \Omega \to \mathbb{C}$ from measurements $y^{j,\delta} \in \mathbb{C}^N$ of the electric field, where

$$F^j(m) = y^j, \quad \|y^{j,\delta} - y^j\| \le \delta, \quad j = 1, ..., J.$$

If $m$ is real-valued, this corresponds to the inverse medium problem, see, e.g., [4].

We use sequential subspace optimization [2] to determine a regularized solution. (Regularizing) Sequential subspace optimization – (RE)SESOP – is an iterative reconstruction technique for linear and nonlinear inverse problems in Hilbert and Banach spaces that yields a regularized solution if only noisy data is available [2, 3, 5]. For a nonlinear problem

$$F(x) = y, \quad F : \mathcal{D}(F) \subseteq X \to Y, \quad \|y - y^\delta\| \le \delta$$

in a Hilbert space setting with solution set $M_{F(x)=y}$, the iteration reads

$$x_{n+1}^\delta = x_n^\delta - \sum_{i\in I_n^\delta} t_{n,i}^\delta F'(x_i^\delta)^* w_{n,i}^\delta,$$

where the parameters $t_{n,i}^\delta$ are calculated such that

$$x_{n+1}^\delta \in \bigcap_{i\in I_n^\delta} H_{n,i}^\delta$$

is the metric projection of the current iterate $x_n^\delta$ onto the intersection of (finitely many) stripes

$$H_{n,i}^\delta := \Big\{ x \in X : \big|\big\langle F'(x_i^\delta)^* w_{n,i}^\delta, x_i^\delta - x\big\rangle - \big\langle w_{n,i}^\delta, F(x_i^\delta) - y^\delta\big\rangle\big| \\ \le \|w_{n,i}^\delta\| \left(c_\mathrm{tc}\big(\|R_i^\delta\| + \delta\big) + \delta\right) \Big\} \ \supseteq M_{F(x)=y}.$$

The parameters $w_{n,i}^\delta \in Y$ are chosen such that we obtain a descent property

$$\|z - x_{n+1}^\delta\|^2 \le \|z - x_n^\delta\|^2 - C\big(\|F(x_n^\delta) - y^\delta\|, \delta\big) \quad \text{for } z \in M_{F(x)=y}.$$

The iteration is stopped by the discrepancy principle.

The choices $w_{n,i}^{\delta} := F(x_i^{\delta} - y^{\delta})$ and $n \in I_n^{\delta}$ yield a regularization method. For $I_n^{\delta} := \{n\}$, we obtain a Landweber-type method with a regulation of the step width.

## References


[1] A. Wald and T. Schuster, *Tomographic terahertz imaging using sequential subspace optimization*, in New Trends in Parameter Identification, Springer Series Trends in Mathematics (2018)

[2] A. Wald and T. Schuster, *Sequential subspace optimization for nonlinear inverse problems*, Journal of Inverse and Ill-posed Problems **25** 1 (2017), 99–117.

[3] A. Wald, *A fast subspace optimization method for nonlinear inverse problems in Banach spaces with an application in parameter identification*, Inverse Problems **34** 8 (2018), 085008

[4] G. Bao and P. Li, *Inverse medium scattering for the Helmholtz equation at fixed frequency*, Inverse Problems **21** (2005), 1621 – 1641

[5] F. Schöpfer, T. Schuster, and A.K. Louis, *Metric and Bregman projections onto affine subspaces and their computation via sequential subspace optimization methods*, Journal of Inverse and Ill-posed Problems **15** (2007), 1–28

[6] J. Tepe, T. Schuster, and B. Littau, *A modified algebraic reconstruction technique taking refraction into account with an application in terahertz tomography*, Inverse Problems in Science and Engineering **25** 10 (2017), 1448 – 1473


## Computational Methods for Tomographic Reconstruction

Julianne Chung

Tomographic reconstruction is a classic example of an inverse problem, where measurements are obtained on the exterior of an object (e.g., the human body or the Earth's crust), and one solves an inverse problem for the purpose of estimating the internal structures. This is illustrated in the following figure, where the goal is to reconstruct the image on the left from the observed measurements on the right.

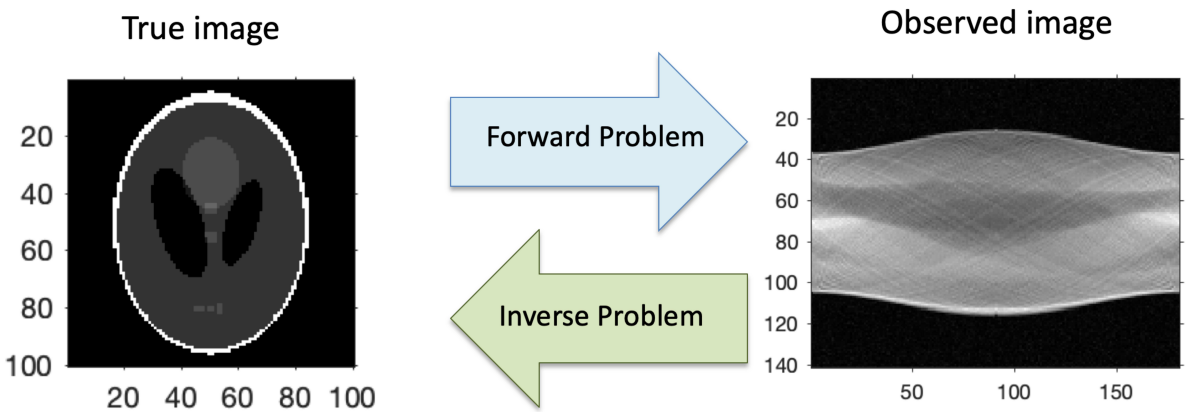


There is a great need for efficient methods that can compute solutions to inverse problems accurately and in real-time. However, the main computational challenges that have hindered large-scale reconstruction and data analysis include ill-posedness of the problem, large parameter dimensions, model inaccuracies, and

regularization parameter selection. In this talk, I describe some *new mathematical and computational tools* for the design, computation, and analysis of solutions to large-scale inverse problems, such as those that arise in tomography.

## 1. Mathematical description

Many tomography problems have an underlying mathematical model that can be represented as $\mathbf{b}_{\text{true}} = F(\mathbf{x}_{\text{true}})$, where $\mathbf{x}_{\text{true}} \in \mathbb{R}^n$ represents the desired parameters or image, $\mathbf{b}_{\text{true}} \in \mathbb{R}^m$ represents perfectly measured (error-free) data, and the functional $F(\cdot) : \mathbb{R}^n \to \mathbb{R}^m$ models the forward data acquisition process. In many applications, it is impossible to collect error-free data, and a realistic model of the data collection process is given by

$$\mathbf{b} = F(\mathbf{x}_{\text{true}}) + \boldsymbol{\delta}\,,$$

where $\boldsymbol{\delta} \in \mathbb{R}^m$ represents inevitable errors that arise from measurement error, discretization error, or round-off error. The precise form of $F$ depends on the application, but the inverse problem can be stated as follows.

| **Problem statement** |
|---|
| *Given measured data,* $\mathbf{b} = F(\mathbf{x}_{\text{true}}) + \boldsymbol{\delta}$, *and knowledge of the forward model,* $F(\cdot)$, *the goal is to compute an approximation of* $\mathbf{x}_{\text{true}}$. |

Solving inverse problems is notoriously difficult due to *ill-posedness*, whereby data acquisition noise and computational errors can lead to large changes in the computed solution. By incorporating prior information, *regularization* is a standard approach to modify the problem and overcome the inherent instability of ill-posed problems. Most inverse problems can be formulated as an optimization problem of the form,

$$\min_{\mathbf{x}} \mathcal{J}(\mathbf{b} - F(\mathbf{x})) + \lambda \mathcal{R}(\mathbf{x}) \tag{1}$$

where $\mathcal{J}$ is a loss function, $\mathcal{R}$ is a regularization operator, and $\lambda > 0$ is a regularization parameter that controls the amount of regularization, thereby determining how faithful the modified problem is to the original problem. Consider the simplified case where $\mathcal{J}(\mathbf{r}) = \|\mathbf{r}\|_2^2$ and $\mathcal{R}(\mathbf{x}) = \|\mathbf{x}\|_2^2$. Computing solutions for the least-squares problem can still be challenging if the number of parameters in $\mathbf{x}$ is very large or if $\lambda$ is not known a priori. Other challenges arise if $\mathcal{R}(\mathbf{x})$ incorporates more general prior models or if the forward model $F(\mathbf{x})$ is nonlinear.

## 2. Computational Methods for Reconstruction

In my research, I have developed a range of new methods with solid mathematical theory for solving (1). Here I focus on efficient hybrid projection regularization methods and highlight relevant applications to tomography.

Many of the existing regularization methods can be implemented efficiently if regularization parameter(s) are known *a priori* but fall short of clear strategies for simultaneous parameter selection. My work on iterative hybrid methods combine iterative with direct regularization in an efficient and robust way to achieve the

best properties of both approaches. Consider the linear case where $F(\mathbf{x}) = \mathbf{A}\mathbf{x}$ with $\mathbf{A} \in \mathbb{R}^{m\times n}$ and consider the Tikhonov regularized problem,

$$\min_{\mathbf{x}} \|\mathbf{b} - \mathbf{A}\mathbf{x}\|_2^2 + \lambda\|\mathbf{x}\|_2^2.$$

In [1], my collaborators and I investigated a hybrid LSQR framework and demonstrated the main advantages of hybrid methods, namely requiring only matrix-vector and matrix-transpose-vector multiplications with $\mathbf{A}$, overcoming semiconvergence behavior, and being able to select the regularization parameter automatically. We developed a weighted generalized-cross-validation (WGCV) method for selecting regularization parameters in a hybrid framework.

Algorithmic extensions were described in [2] where we developed a hybrid algorithm based on the generalized Golub-Kahan bidiagonalization to efficiently approximate the solution to

$$\min_{\mathbf{x}} \|\mathbf{b} - \mathbf{A}\mathbf{x}\|_{\mathbf{R}^{-1}}^2 + \lambda\|\mathbf{x}\|_{\mathbf{Q}^{-1}}^2,$$

where $\mathbf{R}$ and $\mathbf{Q}$ are covariance matrices for the noise and prior respectively. More specifically, we described a reformulation so that explicit computation of the square root and inverse of the covariance kernel for the prior covariance matrix is no longer required. Such scenarios arise, for example, in problems where covariance kernels are defined on irregular grids, e.g., those from the Matérn class, and the resulting covariance matrices are only available via matrix-vector multiplication. We proved that iterates are equivalent to LSQR iterates applied to a directly regularized Tikhonov problem, after a transformation of variables, and we provided connections to a generalized singular value decomposition filtered solution.

Then in [3], my collaborators and I considered a Bayesian framework for solving dynamic inverse problems, where the underlying parameters of interest change in time, such that the total number of unknowns is on the order of millions. We showed that incorporating prior information regarding temporal smoothness in algorithms can lead to better reconstructions, but more importantly, we showed that low-rank approximations obtained using the generalized Golub-Kahan bidiagonalization can be used to estimate pixel and voxel-wise solution variances. Other tools for uncertainty quantification are currently being developed [4]. These computational methods have been used to improve reconstructions in computed tomography, photoacoustic tomography, and passive seismic tomography.

## 3. Summary and looking forward

Tomographic reconstruction is an ill-posed inverse problem, and computing reasonable solutions requires regularization to overcome inherent instabilities, good regularization parameters, numerical algorithms, and efficient computational implementations. In my current and ongoing research projects, I am developing methods to address various computational challenges. For example, for problems where many vectors are needed for solution representation, we are developing hybrid projection methods that exploit recycling techniques from numerical linear

algebra to compress and update a given solution space. For massive inverse problems where the data is too large to keep in memory and/or dynamically growing, we are investigating sampled Tikhonov methods for efficient computation. And for problems where training images are readily available, we are developing statistical learning approaches that can be coupled with existing regularization techniques for improved reconstructions.

## References


[1] J. Chung, J. G. Nagy, and D. P. O'Leary. A weighted GCV method for Lanczos hybrid regularization. *Electronic Transactions on Numerical Analysis*, 28:149–167, 2008.

[2] J. Chung and A. K. Saibaba. Generalized hybrid iterative methods for large-scale Bayesian inverse problems. *SIAM Journal on Scientific Computing*, 39(5):S24–S46, 2017.

[3] J. Chung, A. K. Saibaba, M. Brown, and E. Westman. Efficient generalized Golub–Kahan based methods for dynamic inverse problems. *Inverse Problems*, 34(2):024005, 2018.

[4] A. K. Saibaba, J. Chung, and K. Petroske. Quantifying uncertainties in large-scale Bayesian linear inverse problems using Krylov subspace methods. *arXiv preprint arXiv:1808.09066*, 2018.


## Inversion of the star transform


Gaik Ambartsoumian

(joint work with Mohammad Javad Latifi Jebelli)


Let $f(x) \in C_c\left(\mathbb{R}^2\right)$ be a compactly supported continuous function, and let $\gamma$ be a fixed unit vector in the plane.

**Definition 1.** *The divergent beam transform $\mathcal{X}_\gamma$ of $f$ at $x \in \mathbb{R}^2$ is defined as:*

$$\mathcal{X}_\gamma f(x) = \int_0^\infty f(x + t\gamma)\, dt.$$

One can use a linear combination of divergent beam transforms with a set of fixed directions $\gamma_i \in S^1$ and non-zero constants $c_i \in \mathbb{R}$, $i = 1, \ldots, m$ to define the star transform of $f$. Namely,

**Definition 2.** *The star transform $\mathcal{S}$ of $f$ at $x \in \mathbb{R}^2$ is defined as:*

$$\mathcal{S}f(x) = \sum_{i=1}^{m} c_i\, \mathcal{X}_{\gamma_i} f(x) = \sum_{i=1}^{m} c_i \int_0^\infty f(x + t\gamma_i)\, dt.$$

In particular, if $c_1 = \ldots = c_m = 1$, the star transform $S$ puts into correspondence to a given function $f(x)$ its integrals $\mathcal{S}f(x)$ along a two-parameter family of so-called "stars". Each star consists of a union of rays emanating from a common vertex $x$ along fixed directions $\gamma_i$, $i = 1, \ldots, m$ (see Figure 1).

We are interested in the inversion of the star transform $\mathcal{S}$ for an arbitrary (finite) number of rays $m$ and arbitrary non-zero constants $c_i$, $i = 1, \ldots, n$. Such integral-geometric problems appear naturally in relation to single-scattering optical tomography and single-scattering X-ray CT (e.g. see [4, 5, 8, 10]). Particular attention has been drawn to the transforms with $m = 2$ and various choices of

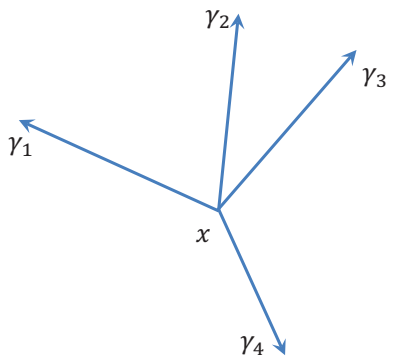


FIGURE 1. A star centered at point $x$ with rays emanating along fixed vectors $\gamma_1, \ldots, \gamma_4$.

constants $c_1$ and $c_2$. In this special case, the integral transform $\mathcal{S}$ is usually called either a *broken ray transform* or a *V-line transform* (e.g. see [1–3, 7, 9]).

While there are multiple interesting formulas and procedures for inversion of the broken ray transform (e.g. see [1–3,7,9]), the star transform for $m \geq 3$ was studied only in [10]. The method presented in that paper is based on Fourier analysis techniques and allows stable inversion of the star transform only for configurations involving odd number of rays.

We present a new exact inversion formula for the star transform $\mathcal{S}$, by establishing a connection between the star transform of $f$ and the Radon transform of $f$. Our inversion method works equally well for configurations with both odd and even number of rays.

For simplicity, the main result below if formulated for the case when $c_1 = \ldots = c_m = 1$. The general case can be treated similarly with minor modifications.

**Theorem 1.** *Let $\mathcal{S} = \sum_{i=1}^{m} \mathcal{X}_{\gamma_i}$ be the star transform and let*

$$q(\psi) = \frac{-1}{\sum_{i=1}^{m} \frac{1}{\langle \psi, \gamma_i \rangle}}.$$

*Then the following is true for any $\psi$ in the domain of $q$:*

$$\mathcal{R}f(\psi, s) = q(\psi) \frac{d}{ds} \mathcal{R}(\mathcal{S}f)(\psi, s),$$

*where $\mathcal{R}$ denotes the (ordinary) Radon transform of a function in $\mathbb{R}^2$. Hence, if $q$ is defined almost everywhere, we can apply $\mathcal{R}^{-1}$ to recover $f$.*

Notice, that for certain configurations the function $q(\psi)$ is not defined for almost every $\psi$. For example, it happens when $m = 4$, $\gamma_1 = -\gamma_3 = (1, 0)$, and $\gamma_2 = -\gamma_4 = (0, 1)$. It is easy to notice that in this case the star transform is not injective.

In the case of $m = 2$ Theorem 1 yields a simple inversion for the broken ray transform.

**Corollary 1.** *An inversion formula for the V-line transform with ray directions* $\gamma_1$, $\gamma_2$ *is given by*

$$f = \mathcal{R}^{-1}\left(\frac{-\langle\psi,\gamma_1\rangle\langle\psi,\gamma_2\rangle}{\langle\psi,\gamma_1\rangle+\langle\psi,\gamma_2\rangle}\frac{d}{ds}\mathcal{R}(\mathcal{S}f)(\psi,s)\right).$$

The detailed proofs of these statements, numerical implementations, and discussion of some other related results will be presented in an article that will be submitted soon for publication.

This work was partially funded by NSF grant DMS 1616564, and Simons Foundation grant 360357.

## References

[1] G. Ambartsoumian and M. J. Latifi Jebelli, *The V-line transform with some generalizations and cone differentiation*, Inverse Problems, **35** 3 (2019), 034003.
[2] G. Ambartsoumian and S. Moon, *A series formula for inversion of the V-line Radon transform in a disc*, Computers & Mathematics with Applications, **66** 9 (2013), pp 1567–1572.
[3] L. Florescu, V. Markel and J. Schotland, *Inversion formulas for the broken ray Radon transform*, Inverse Problems, **27** 2 (2011) 025002.
[4] L. Florescu, J. Schotland and V. Markel, *Single scattering optical tomography*, Physical Review E, **79** 3 (2009), 036607.
[5] L. Florescu, V. Markel and J. Schotland, *Single scattering optical tomography: simultaneous reconstruction of scattering and absorption* Physical Review E, **81** 1 (2010), 016602.
[6] R. Gouia-Zarrad and G. Ambartsoumian, *Exact inversion of the conical Radon transform with a fixed opening angle*, Inverse Problems, **30** 4 (2014), 045007.
[7] A. Katsevich and R. Krylov, *Broken ray transform: inversion and a range condition*, Inverse Problems, **29** 7 (2013), 075008.
[8] R. Krylov and A. Katsevich, *Inversion of the broken ray transform in the case of energy dependent attenuation*, Physics in Medicine & Biology, **60** 11 (2015), pp 4313–4334.
[9] B. Sherson, *Some results in single-scattering tomography*, PhD Thesis, Oregon State University, 2015.
[10] Z. Zhao, J. Schotland and V. Markel, *Inversion of the star transform*, Inverse Problems, **30** 10 (2014), 105001.

## Convergence Rates of First and Higher Order Dynamics for Solving Linear Inverse Problems

Otmar Scherzer

(joint work with Radu Boţ, Guozhi Dong and Peter Elbau)

We consider the problem of solving a linear inverse problem, formulated as solving an operator equation

$$Lx = y, \tag{1}$$

where $L : \mathcal{X} \to \mathcal{Y}$ is a bounded linear operator between (infinite dimensional) real Hilbert spaces $\mathcal{X}$ and $\mathcal{Y}$. If the range of $L$ is not closed, Equation 1 is ill-posed and regularization has to be employed for a stable solution.

In this talk we consider dynamical regularization methods: That is, we approximate the minimum norm solution $x^\dagger$ of Equation 1 by the solution of a dynamical

system at an appropriate time. An established example of such a dynamical regularization method is Showalter's method [6], which consists in calculating the solution of the Cauchy problem

$$\begin{aligned} &\xi'(t) = -L^*L\xi(t) + L^*y \text{ for all } t \in (0,\infty), \\ &\xi(0) = 0. \end{aligned} \tag{2}$$

More recently, second order dynamical systems have been investigated for optimizing **general** convex functionals, see [1, 2, 4, 7]. One motivation for these dynamic equations has been to consider them as time continuous limits of Nesterov's algorithm [5] to explain its fast convergence.

We consider dynamical systems for solving linear ill-posed operator equations by focusing on the particular convex functionals

$$\mathcal{J}(x) = \frac{1}{2}\|Lx - y\|^2. \tag{3}$$

Specifically, we develop a regularization theory to analyse $N$-th order dynamical method of the form

$$\begin{aligned} \xi^{(N)}(t) + \sum_{k=1}^{N-1} a_k(t)\xi^{(k)}(t) &= -L^*L\xi(t) + L^*y \quad \text{for all } t \in (0,\infty), \\ \xi^{(k)}(0) &= 0 \qquad\qquad\qquad\quad \text{for all } k = 0,\dots,N-1, \end{aligned} \tag{4}$$

where $N \in \mathbb{N}$ and $a_k : (0,\infty) \to \mathbb{R}, k = 1,\dots,N-1$, are continuous functions. When $N = 1$ this is Showalter's method. When $N = 2$, and $a_1$ is constant and positive the method is called *heavy ball dynamical method* (HBD). And for $N = 2$ and $a_1 = \frac{b}{t}$, $b > 0$, the analogous method as considered in [1, 2, 4, 7], we call it the *vanishing viscosity flow* (VVF).

In [3] we proved the following convergence rates result and compared it with the literature, see Table 1.

Note that the results from convex analysis (VVD (convex) in Table 1) prove convergence rates of the residuum and not of the solution. The results of (IP) show an improvement of the convergence rates for general convex problems. Actually these results support a conjecture of [7]: "However, from a different perspective, this example suggests that $\mathcal{O}(t^{-b})$ convergence rate can be expected ..."

Moreover, we showed that under classical source conditions even convergence rates for $\|\xi(t) - x^\dagger\|^2$ can be proven. In this case we require source conditions like: There exists some $w \in \mathcal{X}$ such that

$$x^\dagger = (L^*L)^{\frac{\mu}{2}} w. \tag{5}$$

We summarize some results from [3] on regularized dynamical systems when the solution $x^\dagger$ satisfies some source condition in Table 2.

| Method ($t \to \infty$) | $\mathcal{J}(\xi(t)) - \min \mathcal{J}$ | $\|\xi(t) - x^\dagger\|^2$ |
|---|---|---|
| VVD (convex) | $o(t^{-2})$ $(b > 3)$, $\mathcal{O}(t^{-2})$ $(b = 3)$, $\mathcal{O}(t^{-2b/3})$ $(b < 3)$ | – |
| VVD (IP) | $\boldsymbol{o(t^{-2})}$ $\boldsymbol{(b > 2)}$, $\boldsymbol{o(t^{-b})}$ $\boldsymbol{(b \leq 2)}$ | $\boldsymbol{o(1)}$ |
| Showalter | $o(t^{-1})$ | $o(1)$ |
| HBD | $o(t^{-1})$ | $o(1)$ |

TABLE 1. Convergence Rates without Source Conditions. Convergence for VVD from [1, 2, 4, 7] for minimizing general convex functionals $\mathcal{J}$, and results from [3] (IP) for the convex functionals from Equation 3. Analogous results for Showalter and HBD. Results in bold face are from [3].

| Method ($t \to \infty$) | $\mathcal{J}(\xi(t)) - \min \mathcal{J}$ | $\|\xi(t) - x^\dagger\|^2$ |
|---|---|---|
| VVD (IP) [Max Rate] | $\boldsymbol{\mathcal{O}(t^{-2\mu-2})}$ $[\boldsymbol{\mathcal{O}(t^{-b+\epsilon})}]$ | $\boldsymbol{\mathcal{O}(t^{-2\mu})}$ $[\boldsymbol{\mathcal{O}(t^{-b+\epsilon})}]$ |
| Showalter | $\mathcal{O}(t^{-\mu-1})$ | $\mathcal{O}(t^{-\mu})$ |
| HBD | $\mathcal{O}(t^{-\mu-1})$ | $\mathcal{O}(t^{-\mu})$ |

TABLE 2. Convergence rates with source conditions. In the case of VVD, the parameters are restricted to $0 < \mu < \frac{b}{2} - 1$ (and thus $b > 2$) for $\mathcal{J}(\xi(t)) - \min \mathcal{J}$ and $0 < \mu < \frac{b}{2}$ for $\|\xi(t) - x^\dagger\|^2$, which leads to the given maximal rates (for arbitrarily small $\epsilon > 0$). For general convex problems, source conditions, Equation 5, are not known to provide improved convergence rates.

## ACKNOWLEDGMENTS


- RB acknowledges support from the Austrian Science Fund (FWF) within the project I2419-N32 (Employing Recent Outcomes in Proximal Theory Outside the Comfort Zone).
- GD is supported by a MATHEON Research Center project CH12 funded by the Einstein Center for Mathematics (ECMath) Berlin.
- PE and OS are supported by the Austrian Science Fund (FWF), with SFB F68, project F6804-N36 (Quantitative Coupled Physics Imaging) and project F6807-N36 (Tomography with Uncertainties).
- OS acknowledges support from the Austrian Science Fund (FWF) within the national research network Geometry and Simulation, project S11704 (Variational Methods for Imaging on Manifolds) and I3661-N27 (Novel Error Measures and Source Conditions of Regularization Methods for Inverse Problems).

## References

[1] H. Attouch, Z. Chbani, J. Peypouquet, and P. Redont. Fast convergence of inertial dynamics and algorithms with asymptotic vanishing viscosity. *Mathematical Programming. A Publication of the Mathematical Optimization Society*, 168(1–2):123–175, 2018.

[2] H. Attouch, Z. Chbani, and H. Riahi. Combining fast inertial dynamics for convex optimization with Tikhonov regularization. *Journal of Mathematical Analysis and Applications*, 457(2):1065–1094, 2018.

[3] R. Boţ, G. Dong, P. Elbau, and O. Scherzer. Convergence rates of first and higher order dynamics for solving linear ill-posed problems. Preprint on ArXiv 1812.09343, University of Vienna, Austria, 2018.

[4] R. I. Boţ and E. R. Csetnek. Second order forward-backward dynamical systems for monotone inclusion problems. *SIAM Journal on Control and Optimization*, 54(3):1423–1443, 2016.

[5] Yu. E. Nesterov. A method for solving the convex programming problem with convergence rate $O(1/k^2)$. *Doklady Akademii Nauk SSSR*, 269(3):543–547, 1983.

[6] D. Showalter. Representation and computation of the pseudoinverse. *Proceedings of the American Mathematical Society*, 18:584–586, 1967.

[7] W. Su, S. Boyd, and E. Candès. A differential equation for modeling nesterov's accelerated gradient method: Theory and insights. *Journal of Machine Learning Research (JMLR)*, 17(153):1–43, 2016.


## An efficient reconstruction approach for a class of dynamic imaging operators


Melina-Loren Kienle Garrido

(joint work with Bernadette N. Hahn)


We are dealing with the problem of recovering a searched-for quantity $f$ from tomographic data, which are corrupted by motion of the object. This plays an important role in applications, for example in medical imaging or non-destructive testing. As models for the dynamic imaging problem we consider generalized Radon transforms

$$\mathcal{A}_\Gamma f(\varphi, s) = \int e^{i\sigma(s-\Psi_\Gamma(\varphi,x))} a_\Gamma(\varphi, s, x) f(x)\,\mathrm{d}x\,\mathrm{d}\sigma,$$

with $(\varphi, s) \in \Theta \times \Pi$, since they cover a broad range of applications, such as computerized tomography or photoacoustic tomography data. Here, both $\Psi_\Gamma$, characterizing the manifold we are integrating over, and the amplitude $a_\Gamma$ depend on a smoothly diffeomorphic motion $\Gamma$, which models the dynamic behaviour of the object.

Apart from very special cases, e.g. affine deformations in computerized tomography (see [3]), there is no exact inversion formula known. Nevertheless, methods from microlocal analysis (see e.g. [5–8]) can provide insights on a suitable choice for reconstruction operators.

We aim at generalizing approaches from [4] for dynamic computerized tomography and from [1] for dynamic photoacoustic tomography with a very special deformation (namely a vertical stretching).

Therefore, we consider operators of the form

$$\mathcal{L}_\Gamma := \mathcal{B}_\Gamma \mathcal{P} \mathcal{A}_\Gamma,$$

with backprojection operator $\mathcal{B}_\Gamma$, corresponding to the formal dual of $\mathcal{A}_\Gamma$ and a pseudodifferential operator $\mathcal{P}$.

Now, using methods from microlocal analysis it can be shown that the singularities of $\mathcal{L}_\Gamma$ correspond to the singularities of $f$.
Further, we show that a regularized version of the operator $(\mathcal{L}_{\Gamma_n})^\gamma$ approximates the corresponding static operator $(\mathcal{L}_I)^\gamma$ as the motion $\Gamma_n$ converges to the identity $I$. Thus, in cases where we have an exact static inversion fromula (like for example in photoacoustic tomography, see [2]), the operator $\mathcal{P}$ can be chosen such that our dynamic reconstruction approach provides a good approximation to the searched-for quantity $f$, at least for small deformations.
From the presented approach, we derive a filtered backprojection type algorithm, which is tested on numerical examples from dynamic photoacoustic tomography, showing a significant reduction of motion artifacts.

## References


[1] J. Chung and L. Nguyen, *Motion estimation and correction in photoacoustic tomographic reconstruction* SIAM Journal on Imaging Sciences **10** (2017), 216–242.

[2] D. Finch, M. Haltmeier and Rakesh, *Inversion of spherical means and the wave equation in even dimensions* SIAM Journal on Applied Mathematics **68** (2007), 392–412.

[3] B. N. Hahn, *Reconstruction of dynamic objects with affine deformations in computerized tomography* Journal of Inverse and Ill-posed Problems **22** (2014), 323–339.

[4] B. N. Hahn and E. T. Quinto, *Detectable singularities from dynamic Radon data*, SIAM Jornal on Imaging Sciences **9** (2016), 1195–1225.

[5] L. Hörmander, *Fourier Integral Operators, I* Acta Mathematica **127** (1971), 79–183.

[6] V. P. Krishnan and E. T. Quinto, *Microlocal Analysis in Tomography* (Handbook of Mathematical Methods in Imaging) ed O. Scherzer (2015), New York: Springer-Verlag.

[7] F. Trèves, *Introduction to Pseudodifferential and Fourier Integral Operators* vol 1 *Pseudodifferential Operators* (The University Series in Mathematics) ed J. H. Kohn (1980) New York and London: Plenum Press.

[8] F. Trèves *Introduction to Pseudodifferential and Fourier Integral Operators* vol 2 *Fourier Integral Operators* (The University Series in Mathematics) ed J. H. Kohn (1980) New York and London: Plenum Press.


## Semi-discrete iteration methods in X-ray tomography

Jonas Vogelgesang

In practice, many applications of X-ray computed tomography suffer from incomplete data. For example in non-destructive testing applications when inspecting large objects or objects with extremely different diameters in longitudinal and transversal directions, the physical limitations of the scanning device do not allow a full rotation of the inspected object. Although more specific scanning geometries like laminographic geometries allow a full rotation of such objects, the measured data is only available for a restricted number of X-ray source positions.

In many cases it is reasonable to apply a semi-discrete data model to describe the measurement process as multiple separate measurements at fixed X-ray source positions. Thus, a system of linear operator equations is obtained,

$$\mathcal{X}_a f(\eta) = g_a(\eta),$$

where $\mathcal{X}_a$ describes the model operator of the scanning geometry at the X-ray source positions $a \in \mathbb{R}^n$. In the following, a semi-discrete model for the emerging system of linear operator equations is proposed together with a framework to solve linear systems of semi-discrete operator equations iteratively in a Hilbert space setting.

## 1. Semi-discrete operator model

Let $A_i$ be a bounded linear operator between real Hilbert spaces $X$ and $Y_i$ for $i \in I$ and $I \subset \mathbb{N}$ being a finite dimensional index set. Further, let

$$\mathcal{B} \coloneqq \{b_j\}_{j\in J} \subset X$$

be a set of mutually linearly independent elements for $J \subset \mathbb{N}$ with $|J| < \infty$. Considering $X_\mathcal{B} \coloneqq \operatorname{span} \mathcal{B}$, all elements $f \in X_\mathcal{B}$ can be represented as a linear combination

$$f = \sum_{j\in J} \mathbf{f}_j b_j \tag{1}$$

where the *basis coefficients* $\mathbf{f}_j \in \mathbb{R}$ are uniquely determined. Thus, a bijective mapping from $\mathbb{R}^{|J|}$ to $X$ is induced via the basis representation (1). This justifies the definition of the semi-discrete model operators

$$\mathbf{A}_i : \left(\mathbb{R}^{|J|}, \langle\cdot,\cdot\rangle_{W_i}\right) \to Y_i, \qquad \mathbf{A}_i\mathbf{f} \coloneqq \sum_{j\in J} \mathbf{f}_j\, A_i b_j \tag{2}$$

on the coefficient space with weighted inner products $\langle\cdot,\cdot\rangle_{W_i} \coloneqq \langle\cdot, W_i\,\cdot\rangle$ for some symmetric positive definite weight matrices $W_i$.

## 2. Semi-discrete iteration methods

Due to the uniqueness of (1) and the bijectivity of the induced mapping, solving $A_i f = g_i$, $i \in I$, in $X_\mathcal{B}$ is equivalent to solving the semi-discrete system

$$\mathbf{A}_i\mathbf{f} = g_i \qquad i \in I$$

for given right-hand sides $g_i \in Y_i$. To compute a solution of the semi-discrete problem, the iteration scheme

$$\begin{aligned} \mathbf{f}^{m,1} &= \mathbf{f}^m \\ \mathbf{f}^{m,i+1} &= \mathbf{f}^{m,i} + \Psi_i\left(g_i - \mathbf{A}_i\mathbf{f}^{m,i}\right) \qquad i \in I \\ \mathbf{f}^{m+1} &= \mathbf{f}^{m,|I|+1} \end{aligned} \tag{3}$$

is applied for an arbitrary initial basis vector $\mathbf{f}^0 \in \mathbb{R}^{|J|}$. The operators $\Psi_i : Y_i \to \left(\mathbb{R}^{|J|}, \langle\cdot,\cdot\rangle_{W_i}\right)$ are assumed to be bounded linear mappings from the data spaces to the weighted coefficient spaces. Since the coefficient spaces are finite dimensional, a

possible choice is $\Psi_i \coloneqq \lambda_i \mathbf{A}_i^\dagger$ yielding the relaxed *semi-discrete Kaczmarz* iteration. Choosing

$$\Psi_i \coloneqq \lambda_i \mathbf{A}_i^* \qquad \lambda_i > 0$$

where the adjoint semi-discrete operators $\mathbf{A}_i^*$ are given by

$$\mathbf{A}_i^* \varphi = W_i^{-1} \left( \langle A_i b_j, \varphi \rangle_{Y_i} \right)_{j \in J} \qquad \forall \varphi \in Y_i$$

gives rise to the *semi-discrete Landweber-Kaczmarz* iteration.

## 3. Application to X-ray tomography

Let $\Omega \subset \mathbb{R}^n$ denote the $n$-dimensional unit ball. For a rapidly decreasing function $f \in \mathcal{S}(\mathbb{R}^n)$ with compact support in $\Omega$ *the flat detector cone beam transform* is defined as

$$\mathcal{X}_a f(\eta) = \int_0^\infty f\left(a + t\left(\eta - a\right)\right) \, dt$$

where $a \in \mathbb{R}^n \setminus \bar{\Omega}$ denotes a fixed X-ray source position. Considering the restricted detector

$$\tilde{E}_a \coloneqq \{\eta \in \mathbb{R}^n : \langle \eta - \mathrm{d}_a, \mathrm{n}_a \rangle = 0\} \cap \mathcal{X}_a(\Omega)$$

with $\mathrm{n}_a \in \mathbb{R}^n$ denoting the normal vector and $\mathrm{d}_a \in \mathbb{R}^n$ the displacement vector, the cone beam transform

$$\mathcal{X}_a : L_2(\Omega, \omega_a) \to L_2(\tilde{E}_a, w_a)$$

is a bounded linear operator on weighted $L_2$-spaces with the weight functions

$$\omega_a(x) \coloneqq \|\tilde{a}\|^{-1} \left( \frac{\langle a - x, \tilde{a} \rangle}{\langle \tilde{a}, \tilde{a} \rangle} \right)^{(1-n)} \qquad \text{and} \qquad w_a(\eta) \coloneqq \left( \mathcal{X}_a \chi_\Omega(\eta) \right)^{-1}$$

and $\tilde{a} \coloneqq \mathrm{P}|_{\left(\tilde{E}_a - \mathrm{d}_a\right)^\perp} (a - \mathrm{d}_a)$. Thus, the proposed semi-discrete approach can be applied to solve the system

$$\mathcal{X}_{a_i} f(\eta) = g_{a_i}(\eta)$$

where $\{a_i\}_{i \in I} \subset \mathbb{R}^n \setminus \bar{\Omega}$ is a finite set of fixed X-ray sources and $g_{a_i} \in L_2(\tilde{E}_{a_i}, w_{a_i})$ denotes the measured data for $i \in I$.

Analogously to (2), the semi-discrete model operators are defined as

$$\mathbf{X}_i : \left( \mathbb{R}^{|J|}, \langle \cdot, \cdot \rangle_{W_i} \right) \to L_2(\tilde{E}_{a_i}, w_{a_i}), \qquad \mathbf{X}_i \mathbf{f}(\eta) \coloneqq \sum_{j \in J} \mathbf{f}_j \mathcal{X}_{a_i} b_j(\eta),$$

giving rise to the semi-discrete problem

$$\mathbf{X}_i \mathbf{f}(\eta) = g_{a_i}(\eta) \qquad i \in I.$$

To solve this problem, the semi-discrete Landweber-Kaczmarz iteration is applied. Thus, with $\Psi_i \coloneqq \lambda_i \mathbf{X}_i^*$ and the diagonal weight matrices

$$(W_i)_{jj} \coloneqq \left\langle \mathcal{X}_{a_i} b_j, \sum_{l \in J} \mathcal{X}_{a_i} b_l \right\rangle_{L_2(\tilde{E}_{a_i}, w_{a_i})}$$

the semi-discrete iteration scheme

$$\begin{aligned}\mathbf{f}^{m,1} &= \mathbf{f}^m \\ \mathbf{f}^{m,i+1} &= \mathbf{f}^{m,i} + \lambda_i \left( \frac{\left\langle \mathcal{X}_{a_i} b_j, g_{a_i} - \mathbf{X}_i \mathbf{f}^{m,i} \right\rangle_{L_2(\tilde{E}_{a_i}, w_{a_i})}}{\left\langle \mathcal{X}_{a_i} b_j, \sum_{l \in J} \mathcal{X}_{a_i} b_l \right\rangle_{L_2(\tilde{E}_{a_i}, w_{a_i})}} \right)_{j \in J} \qquad i \in I \\ \mathbf{f}^{m+1} &= \mathbf{f}^{m,|I|+1}\end{aligned}$$

is obtained from (3) for some arbitrary initial value $\mathbf{f}^0 \in \mathbb{R}^{|J|}$. With the parameter choice

$$\lambda_i \in \left( 1 - \frac{1}{\sqrt{\kappa(W_i)}}, 1 + \frac{1}{\sqrt{\kappa(W_i)}} \right) \qquad \forall i \in I$$

the scheme converges for $m \to \infty$. If the semi-discrete system is consistent, it holds

$$\mathbf{f}^m \to \mathrm{P}_{\ker(\mathbf{A})} \mathbf{f}^0 + \mathbf{f}^\dagger.$$

For applications and numerical results of the semi-discrete Landweber-Kaczmarz method we refer to [1] and [2]. Also, the incorporation of additional information into the reconstruction process such as geometrical a priori information in limited data tomography as well as material *and* geometrical prior information in the context of region-of-interest tomography from limited data is discussed in the given references.

## References

[1] J. Vogelgesang and C. Schorr, *A Semi-Discrete Landweber-Kaczmarz Method for Cone Beam Tomography and Laminography Exploiting Geometric Prior Information*, Sens Imaging 17:17 (2016).

[2] J. Vogelgesang and C. Schorr, *Iterative Region-of-Interest Reconstruction from Limited Data Using Prior Information*, Sens Imaging 18:16 (2017).

## Seismic tomography with the elliptic Radon transform in 3D

Christine Grathwohl

(joint work with Peer Christian Kunstmann, Eric Todd Quinto and Andreas Rieder)

A well-established method to investigate subsurface material parameters is to generate pressure waves on the surface and measure their reflections returning there at different points. If we assume that no shear waves appear and the medium has constant mass density, the propagation of these waves with speed of sound $\nu$ is described by the acoustic wave equation

$$\frac{1}{\nu^2(\mathbf{x})} \partial_t^2 u(t; \mathbf{x}, \mathbf{x}_\mathrm{s}) - \Delta u(t; \mathbf{x}, \mathbf{x}_\mathrm{s}) = \delta(\mathbf{x} - \mathbf{x}_\mathrm{s}) \delta(t) \tag{1}$$

at location $\mathbf{x} \in \mathbb{R}^3_+$ and for time $t \geq 0$ where $\mathbf{x}_\mathrm{s}$ is the source point. The task is to reconstruct $\nu$ from the backscattered field $u(t; \mathbf{x}_\mathrm{r}, \mathbf{x}_\mathrm{s})$ observed at a receiver point

$\mathbf{x}_\mathrm{r}$ for $(t;\mathbf{x}_\mathrm{s},\mathbf{x}_\mathrm{r}) \in [0,T_{\max}] \times \mathcal{S} \times \mathcal{R}$ where $\mathcal{S}$ and $\mathcal{R}$ are the sets of source and receiver positions, respectively, and $T_{\max}$ is the recording time.

We consider a scanning geometry with constant distance from source to receiver. Thus, let $\mathbf{x}_\mathrm{s} = \mathbf{x}_\mathrm{s}(s) = (s_1, s_2 - \alpha, 0)$ and $\mathbf{x}_\mathrm{r} = \mathbf{x}_\mathrm{r}(s) = (s_1, s_2 + \alpha, 0)$ for $\alpha > 0$ fixed and $(s_1, s_2) \in S_0$ with $S_0 \subset \mathbb{R}^2$ open, bounded and connected. Further, we make the ansatz

$$\frac{1}{\nu^2(\mathbf{x})} = \frac{1 + n(\mathbf{x})}{c^2}.$$

with a smooth and a priori knwon background velocity $c$ which we assume to be constant. The corresponding solution $\widetilde{u}$ satisfies (1) with speed of sound $c$ instead of $\nu$. For simplicity, we choose $c = 1$. After we made this ansatz, we search for $n$ instead of $\nu$.

Under the assumption that no multiple scattering occurs we linearize the problem by the Born approximation. This yields a linear integral equation for $n$. Here, we follow the lines of [1] and [7].

Our linearized version then reads

$$Fn(s,T) = 32\pi^2 \int_0^T (T-t)(u - \widetilde{u})(t; \mathbf{x}_\mathrm{r}(s), \mathbf{x}_\mathrm{s}(s))\,\mathrm{d}t$$

where

$$Fn(s,T) = -2 \int_{E(s,T)} \frac{n(\mathbf{x})}{|\mathbf{x}_\mathrm{s}(s) - \mathbf{x}||\mathbf{x} - \mathbf{x}_\mathrm{r}(s)|}\,\mathrm{d}\sigma(\mathbf{x})$$

is a generalized Radon transform with the half-ellipsoid

$$E(s,T) = \{\mathbf{x} \in \mathbb{R}^3_+ \mid |\mathbf{x}_\mathrm{s}(s) - \mathbf{x}| + |\mathbf{x} - \mathbf{x}_\mathrm{r}(s)| = T\}$$

for $s = (s_1, s_2) \in S_0$ and $T \in [0, T_{\max}]$.

As we are not interested in exact values of $n$ but in its singularities, we consider the reconstruction operator

$$\Lambda := -\partial_3 \Delta F^* \psi F$$

where $\partial_3$ is the derivative in third space direction, $\Delta$ the Laplacian and $\psi$ a smooth cut-off function, necessary to compose $F^*$ and $F$. Hence, we reconstruct $\Lambda n$ via

$$\Lambda n = -\partial_3 \Delta F^* \psi g$$

from our measurements $g = Fn$.

The generalised Radon transform $F$ satisfies the Bolker assumption (see [2]). Multiplying $F$ with the cut-off $\psi$ the composition of $F^*$ with $\psi F$ is well-defined and so, we achieve that $F^*\psi F$ is a pseudodifferential operator of order $-2$ (see [5]). With the two differential operators in front of $F^*$ the reconstruction operator $\Lambda$ is a pseudodifferential operator of order 1. Due to its positive order $\Lambda$ emphasizes the singularities of $n$.

**Theorem 1.** *The principal symbol of* $\Lambda = -\partial_3 \Delta F^* \psi F$ *as a pseudodifferential operator is*

$$\sigma(\mathbf{x}, \xi) = \frac{4\pi^2 \xi_3 |\xi|^2}{|\mathbf{x}_\mathrm{s} - \mathbf{x}|^2 |\mathbf{x} - \mathbf{x}_\mathrm{r}|^2} \frac{\psi(s, \varphi(s, \mathbf{x}))}{|\omega|^2 B(s, \mathbf{x})}$$

*where* $B$ *is defined by* $B(s, \mathbf{x}) = |\det(\nabla\varphi(s, \mathbf{x}), \partial_{s_1} \nabla\varphi(s, \mathbf{x}), \partial_{s_2} \nabla\varphi(s, \mathbf{x}))|$ *with* $\varphi(s, \mathbf{x}) = |\mathbf{x}_\mathrm{s} - \mathbf{x}| + |\mathbf{x} - \mathbf{x}_\mathrm{r}|$ *and* $s$ *and* $\omega$ *are implicitly given by* $\xi = \omega \nabla\varphi(s, \mathbf{x})$ .

For the explicit expressions of $s$ and $\omega$ as functions of $\mathbf{x}$ and $\xi$ we refer to Lemma 3.6 in [4]. To find out which singularities are preserved we need to know where $\Lambda$ is microllocally elliptic.

**Proposition 2.** *If* $\xi_0 \in C(\mathbf{x}_0) = \{\xi \in \mathbb{R}^3 \,|\, \xi_3 \neq 0, \psi(\mathbf{x}_0, \xi) > 0\}$ *the operator* $\Lambda$ *is microlocally elliptic of order* 1 *at* $(\mathbf{x}_0, \xi_0)$.

The subsequent corollary follows by Proposition 2 and a general result (e.g. [6]). Here, $\mathrm{WF}^r(u)$ denotes the $H^r$-wave front set of a distribution $u$.

**Corollary 3.** *Let* $u \in \mathcal{E}'(\mathbb{R}^3_+)$ *and* $\mathbf{x} \in \mathbb{R}^3_+$. *If* $\xi \in C(\mathbf{x})$ *then*

$$(\mathbf{x}, \xi) \in \mathrm{WF}^r(u) \Leftrightarrow (\mathbf{x}, \xi) \in \mathrm{WF}^{r-1}(\Lambda u).$$

Roughly speaking, a distribution $u$ is not $H^r$ at $\mathbf{x}$ in direction $\xi$ if and only if $\Lambda u$ is not $H^{r-1}$ at $\mathbf{x}$ in direction $\xi$.

As the principal symbol $\sigma$ of $\Lambda$ is not independent of the offset $\alpha$ and the depth $x_3$ we aim to modify $\Lambda$. For this purpose, we consider the case $\alpha = 0$, so $\mathbf{x}_\mathrm{s} = \mathbf{x}_\mathrm{r}$, which we get approximately for large $x_3$ in comparison to $\alpha$. In this case, the principal symbol of $\Lambda$ behaves like $x_3^{-2}$. By inserting the operator which multiplicates with $x_3^2$ we get an operator with principal symbol $x_3^2 \sigma(\mathbf{x}, \xi)$ which depends on $x_3$ only via the cut-off $\psi$.

Moreover, the principal symbol $\sigma = \sigma(\mathbf{x}, \xi)$ of $\Lambda$ behaves like $\alpha^{-2}$ for $\alpha \to \infty$ if $\xi_2 \neq 0$ is satisfied. Thus, we insert the factor $\alpha^2$ and add this operator to the modified one before.

With these modifications we obtain the modified reconstruction operator

$$\Lambda_\mathrm{mod} = -\partial_3 \Delta (\mathbf{x_3^2} + \alpha^2 I) F^* \psi F$$

where $\mathbf{x_3^2}$ denotes the multiplication operator induced by $x_3^2$. Proposition 2 and Corollary 3 remain true for $\Lambda_\mathrm{mod}$. For small $\alpha$ in comparison to $x_3$ the first operator of $\Lambda_\mathrm{mod}$ dominates, for large $\alpha$ the second one. Thus, we achieve reconstructions nearly independent of the offset $\alpha$ and the depth $x_3$.

Due to the structure of the reconstruction operators $\Lambda$ and $\Lambda_\mathrm{mod}$ it is natural to apply the method of the approximative inverse for numerical reconstructions. We refer to the two-dimensional case in [3] for details. The images show two

reconstructions where $n = \chi_{B_2(0,0,4)} - \chi_{B_1(0,0,4)} + \chi_{B_{1.5}(3,0,5)}$ is a sum of characteristic functions. On the left image we have offset $\alpha = 1$, on the right $\alpha = 10$.

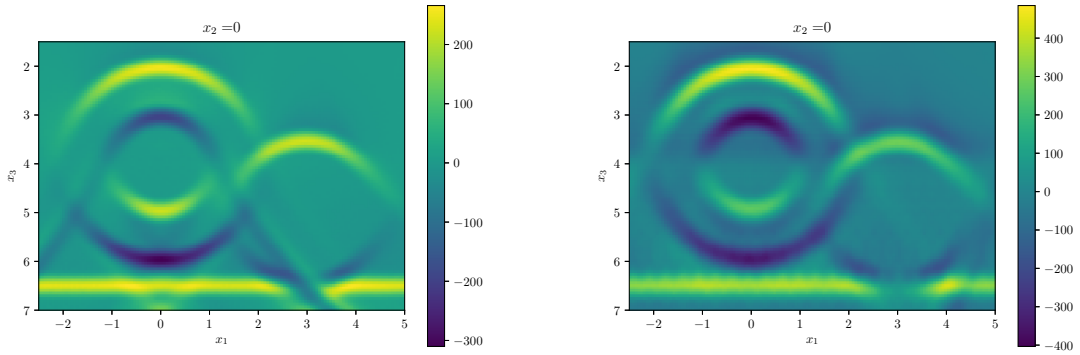


**Acknowledgement.** We gratefully acknowledge financial support by the Deutsche Forschungsgemeinschaft (DFG) through CRC 1173. E. T. Quinto thanks the U.S. National Science Foundation for their support under the grant DMS 1712207.

## References

[1] J. K. Cohen and N. Bleistein, *Velocity inversion procedure for acoustic waves*, Geophysics **44** (1979), 1077–1085.

[2] R. Felea,V. P. Krishnan, C. J. Nolan, E. T. Quinto, *Common midpoint versus common offset acquisition geometry in seismic imaging*, Inverse Problems & Imaging **10** (2016), 87–102.

[3] C. Grathwohl, P. C. Kunstmann, E. T. Quinto, A. Rieder, *Approximate inverse for the common offset acquisition geometry in 2D seismic imaging*, Inverse Problems **34** (2018), 014002.

[4] C. Grathwohl, P. C. Kunstmann, E. T. Quinto, A. Rieder, *Microlocal analysis of imaging operators for effective common offset seismic reconstruction*, Inverse Problems **34** (2018), 114001.

[5] V. Guillemin, S. Sternberg, *Geometric asymptotics*, Mathematical Surveys **14** (1977), American Mathematical Society.

[6] B. E. Petersen, *Introduction to the Fourier transform and pseudo-differential operators*, Monographs and Studies in Mathematics **19** (1983), Pitman, Boston.

[7] W. W. Symes, *Mathematics of reflection seismology*, Technical report, The Rice Inversion Project, Rice University, Houston, TX, USA (1998).

## Inverse problems in Adaptive Optics: wavefront reconstruction methods for the pyramid and the new ιQuad sensor

Victoria Hutterer

(joint work with Ronny Ramlau, Iuliia Shatokhina, Olivier Fauvarque and Andreas Obereder)

Atmospheric turbulence and diffraction of light induce blurred images of celestial bodies when they are observed by ground based telescopes. To compensate the perturbations, the new generation of telescopes involves the technology of Adaptive Optics (AO). An AO system consists of wavefront sensors, a control algorithm and deformable mirrors. Wavefront sensors provide quantitative information about

incoming distorted wavefronts, deformable mirrors physically correct for the atmospheric aberrations and the control algorithm gives a relation between wavefront sensor measurements and optimal mirror actuator commands. To derive actuator commands the knowledge of the shape of the wavefronts is essential. Reconstruction of the unknown wavefronts from given sensor measurements is an inverse problem. In the era of Extremely Large Telescopes (ELTs) with primary mirror diameters up to 40 m the computational load of existing control algorithms is immense which makes the development of new and fast methods important.

Pyramid wavefront sensors [1, 2] are included as baseline on many instruments under development for ELTs due to their increased sensitivity compared to other sensors. Hence, appropriate wavefront reconstruction algorithms are currently in high demand. Using Fourier optics the model of the pyramid sensor is described by a non-linear combination of one and two dimensional Hilbert transforms of the sine and cosine of the incoming wavefront. Based on detailed analytical studies [3] of the pyramid sensor we developed several linear and non-linear wavefront reconstruction methods [4–6] which are utilizing approximations of the mathematical forward model. Although we obtain precise reconstructions applying those simplifications, the goal is to rely on more exact underlying models in order to further improve the accuracy. Additionally, we consider real life features such as so-called telescope spiders. These structures create areas where the information on the wavefront is isolated and thus segmented on the wavefront sensor detector introducing additional errors in the reconstructions [7].

Based on optical Fourier filtering (similar to pyramid wavefront sensors) a new sensor device, the so-called $\imath$Quad sensor [8] was recently invented. We provide an optical description, underlying mathematical models and first reconstruction approaches for the new wavefront sensor.

## References

[1] R. Ragazzoni. *Pupil plane wavefront sensing with an oscillating prism*, J. of Modern Optics **43**(2), (1996), 289–293.

[2] C. Vérinaud. *On the nature of the measurements provided by a pyramid wave-front sensor*, Optics Communication **233**, (2004).

[3] V. Hutterer, R. Ramlau, Iu. Shatokhina. *Real-time Adaptive Optics with pyramid wavefront sensors: A theoretical analysis of the pyramid sensor model*, accepted in Inverse Problems.

[4] V. Hutterer, R. Ramlau. *Wavefront Reconstruction from Non-modulated Pyramid Wavefront Sensor Data using a Singular Value Type Expansion*, Inverse Problems **34**, (2018), 035002.

[5] V. Hutterer, R. Ramlau, Iu. Shatokhina. *Real-time Adaptive Optics with pyramid wavefront sensors: Accurate wavefront reconstruction using iterative methods*, accepted in Inverse Problems.

[6] V. Hutterer, R. Ramlau. *Non-linear wavefront reconstruction methods for pyramid sensors using Landweber and Landweber-Kaczmarz iteration.* Applied Optics **57**(30), (2018), 8790–8804.

[7] V. Hutterer, Iu. Shatokhina, A. Obereder, R. Ramlau. *Advanced reconstruction methods for segmented ELT pupils using pyramid sensors*. J. Astron. Telesc. Instrum. Syst. **4**(4), (2018). 049005.
[8] O. Fauvarque, V. Hutterer et al., *The ıQuad sensor: a new Fourier-based WFS derived from the 4Q-coronagraph*, in preparation.

## Regularization of Inverse Problems with Deep Learning and Neural Networks

Markus Haltmeier
(joint work with Stephan Antholzer and Johannes Schwab)

Many challenges in natural sciences and elsewhere yield to the solution of inverse problems for which the solution is either under-determined, sensitive with respect to data perturbation, or both. Classical solution approaches are based on regularization methods which are basically stable approximations to the Moore Penrose inverse. Recently, deep learning based methods appeared as a new paradigm for solving inverse problems, often with outstanding performance. We recall classical concepts and present some recent developments on deep learning methods for inverse problems. We introduce and analyze two different deep-learning based regularization approaches: regularizing two-step networks [1] and the NETT [2].

### 1. Inverse problems

In this paper, we consider the standard setting of inverse problems, where the task is to estimate the unknown $\boldsymbol{x} \in \mathbb{X}$ from data

$$\boldsymbol{y} = \mathcal{A}\boldsymbol{x} + \boldsymbol{\xi}\,. \tag{1}$$

Here $\mathcal{A}\colon \mathbb{X} \to \mathbb{Y}$ is a bounded linear operator between Hilbert spaces, and $\boldsymbol{\xi}$ denotes the data distortion that satisfies $\|\boldsymbol{\xi}\| \leq \delta$ for some noise level $\delta \geq 0$. A characteristic property of inverse problems is the ill-posedness. This means that the solution of (1) is either not unique or unstable with respect to data perturbations. To solve such kind of inverse problems one has to employ regularization methods, which serve the following two main purposes: First, they account for the non-uniqueness by selecting particular solutions of the noise-free equation $\boldsymbol{y} = \mathcal{A}\boldsymbol{x}$. Second, they approximate (1) by neighboring but stabler problems. A prominent method is to minimize the Tikhonov functional $\mathcal{T}_{\boldsymbol{y},\alpha}(\boldsymbol{x}) = \frac{1}{2}\|\mathcal{A}\boldsymbol{x} - \boldsymbol{y}\|^2 + \frac{\alpha}{2}\|\boldsymbol{x}\|^2$. As other classical approaches, Tikhonov regularization is designed to approximate solutions with minimal Hilbert space norm.

As has been realized some time ago, solutions with small Hilbert space norm are often not the desired ones in practical applications. Variational regularization replaces the Hilbert space norm penalty by a general convex regularizer $r\colon \mathbb{X} \to [0,\infty]$ and considers minimizers of the generalized Tikhonov regularization $\mathcal{T}_{\boldsymbol{y},\alpha}(\boldsymbol{x}) = \frac{1}{2}\|\mathcal{A}\boldsymbol{x} - \boldsymbol{y}\|^2 + \alpha r(\boldsymbol{x})$, where the prior knowledge is encoded in $r(\boldsymbol{x})$. While often being a significant improvement over the Hilbert space norm,

such hand-crafted priors do also not optimally represent realistic signal classes. Moreover, the implementation requires time consuming iterative minimization.

## 2. Regularization by deep learning

In the very recent years, deep learning based methods appeared as a new powerful tool for solving inverse problems. Instead of using a hand crafted prior, they adapt to a certain class of unknowns, by using a training data set

$$\mathcal{D}_N := \{(\boldsymbol{x}_n, \boldsymbol{y}_n) \mid n = 1, \dots, N\}\,. \tag{2}$$

Here $\boldsymbol{x}_n \in \mathbb{M}$ are elements taken from a set $\mathbb{M}$ of desired outputs, and $\boldsymbol{y}_n$ are the corresponding data. Based on the training data, one selects the reconstruction operator $\mathcal{B}\colon \mathbb{Y} \to \mathbb{X}$ from a parametrized family of possible candidates. Various such tools have been proposed in the literature. In this short note, we focus on regularizing two-step networks and the NETT which, to the best of our knowledge, are the only deep learning approaches that are known to be regularization methods. In the following we refer to any element of a parametrized family $(\mathcal{N}_\theta)_{\theta\in\mathbb{R}^p}$ of mappings $\mathcal{N}_\theta\colon \mathbb{X} \to \mathbb{X}$ as neural network (NN). Likewise, we call any element of a family $(\mathcal{R}_\theta)_{\theta\in\mathbb{R}^p}$ of mappings $\mathcal{R}_\theta\colon \mathbb{Y} \to \mathbb{X}$ a reconstruction network.

2.1. **Regularizing two-step networks.** The probably simplest deep learning approach uses a reconstruction network of the form $\mathcal{R} = \mathcal{N} \circ \mathcal{A}^\sharp\colon \mathbb{Y} \to \mathbb{X}$, where $\mathcal{A}^\sharp\colon \mathbb{Y} \to \mathbb{X}$ is an operator that performs an initial reconstruction and $\mathcal{N}$ is a standard NN (sometimes called post-processing). In particular, the so-called residual networks $\mathcal{N} = \mathrm{Id} + \mathcal{U}$ have been demonstrated to give accurate results. The network is adjusted to a particular application and training data set by minimizing a loss function such as $E_N(\mathcal{D}_N, \theta) := \frac{1}{N}\sum_{k=1}^N \|\mathcal{N}_\theta \circ \mathcal{A}^\sharp \boldsymbol{y}_n - \boldsymbol{x}_n\|^2$ over $\theta \in \mathbb{R}^p$. The minimization of $E_N$ is called the training phase. A benefit of the two-stage approach is that $\mathcal{A}^\sharp \boldsymbol{y}_n$ can be computed once before the training phase. Therefore, network training can be performed very efficiently using existing advanced software tools to evaluate $E_N$ and its gradient with respect to $\theta$.

Especially, when applied to elements $\boldsymbol{x} \in \mathbb{X}$ very different from the training data, standard residual networks may lack data consistency. This means that even when $\|\mathcal{A}^\sharp \boldsymbol{x} - \boldsymbol{y}\|$ is small, there is no control over $\|\mathcal{N}_\theta \mathcal{A}^\sharp \boldsymbol{x} - \boldsymbol{y}\|$. To overcome this issue, in [1] we consider the modified structure, that we named null space network,

$$\mathcal{N} = \mathrm{Id} + \mathcal{A}_{\ker(\mathcal{A})} \circ \mathcal{U}\colon \mathbb{X} \to \mathbb{X}\,. \tag{3}$$

Here $\mathcal{A}_{\ker(\mathcal{A})}$ denotes the projection onto the null space $\ker(\mathcal{A})$ of $\mathcal{A}$, and $\mathcal{U}$ is any NN. Considering $\mathcal{A}_{\ker(\mathcal{A})}\mathcal{U}$ instead of $\mathcal{U}$ implies that the null space network preserves data consistency. Moreover, in [1] we derived the following result.

**Theorem 1.** *Let the family $(\mathcal{B}_\alpha)_{\alpha>0}$ together with the parameter choice $\alpha^\star\colon (0,\infty) \times \mathbb{Y} \to (0,\infty)$ be a classical regularization method (approximating the Moore-Penrose inverse), and let $\mathcal{N}$ be a null-space network as in* (3)*. Then, $(\mathcal{R}_\alpha)_{\alpha>0}$ defined by*

$$\forall \alpha > 0\colon \quad \mathcal{R}_\alpha = \mathcal{N} \circ \mathcal{B}_\alpha\colon \mathbb{Y} \to \mathbb{X}\,, \tag{4}$$

*together with the parameter choice $\alpha^\star$, is a regularization method adapted to $\mathbb{M} := \mathcal{N}\big(\ker(\mathcal{A})^\perp\big)$ for (1). This means that for every $\boldsymbol{x} \in \mathbb{M}$ we have $\lim_{\delta\to 0} \sup\{\|\boldsymbol{x} - \mathcal{R}_{\alpha^\star(\delta,\boldsymbol{y})}\boldsymbol{y}\| : \boldsymbol{y} \in \mathbb{Y} \wedge \|\boldsymbol{y} - \mathcal{A}\boldsymbol{x}\| \le \delta\} = 0$.*

In [1] we also derived convergence rates for the null space regularizations. The role of the NN in (4) is to select a particular solution which is the main issue in undersampled tomographic problems. For inverse problems where the singular values are rapidly decaying but only a small part of them is strictly equal to zero it is important that the networks are allowed to also map to values outside of the kernel for $\delta > 0$. This issue has been addressed in [3], where we analyzed more general regularizing networks $\mathcal{R}_\alpha = \mathcal{N}_\alpha \circ \mathcal{B}_\alpha$ with $(\mathcal{N}_\alpha)_{\alpha>0}$ being a family of networks that converge to a null-space network as $\alpha \to 0$.

2.2. **NETT: Tikhonov regularization with a learned regularizer.** An alternative way to to obtain a deep learning based regularization method has been proposed and analyzed in [2], and considers Tikhonov regularization

$$\mathcal{T}_{\boldsymbol{y},\alpha}(\boldsymbol{x}) := \frac{1}{2}\|\mathcal{A}\boldsymbol{x} - \boldsymbol{y}\|^2 + \frac{\alpha}{2}\|\mathcal{N}(\boldsymbol{x})\|^2, \tag{5}$$

where $\mathcal{N} : \mathbb{X} \to \Xi$ is a trained NN defining the regularizer. Here $\Xi$ is a Hilbert space and $\alpha > 0$ a regularization parameter. The resulting reconstruction approach has been named NETT (for network Tikhonov regularization), as it is a generalized form of Tikhonov regularization using a NN as trained regularizer. In [2], the following is shown.

**Theorem 2.** *Consider the NETT functional (5) where $\mathcal{N} : \mathbb{X} \to \mathbb{X}$ has the form $\mathcal{N} = \sigma_L \circ \mathcal{W}_L \circ \sigma_{L-1} \circ \mathcal{W}_{L-1} \circ \cdots \circ \sigma_1 \circ \mathcal{W}_1$ with $L \ge$ and mappings $\sigma_\ell$, $\mathcal{W}_\ell$ being all coercive and weakly continuous. Then, minimizing $\mathcal{T}_{\boldsymbol{y},\alpha}$ is well posed, weakly stable and weakly convergent in the sense of [4, Theorems 3.22, 3.23 and 3.26].*

On the theoretical level, the main difference between the NETT (5) and standard variational regularization is the non-convexity of the NN based regularizer. As pointed out in [2], the proof Theorem 2 follows as in the convex case [4]. However, the strong convergence and the derivation of convergence rates requires extra work. For that purpose, in [2] we introduced and studied the novel concepts of absolute Bregman distance and total nonlinearity. A possible training strategy proposed in [2] uses training data (2) and trains $\mathcal{N}$ to map $\mathcal{A}^\sharp \boldsymbol{y}_n$ to the artifacts $\mathcal{A}^\sharp \boldsymbol{y}_n - \boldsymbol{x}_n$, and the artifact-free images $\boldsymbol{x}_n$ to the zero image $\mathbf{0} \in \mathbb{X}$. Regularized solutions therefore favor being similar to the elements of training class $\mathbb{M}$ rather than containing artifact structures.

## References

[1] J. Schwab, S. Antholzer, and M. Haltmeier, "Deep null space learning for inverse problems: convergence analysis and rates," *Inverse Probl.* **35**(2), p. 025008, 2019.

[2] H. Li, J. Schwab, S. Antholzer, and M. Haltmeier, "NETT: Solving inverse problems with deep neural networks," 2018. arXiv:1803.00092.

[3] J. Schwab, S. Antholzer, and H. M. Haltmeier, "Big in Japan: Regularizing networks for solving inverse problems," 2018. arXiv:1812.00965.
[4] O. Scherzer, M. Grasmair, H. Grossauer, M. Haltmeier, and F. Lenzen. *Variational methods in imaging*, volume 167 of *Applied Mathematical Sciences*. Springer, New York, 2009.

## Towards Learning of Efficient Algorithms for Image Reconstruction

Andreas Maier

This is a short report on the latest developments on computed tomography and inverse problems at the Pattern Recognition Lab, Friedrich-Alexander-University Erlangen-Nuremberg, Germany in 2018. In particular these developments include application of deep learning methods to image reconstruction and medical imaging in general.

### 1. Deep and Precision Learning

In recent years, the methods of *deep learning* have revolutionized large fields in pattern recognition from speech processing to computer vision [1]. Lately, these techniques became also popular in image reconstruction and for the efficient solution of inverse problems [2–4]. In contrast to several other groups, we propose to blend *black-box deep learning* with prior knowledge in order to restrict the solution space to physically and algorithmically plausible solutions. We coined this known operator approach *precision learning*. In [5], we demonstrated that this approach reduces maximal error bounds of the training problem and has several other guarantees that black-box deep learning is not able to give. In our framework, any operation that allows computation of a sub-gradient towards its input variables can be employed.

### 2. Deep Learning Computed Tomography

In [4,6], we demonstrate that the well-known Feldkamp-Davis-Kress (FDK) Algorithm can be mapped mathematically identically onto a three-layer neural network that consists of a multiplicative, a convolutional, and a fully connected layer. Doing so, one does not even require training, as the multiplication is initialized using Cosine and Parker weights, the convolutional layer uses the Ramp Filter, and the fully connected layer implements back-projection. In this constellation, we demonstrated that we are able to train the weights of the multiplicative layer to limited angle problems, even though the actual back-projection matrix does not fit into a computer's main memory. We use – similar to iterative reconstruction – efficient implementation of projection and back-projection on GPUs. This way the limited angle reconstruction is solved efficiently in a single forward-pass at run-time. Learned weights resemble heuristic configurations that were found by other researchers [7,8]. Remaining streaks can be efficiently further reduced using the variational networks approach by Hammernik et al. [9]. This way, we remain with an interpretable neural network that is analytically equivalent to FDK reconstruction followed by interative image-domain de-streaking.

## 3. Attacks on Deep Learning Reconstruction

Recently, so-called *adversarial attacks* have demonstrated to mislead neural networks towards false classifications [10]. So far, this concept was only applied to classification or segmentation tasks. In [11], we demonstrated that similar concepts also apply to reconstruction networks. In particular, we found that U-nets with their non-local receptive field can be misled in such a way that lesions disappear from CT slice images. Hence, general black-box deep learning reconstruction networks like the ones presented in [3] are to be handled with caution.

## 4. Deriving Neural Networks

Given the concept of *precision learning* and the mathematical equivalence of neural network and reconstruction algorithm, we can also approach other problems in medical imaging. In [12], we investigate whether it is possible to re-bin a parallel MRI acquisition to fan-beam geometry using a filtering-based approach. We demonstrate that we can reformulate the problem using an algebraic approach. Doing so, we solve for the unknown fan-beam projections and postulate that the inverse that is required during this computation is a circulant matrix. As a result, we derive an algorithm that is known up-to-the circulant operator that is conveniently initialized as the Ramp filter. Using 50 synthetic phantoms, we demonstrate that we are able to estimate an appropriate filter kernel that also generalizes to real data. As such we employ *deep learning* merely as a tool to efficiently minimize our optimization problem. Still, we hope that such use of the back-propagation algorithm will further facilitate the blend of math, physics, and computer science.

## References

[1] Maier, A., Syben, C., Lasser, T., Riess, C.: A gentle introduction to deep learning in medical image processing (2018)
[2] Ye, J.C., Han, Y., Cha, E.: Deep convolutional framelets: A general deep learning framework for inverse problems. SIAM Journal on Imaging Sciences **11**(2), 991–1048 (2018)
[3] Zhu, B., Liu, J.Z., Cauley, S.F., Rosen, B.R., Rosen, M.S.: Image reconstruction by domain-transform manifold learning. Nature **555**(7697), 487 (2018)
[4] Würfl, T., Hoffmann, M., Christlein, V., Breininger, K., Huang, Y., Unberath, M., Maier, A.K.: Deep learning computed tomography: Learning projection-domain weights from image domain in limited angle problems. IEEE transactions on medical imaging **37**(6), 1454–1463 (2018)
[5] Maier, A., Schebesch, F., Syben, C., Würfl, T., Steidl, S., Choi, J.H., Fahrig, R.: Precision Learning: Towards Use of Known Operators in Neural Networks. In: Tan, J.K.T. (ed.) 2018 24rd International Conference on Pattern Recognition (ICPR). pp. 183–188 (2018),
[6] Würfl, T., Ghesu, F.C., Christlein, V., Maier, A.: Deep Learning Computed Tomography. In: Springer (ed.) Medical Image Computing and Computer-Assisted Intervention – MICCAI 2016. vol. 3, pp. 432–440 (2016)
[7] Riess, C., Berger, M., Wu, H., Manhart, M., Fahrig, R., Maier, A.: Tv or not tv? that is the question. Proceedings Fully3D pp. 341–344 (2013)
[8] Schäfer, D., van de Haar, P., Grass, M.: Modified parker weights for super short scan cone beam ct. In: Proc. 14th Int. Meeting Fully Three-Dimensional Image Reconstruction Radiol. Nucl. Med. pp. 49–52 (2017)

[9] Hammernik, K., Würfl, T., Pock, T., Maier, A.: A deep learning architecture for limited-angle computed tomography reconstruction. In: Maier-Hein, geb. Fritzsche, K.H., Deserno, geb. Lehmann, T.M., Handels, H., Tolxdorff, T. (eds.) Bildverarbeitung für die Medizin 2017. pp. 92–97. Springer Berlin Heidelberg, Berlin, Heidelberg (2017)
[10] Yuan, X., He, P., Zhu, Q., Bhat, R.R., Li, X.: Adversarial examples: Attacks and defenses for deep learning. arXiv preprint arXiv:1712.07107 (2017)
[11] Huang, Y., Würfl, T., Breininger, K., Liu, L., Lauritsch, G., Maier, A.: Some investigations on robustness of deep learning in limited angle tomography. In: Frangi, A.F., Schnabel, J.A., Davatzikos, C., Alberola-López, C., Fichtinger, G. (eds.) Medical Image Computing and Computer Assisted Intervention – MICCAI 2018. pp. 145–153. Springer International Publishing, Cham (2018)
[12] Syben, C., Stimpel, B., Lommen, J., Würfl, T., Dörfler, A., Maier, A.: Deriving neural network architectures using precision learning: Parallel-to-fan beam conversion. In: German Conference on Pattern Recognition (GCPR) (2018)

## Task-based image reconstruction from tomographic data

Carola-Bibiane Schönlieb

(joint work with Jonas Adler, Martin Benning, Martin Burger, Veronica Corona, Hendrik Dirks, Lynn Gladden, Sebastian Lunz, Ozan Öktem, Andi Reci, Andy Sederman and Olivier Verdier)

Image reconstruction from indirect measurements, such as they appear in computed tomography (CT) or magnetic resonance imaging (MRI), is often complicated by incomplete and noisy measurements. Lots of work in the mathematical imaging community in the last thirty years or so has gone into the development, analysis and numerical realisation of image reconstruction methods from such data. In this work we are mainly interested in the subclass of variational regularisation and associated iterative reconstruction schemes.

While those are classically optimised for some measure of image quality, another strategy is to optimise the image reconstruction for a particular end-task at hand. Such a task-adapted reconstruction strategy is particularly appropriate in most biomedical applications where an image is not reconstructed to look 'pretty' but to be used for a subsequent quantification task, e.g. segmentation, classification, motion estimation etc.

Some examples in the literature for task-adapted reconstruction (also called feature reconstruction) from tomographic data are [6–11]. In our work we have investigated several instances of task-adapted reconstruction using variational models as well as recently introduced deeply learned iterative reconstruction approaches [1,2]. In [4] we propose a variational model for joint motion estimation and reconstruction and discuss its well-posedness and numerical solution. In [5] we consider a variational model for joint image reconstruction and segmentation from MRI data, and its numerical enhancement via Bregman iteration for which we provide a global convergence proof. In [3] we introduce a generic framework for task-adapted reconstruction based on deep neural networks, with examples for joint image reconstruction and segmentation, and joint image reconstruction and classification from tomographic data. In those works we show that in both cases, having

in mind the end-task already during the reconstruction step improves performance on the task. While a variational approach for task-adapted reconstruction gives the advantage of a strong theoretical foundation, its numerical solution and practical application are challenging due to its non-convexity and non-smoothness, and dependence on several free parameters. Task-adapted reconstruction with deep learning on the other hand, currently stands on shaky theoretical foundations, however, once trained, renders task-adapted reconstruction feasible also for very large-scale inverse problems.

### References


[1] J. Adler, O. Öktem, *Solving ill-posed inverse problems using iterative deep neural networks*, Inverse Problems, **33(12)** (2017), 124007.

[2] J. Adler, O. Öktem, *Learned primal-dual reconstruction*, IEEE transactions on medical imaging, **37(6)** (2018), 1322-1332.

[3] J. Adler, S. Lunz, O. Verdier, C. B. Schönlieb, O. Öktem, *Task adapted reconstruction for inverse problems*, arXiv preprint arXiv:1809.00948, (2018).

[4] M. Burger,H. Dirks, C.-B. Schönlieb, *A variational model for joint motion estimation and image reconstruction*, SIAM Journal on Imaging Sciences, **11(1)** (2018), 94-128.

[5] V. Corona, M. Benning, M. J. Ehrhardt, L. F. Gladden, R. Mair, A. Reci, A. J. Sederman, S. Reichelt, C.-B. Schönlieb, *Enhancing joint reconstruction and segmentation with non-convex Bregman iteration*, arXiv preprint arXiv:1807.01660 (2018).

[6] B. N. Hahn, *Efficient algorithms for linear dynamic inverse problems with known motion* Inverse Problems, **30(3)** (2014), 035008.

[7] A.K. Louis, P. Maass, *Contour reconstruction in 3-D X-ray CT*, IEEE transactions on medical imaging, **12(4)** (1993), 764-769.

[8] E. Klann, *A Mumford–Shah-like method for limited data tomography with an application to electron tomography*, SIAM Journal on Imaging Sciences, **4(4)** (2011), 1029-1048.

[9] R. Ramlau, W. Ring, *A Mumford–Shah level-set approach for the inversion and segmentation of X-ray tomography data*. Journal of Computational Physics, **221(2)** (2007), 539-557.

[10] J. P. Thirion, *Direct extraction of boundaries from computed tomography scans*, IEEE transactions on medical imaging, **13(2)** (1994), 322-328.

[11] E. I. Vainberg, I. A. Kazak, V. P. Kurozaev, *Reconstruction of the internal three-dimensional structure of objects based on real-time integral projections*, Soviet Journal of nondestructive testing - USSR, **17(6)** (1981), 415-423.


## Perspectives of Similarity Measures for Joint Multimodality Image Reconstruction


Ming Jiang

(joint work with Di He, Alfred K. Louis, Peter Maass and Thomas Page)


Joint multi-modality image reconstruction is to estimate images from measurement data simultaneously rather than separately and sequentially for each modality. A conceptual framework for joint multi-modality image reconstruction is as follows [1]. Without loss of generality, we consider bi-modal joint image reconstruction in the following. For $i = 1, 2$, let

$$A_i(f_i) = g_i, \tag{1}$$

be two forward operators of two imaging modalities, respectively. For each image reconstruction, we use the conventional regularization approach to formulate the following reconstruction functional,

$$E_i(f_i) = \|A_i(f_i) - g_i\|^2 + \alpha_i R_i(f_i) \tag{2}$$

where $R_i(f_i)$ is the regularization for $f_i$ and $\alpha_i > 0$ the regularization parameter, for $i = 1, 2$. Joint multi-modality image reconstruction is based on the observation that images of the same object from different modalities possess similar features, at least partially. Assume that $T$ is an feature operator of images, and that $D$ is a feature similarity of images. Then we can incorporate the feature similarity into the reconstruction process by updating the reconstruction functionals as following,

$$E_1(f_1) = \|A_1(f_1) - g_1\|^2 + \alpha_1 R_1(f_1) + \gamma_1 D\left[T(f_1), T(f_2)\right], \tag{3}$$

$$E_2(f_2) = \|A_2(f_2) - g_2\|^2 + \alpha_2 R_2(f_2) + \gamma_1 D\left[T(f_2), T(f_1)\right]. \tag{4}$$

In implementation, the images $f_1$ and $f_2$ are alternatively and iteratively reconstructed by minimizing (3) and (4), respectively. This conceptual framework is equivalent to alternatively minimizing the following joint reconstruction functional with respect to $f_1$ and $f_2$,

$$E(f_1, f_2) = \tau_1 E_1(f_1) + \tau_2 E_2(f_2), \tag{5}$$

with weights $\tau_1$ and $\tau_2$ on $E_1$ and $E_2$. Please note that the effect of the parameters $\tau_1$ and $\tau_2$ is incorporated into the parameters $\alpha_1$, $\gamma_1$, $\alpha_2$, $\gamma_2$ when performing the alternative minimization for $E_1$ and $E_2$ in (3) and (4) after re-parametrization, and hence can be ignored in implementation. This joint reconstruction functional can also be interpreted from a Bayesian formulation [1,2]. Recent work has demonstrated the performance of joint multi-modality reconstruction [3–6].

One new aspect of the joint multi-modality image reconstruction is the requirement for cross-modality image similarity measures of features to enable iterative methods to alternatively reconstruct images as aforementioned. The difficulty is because images of different modalities are of different ranges and different contrasts. There are features in one modality but not in another. Images of the same object from different modalities possess similar features, but mostly only partially in some regions. Similarity measures must encourage the reconstruction of features when there is sufficient evidence from data and avoid nonexistent features to be transferred into another [1]. This phenomenon that inappropriately reconstruction of nonexistent features due to inappropriate similarity measures can be called '*ill-transfer of features*', and should be addressed in designing similarity measures.

In his prominent paper [7], Tversky proposed his '*feature contrast model*' for the similarity of binary features. Features are binary in the sense that a given feature of an object either is or is not in its set of features $A$. An example of such binary feature is the edge set of an image. In a convincing and entertaining manner, Tversky argued why the requirements of symmetry and triangle inequality for similarity measures are unreasonable to explain a number of psychological experiments. Tversky proposed a set of axioms about similarity measures of binary features, which includes the axioms of matching, independence, solvability,

invariance, and proved mathematically that feature similarity measures must of the following form [7],

$$S(a,b) = p(A \cap B) - \gamma_1 p(A \setminus B) - \gamma_2 p(B \setminus A), \tag{6}$$

where $A$ and $B$ denote the sets of binary features associated with the objects $a$ and $b$, respectively, $\gamma_1$ and $\gamma_2$ are nonnegative constants. $p$ is an additive function such that $p(A \cap B) = p(A) + p(B)$ whenever $A \cap B = \emptyset$. Please note there the convention in [7] is that the more similar $a$ to $b$, the bigger the similarity $S(a,b)$ is. Similarity measures thus obtained increase with addition of common features and/or deletion of distinctive features (i.e., features that belong to one object but not to the other) [7], which coincides with the demand of similarity measures for avoiding *ill-transfer of features* in joint multi-modality image reconstruction .

For 2D images, a natural choice for $p$ with respect to image edge sets is the 1-dimensional Hausdorff measure $\mathcal{H}$, or the length of image edges. Therefore, we obtain,

$$S(f_1, f_2) = \mathcal{H}(K_1 \cap K_2) - \gamma_1 \mathcal{H}(K_1 \setminus K_2) - \gamma_2 \mathcal{H}(K_2 \setminus K_1), \tag{7}$$

where $K_1$ and $K_2$ are the image edge sets of images $f_1$ and $f_2$, respectively. Higher-dimensional Hausdorff measures can also be used in (7) for higher-dimensional images [8]. By using Mumford-Shah regularization function for each modality in (3) and (4), respectively,

$$R_i(f_i) = \int_{\Omega \setminus K_i} |\nabla f_i|^2 + \beta_i \mathcal{H}(K_i), \tag{8}$$

where $\Omega$ is the image domain, and using $D = -S$ as the feature similarity of images, by decomposing $K_1 = K_1 \cap K_2 \cup K_1 \setminus K_2$, and $K_2 = K_2 \cap K_1 \cup K_2 \setminus K_1$, we arrive at the following reconstruction functionals $E_1$ and $E_2$, after re-parametrization with the same symbols,

$$\begin{aligned} &E_1(u_1, K_1) \\ &= \|A_1(f_1) - g_1\|^2 + \alpha_1 \int_{\Omega \setminus K_1} |\nabla f_1|^2 + \beta_1 \left[\mathcal{H}(K_1 \cap K_2) + \gamma_1 \mathcal{H}(K_1 \setminus K_2)\right], \\ &E_2(u_2, K_2) \\ &= \|A_2(f_2) - g_2\|^2 + \alpha_2 \int_{\Omega \setminus K_2} |\nabla f_2|^2 + \beta_2 \left[\mathcal{H}(K_2 \cap K_1) + \gamma_2 \mathcal{H}(K_2 \setminus K_1)\right], \end{aligned} \tag{9}$$

where $\alpha_i$, $\beta_i$ and $\gamma_i$ $(i = 1, 2)$ are positive regularization parameters. It should be remarked that the above extended Mumford-Shah regularization has been proposed in [9]. This abstract provides another interpretation from the psychological perspective. Please note that images and edges are simultaneously reconstructed with the above extended Mumford-Shah regularization functionals. This new image similarity is evaluated with numerical phantoms for the joint reconstruction of XCT and DOT and demonstrate an image quality improvement by 15% in terms of SSIM compared to single model reconstruction [6].

It is expected the feature similarity used in this abstract can be applied for other applications where image similarity is required, such as slice-by-slice reconstruction of 3D volume images, dynamic imaging, multi-change and multi-spectral tomography, and video super-resolution generation.

## References

[1] Haber, E. and Gazit, M. H. (2013). Model fusion and joint inversion. *Surveys in Geophysics*, 34(5):675–695.
[2] Bowsher, J. E., Johnson, V. E., Turkington, T. G., Jaszczak, R. J., Floyd, C., and Coleman, R. E. (1996). Bayesian reconstruction and use of anatomical a priori information for emission tomography. *IEEE Transactions on Medical Imaging*, 15(5):673–686.
[3] Ehrhardt, M. J., Thielemans, K., Pizarro, L., Atkinson, D., Ourselin, S., Hutton, B. F., and Arridge, S. R. (2015). Joint reconstruction of PET-MRI by exploiting structural similarity. *Inverse Problems*, 31(1):015001.
[4] Knoll, F., Holler, M., Koesters, T., Otazo, R., Bredies, K., and Sodickson, D. K. (2017). Joint MR-PET reconstruction using a multi-channel image regularizer. *IEEE transactions on medical imaging*, 36(1):1–16.
[5] Rasch, J., Brinkmann, E.-M., and Burger, M. (2017). Joint reconstruction via coupled bregman iterations with applications to PET-MR imaging. *Inverse Problems*, 34(1):014001.
[6] He, D., Jiang, M., Louis, K., L., Maass, P., Page, T., (2019) Joint bi-modal image reconstruction of DOT and XCT with an extended Mumford-Shah functional, *The IEEE International Symposium on Biomedical Imaging* (ISBI).
[7] Tversky, A. (1977). Features of similarity. *Psychological review*, 84(4):327.
[8] Jiang, M., Maass, P., and Page, T. (2014). Regularizing properties of the Mumford–Shah functional for imaging applications. *Inverse Problems*, 30(3):035007.
[9] Page, T. S. (2015). *Image reconstruction by Mumford-Shah regularization with a priori edge information*. PhD thesis, Universität Bremen.

## Hamilton–Green solver for Photoacoustic Tomography

Marta M. Betcke
(joint work with Francesc Rul·lan)

### 1. Motivation

The increasing interest in imaging dynamic processes in living tissue resulted in a decade of intense research on numerical methods tailored to reconstruction from incomplete or subsampled data. While in ray based tomography e.g. X-ray CT, solution of the forward and adjoint problems scale proportionally with the number of detectors, it is not the case for the photoacoustic tomography (PAT) which for heterogenous sound speeds is usually be tackled by full wave solvers.

Large number of reconstruction methods relies on the ability of computing partial forward and adjoint operators e.g. Kaczmarz or recently gaining popularity stochastic methods e.g. stochastic gradient descent and extensions. To realise the benefits of such methods in PAT, we propose a ray based solver which effectively approximates the Green's function of the respective wave equation (underlying the forward or adjoint problem) along the trajectories of the Hamiltonian system (rays) derived from high frequency approximation.

## 2. High frequency approximation to the wave equation

We consider the linear scalar wave equation

$$\Box^2 u := \left( \frac{\partial^2}{\partial t^2} - c^2(x)\Delta \right) u = 0, \quad (t,x) \in (0,\infty) \times \mathbb{R}^d, \tag{1}$$

with $d = 2, 3$ and appropriate initial / boundary conditions to be specified later, where $c \in \mathcal{C}^\infty(\mathbb{R}^d)$ is the speed of the wave in heterogenous medium. In the high frequency limit $\omega \to \infty$, we look for the solution to (1) of the form, see e.g. [3]

$$u(t,x) = e^{i\omega\phi(t,x)} \sum_{k=0}^{\infty} A_k(t,x)(i\omega)^{-k}, \tag{2}$$

where $\phi(t,x)$ is the *phase*, $A_k$ the *coefficients of the amplitude* and $\omega$ the *frequency* of the oscillating wave. In this representation we expect the phase $\phi$ and the amplitude coefficients $A_k$ to vary at a much lower rate than the wave field $u$.

The *geometrical optics equations* are obtained by substituting the WKB expansion (2) into the wave equation (1) and equating terms of the same order to ensure that (1) holds down to $\mathcal{O}(\omega)$. In the limit $\omega \to \infty$ the terms of order $\mathcal{O}(\omega^{-n})$ for $n \geq 0$ can be neglected. The geometrical optics equations can be solved by e.g. phase-space methods, Hamilton-Jacobi methods or ray tracing methods. The proposed solver is based on *ray tracing*, which has been extensively studied from both the theoretical and numerical perspective, in particular in the context of seismic imaging [1] and ocean acoustics [4].

In the proposed solver, the role of the ray equations is primarily as means of a discretization of a domain $\Omega \subset \mathbb{R}^d$ rather than to obtain an explicit solution to the wave equation of the form (2). Therefore, we assume a fully implicit time dependence of the amplitude and phase, i.e. solely through the time dependence of the trajectory $x(t)$

$$u(t, x(t)) = A(x(t)) \exp(i\omega\phi(x(t)))$$

and solve the frequency domain version of the eikonal and transport equations.

### 2.1. **Phase.**

The frequency domain version of the eikonal equation reads

$$\|\nabla\phi\| = 1/c =: \eta. \tag{3}$$

Following the construction in [3], we introduce the Hamiltonian $H(x,p) = c(x)\|p\|$ defined in the phase space $\mathbb{R}^d \times \mathbb{R}^d$. Let $(x(t), p(t))$ be a bicharacteristic pair associated with this Hamiltonian. The Hamiltonian $H$ is constant along these bicharacteristics and is set to the initial value $H(x_0, p_0) = 1$, which corresponds to $\|p\| = \eta$. Therefore we have

$$\frac{\mathrm{d}x}{\mathrm{d}t} = \nabla_p H(x,p) = \frac{p}{\eta^2}, \qquad x(0) = x_0, \tag{4a}$$

$$\frac{\mathrm{d}p}{\mathrm{d}t} = -\nabla_x H(x,p) = \frac{\nabla\eta}{\eta}, \qquad p(0) = p_0, \qquad \|p_0\| = \eta(x_0), \tag{4b}$$

with the initial conditions $(x(0), p(0)) = (x_0, p_0)$. The solution $(x(t), p(t) = \nabla\phi(x(t)))$ admits following interpretation: $x(t)$ is the *trajectory* and $p(t)$ is the direction of propagation of the wave. Furthermore, for $\phi(t, x) = \phi(x(t))$ the time domain eikonal equation implies a linear relation between the time and phase

$$\phi(x(t)) = \phi(x_0) + t. \tag{5}$$

2.2. **Amplitude.** The amplitude is prescribed by the frequency domain version of the transport equation

$$2\nabla\phi \cdot \nabla A + \Delta\phi A = 0. \tag{6}$$

For the bicharacteristic pair $(x(t; x_0), p(t; p_0))$ the solution of (6) at a point $x(t; x_0)$ can be explicitly written as

$$A(x(t; x_0)) = A(x_0)\frac{\eta(x_0)}{\eta(x(t; x_0))}\sqrt{\frac{q(0; x_0)}{q(t; x_0)}}, \tag{7}$$

where $q$ is the determinant of the Jacobian of $x$ with respect to the initial data,

$$q(t; x_0) = \det J := \det \nabla_{x_0} x(t; x_0). \tag{8}$$

2.3. **Reversing rays.** The natural choice is to shoot the rays from the sensors into the domain. In [2] we showed that such trajectories are reversible and hence can be used by both the forward and adjoint solver and the reversed ray, phase and amplitude can be expressed in terms of the original quantities.

## 3. Hamilton-Green solver for the forward and adjoint problems

Here we restrict the presentation to the forward solver, while the adjoint solver follows similar construction for the time varying source problem which underlies the adjoint PAT operator. The details can be found in [2].

The forward PAT problem is an initial value problem

$$\Box^2 u = 0, \qquad (t, x) \in (0, \infty) \times \mathbb{R}^d, \tag{9a}$$

$$u_t(0, x) = 0, \qquad x \in \mathbb{R}^d, \tag{9b}$$

$$u(0, x) = u_0(x), \qquad x \in \mathbb{R}^d, \tag{9c}$$

with $u_0$ compactly supported on a domain $\Omega \in \mathbb{R}^d$. In the Hamilton-Green forward solver the time dependent pressure is obtained at each of the sensors separately using the cone of rays originating from this particular sensor. Using Green's formula for the solution to (9) we write the pressure $u(t, x_0)$ at a given time $t$ at a sensor location point $x_0$ as

$$u(t, x_0) = \int_{\mathbb{R}^d} \frac{1}{c^2(x')}\frac{\partial}{\partial t} G(t, x_0 \mid 0, x')u_0(x')\mathrm{d}x', \tag{10}$$

where $G(t, x \mid t', x')$ is an in general heterogeneous free-space Green's function. Assuming that the rays shot from $x_0 \notin \Omega$ do not develop a caustic in the domain $\Omega$ i.e. no two different rays from $x_0$ intersect in $\Omega$, and that they cover $\Omega$ sufficiently densely, these rays form a coordinate system for $\Omega$. In this coordinate system, using

Green's function identities and constructing high frequency approximation (7) to the heterogenous Green's function $G$ based on the homogeneous Green's function $G_0$ with sound speed $c(x_0)$, we obtain

$$u(t,x_0) \approx \eta(x_0) \int_0^T \frac{\partial}{\partial t} G_0(t+\ell, x_0 \mid 0, x_0) \\ \times \int_{\mathcal{S}^{d-1}} \eta(x(\ell,\theta;x_0)) \sqrt{q(0,\theta;x_0) q(\ell,\theta;x_0)}\, u_0(x(\ell,\theta;x_0))\, \mathrm{d}\theta\, \mathrm{d}\ell, \tag{11}$$

which we term the Hamilton-Green solution to (10).

## References


[1] V. Červený, *Seismic ray theory*, Cambridge university press (2005).

[2] F. Rullan, and M.M. Betcke, *Hamilton-Green solver for the forward and adjoint problems in photoacoustic tomography*, arXiv preprint arXiv:1810.13196 (2018).

[3] B. Engquist, and O. Runborg, *Computational high frequency wave propagation*, Acta numerica **12** (2003), 181–266.

[4] F.B. Jensen, and W.A. Kuperman, and M.B. Porter, and H. Schmidt, *Computational ocean acoustics*, Springer Science & Business Media (2000).


## Superresolution and Inverse Problems with Internal Sources


John C. Schotland

(joint work with Anna Gilbert, Jeremy Hoskins and Howard Levinson)


We have developed a simple model for localization microscopy [1, 2]. We consider a bounded domain $\Omega \subset \mathbb{R}^3$ that contains an inhomogeneous scattering medium along with a fixed number of internal quasi-monochromatic point sources with unknown locations, amplitudes, and phases. In each experiment the field from a single point source is measured at detectors positioned outside the medium. The measurements are performed one by one for each source. The inverse problem is to reconstruct the optical properties of the medium as well as the amplitude, phase and position of the sources.

The optical field $u$ obeys the Helmholtz equation

$$\Delta u + k^2 \left(1 + \eta(x)\right) u = -a e^{i\phi} \delta(x - x_0) \ , \tag{1}$$

where $k$ is the wavenumber, $\eta$ is the dielectric susceptibility of the scattering medium, and $x_0$, $a$ and $\phi$ denote the position, amplitude and phase of the source. For simplicity, we have not accounted for the effects of polarization and have employed a scalar model of the electromagnetic field. This model is of independent interest in acoustic imaging with micro-bubbles [3].

The field satisfies the integral equation

$$u(x) = u_0(x) + k^2 \int_\Omega G(x,y) \eta(y) u(y) dy \ , \tag{2}$$

where the Green's function $G$ is given by

$$G(x,y) = \frac{e^{ik|x-y|}}{4\pi|x-y|} \ . \tag{3}$$

The background field $u_0$ obeys (1) with $\eta = 0$ and is given by $u_0(x) = ae^{i\phi}G(x,x_0)$. In the far-zone of the scatterer, the field $u$ behaves as an outgoing spherical wave of the form

$$u(x) \sim \frac{e^{ik|x|}}{4\pi|x|}\left(ae^{i\phi}e^{-ik\hat{x}\cdot x_0} + A(x)\right) \ , \tag{4}$$

where the scattering amplitude $A$ is defined by

$$A(x) = k^2 \int_\Omega e^{-ik\hat{x}\cdot y}\eta(y)u(y)dy \ . \tag{5}$$

The classical formulation of the inverse scattering problem is to reconstruct the susceptibility from measurements of the scattering amplitude. Here the dependence of the scattering amplitude on the source is assumed to be known. In contrast, for the problem considered in this proposal, the amplitude, phase and position of the source are unknown and must be determined as part of the inverse problem. It is then natural to consider scattering data of the form

$$\Phi(x,x_0) = ae^{i\phi}e^{-ik\hat{x}\cdot x_0} + A(x,x_0) \ , \tag{6}$$

which corresponds to the amplitude of the spherical wave in (4) and the dependence of $A$ on the source position $x_0$ has been made explicit.

Let us suppose that the amplitude $a$, phase $\phi$ and position $x_0$ of the source are known. We will relax this assumption shortly. The scattering amplitude $A$ can then be determined from $\Phi$. Then making use of the reciprocity of sources and detectors and (4), we can solve (1) for $\eta$, thereby obtaining the inversion formula

$$\eta(x_0) = -\frac{1}{k^2\Phi(x,x_0)}\left(\nabla_{x_0}^2 A(x,x_0) + k^2 A(x,x_0)\right) \ . \tag{7}$$

We observe that for fixed $x$, the above result allows for a *local* reconstruction of $\eta(x_0)$ for $x_0 \in \Omega$. Moreover, there is in principle no limit to the resolution of the reconstruction, beyond that imposed by the accuracy of the forward model. It follows immediately that the inverse problem is well-posed.

Next, suppose that the susceptibility $\eta$ is known. We then wish to determine the amplitudes, phases and positions of the sources. We assume that the field is measured at $M$ detectors with positions $x_1,\ldots,x_M$, and that there are $N$ sources with amplitudes $a_1,\ldots,a_N$, phases $\phi_1,\ldots,\phi_N$ and positions $y_1,\ldots,y_N$. We then consider data $\Phi$ of the form $\Phi(x_m;a_n,\phi_n,y_n)$. We note that in any experiment, only one source is activate so that the entire data set can be collected for all $m$ and $n$. To find the source parameters, we solve the nonlinear least squares problem

$$(a_n,\phi_n,y_n) = \underset{(a,\phi,y)}{\arg\min} \sum_{m=1}^{M} \left|\Phi(x_m;a_n,\phi_n,y_n) - ae^{i\phi}e^{-ik\hat{x}_m\cdot y} - A(x_m,y_n)\right|^2 \ , \tag{8}$$

where $n = 1,\ldots,N$.

The inverse problem consists of recovering the susceptibility along with the amplitude, phase and positions of the sources from the scattering data. Its solution consists of two iterative steps, whereby an inverse source problem and an inverse scattering problem are alternately solved. In the first step, the sources are recovered from the current estimate of the susceptibility. In the second step, the susceptibility is reconstructed from the current estimate of the sources. The process is then repeated until convergence. The algorithm, which generates a sequence of approximations to the susceptibility $\eta^{(\ell)}$ and the sources $\{(a_n^{(\ell)}, \phi_n^{(\ell)}, y_n^{(\ell)})\}$ is given below.

### Reconstruction Algorithm

Put $A^{(0)}(x_m, y_n) = 0$ for all $m$ and $n$. Set $\ell = 1$.

Step 1.

- For all $n$,

$$(a_n^{(\ell)}, \phi_n^{(\ell)}, y_n^{(\ell)}) = \underset{(a,\phi,y)}{\arg\min} \sum_{m=1}^{M} \left| a e^{i\phi} e^{-ik\hat{x}_m \cdot y} - \Phi(x_m; a_n, \phi_n, y_n) + A^{(\ell-1)}(x_m, y_n) \right|^2 .$$

- For all $m$ and $n$,

$$\tilde{A}^{(\ell)}(x_m, y_n) = \Phi(x_m; a_n, \phi_n, y_n) - a_n^{(\ell)} e^{i\phi_n^{(\ell)}} e^{-ik\hat{x}_m \cdot y_n^{(\ell)}} .$$

Step 2.

- Solve for $\eta^{(\ell)}$ from $\tilde{A}^{(\ell)}$ using the inversion formula (7).
- For all $m$ and $n$,

$$A^{(\ell)}(x_m, y_n) = k^2 \int_\Omega e^{-ik\hat{x}_m \cdot y} \eta^{(\ell)}(y) u(y, y_n^{(\ell)}) dy .$$

$\ell \leftarrow \ell + 1$

A variant of the algorithm has been implemented and tested with numerically simulated data [2].

### References

[1] E. Betzig, G. H. Patterson, R. Sougrat, O. W. Lindwasser, S. Olenych, J. S. Bonifacino, M. W. Davidson, J. Lippincott-Schwartz and H. F. Hess, "Imaging intracellular fluorescent proteins at nanometer resolution," Science **313**, 1642–1635 (2006).

[2] A. Gilbert, H. Levinson and J. C. Schotland. "Imaging from the Inside Out: Inverse Scattering with Photoactivated Internal Sources," Opt. Lett. **43**, 3005–3008 (2018).

[3] C. Errico1, J. Pierre, S. Pezet, Y. Desailly, Z. Lenkei, O. Couture, and M. Tanter, "Ultrafast ultrasound localization microscopy for deep super-resolution vascular imaging," Nature **527**, 499–502 (2015).

## Selective-reconstruction Methods and A Microscopic-system Design for Spectral Computed Tomography

Qian Wang
(joint work with Hengyong Yu)

Spectral computed tomography (Spectral CT) is proposed by extending the conventional single spectral CT (SSCT) along the energy dimension. The state-of-the-art photon-counting-detector (PCD) based spectral CT scanners can identify photon energy and divide a whole X-ray spectrum into several channels. Although it has a superior energy-resolution, it meanwhile suffers seriously increased noise, which not only degrades the quality of reconstructed images but also decreases the material-decomposition accuracy. Moreover, some hardware-based barriers, such as the size dimension of PCD cells, further limit the spatial- resolution improvement of the spectral CT.

In this talk, Iwe focus on the selective-reconstruction methods for spectral computed tomography, which cover both dual spctral CT (DSCT) and multiple spectral CT (MSCT), both one- and two-step methods. Moreover, for a new developed spectral micro-CT system with both optical-magnification and energy-identification mechanisms, we investigate the corresponding high-resolution spectral-imaging methods.

**One-step method for DSCT [6].** First, by comparing SSCT and DSCT, we find that although the SSCT has the weaker capability for material distinguishing, the achieved SNR is dramatically higher than that of DSCT. Moreover, there is an interesting relationship, i.e., the decomposed results of DSCT can be viewed as modifications of reconstructed images of SSCT by removing some components and adjusting gray values. Furthermore, this structure-based feature can be mathematically described as a locally linear relationship. By incorporating this constraint into an optimization model, the reconstructed image of SSCT could work as a reference to effectively improve the smoothness of DSCT decomposed results. Motivated by the aforementioned facts, we develop an iterative method to improve the image quality of material decomposition, and the image-guided filtering technique [2, 3] will also be utilized.

When using the locally linear relationship, the SSCT images are employed as guidance to introduce both structural knowledge and smoothness constraint. This means their image quality plays a crucial role, i.e., any merit and fault will affect the final results of DSCT. Thus, we develop an additional preprocessing step to further improve the image quality of SSCT. The purpose of this preprocessing step lies in two aspects: well keeping all the structures and suppressing the noise. In the field of digital image processing, many methods can be used to achieve this goal, such as regularization based methods, transform domain filtering methods, statistical methods, local filtering methods, and so forth. However, in our problem, there are some specific characteristics: strong edges (between different materials) and weak edges (between similar materials) exist simultaneously. Particularly, the weak edges may have the same amplitude with noise. Thus, many methods

fail to keep these fine structures. By analyzing the features of weak edges, we find they can be well described by a locally statistical property, i.e., windowed inherent variation. The relative total variation (RTV) for extracting structure from texture [7] is extended for weak edge detection in this chapter. Thus, by using the preprocessed SSCT image as a good reference, the SNR of decomposed results is further increased.

**Two-step method for MSCT.** Different from directly employing the correlation among channel images of MSCT, we use a locally linear transform to establish a gradient sparsity in spectral dimension. Combining the piece-wise constant prior knowledge in the spatial domain, a three-dimensional (3D) gradient sparsity is formed. This property is further measured by an $L_0$-norm and incorporated into an optimization model as a regularization term. We also develop the corresponding iterative algorithm.

As a naturally further continuation, we innovatively employ a refined locally linear transform to convert the spectrum-related structural similarity to a gradient sparsity. Then we combine this newly established spetral sparsity with the original spatial sparsity to form a global three-dimensional (3D) sparse feature. We extend the two-dimensional (2D) $L_1$- and $L_0$-norm measurements to the corresponding 3D version, respectively. Meanwhile, we modify the spatial total-variation with spectral trace-norm measurement (TVLR) [1] to work on the transformed image volume. Based on the three new feature-measurements, we propose the corresponding optimization models and develop the corresponding iterative algorithms. Moreover, we perform experiments on both simulated and real data to verify the effectiveness and superiority of the proposed methods comparing with the unmodified versions (2D $L_1$- and $L_0$-norm minimization and TVLR method).

**One-step method for MSCT.** X-ray micro-computed tomography (micro-CT) has been widely employed in many practical applications, such as biomedicine, materials, electronic packaging, and the currently fashionable study of small-animal imaging. Several micro-CT systems are now commercially available and most of these share the geometrical or optical magnification mechanism to reach the spatial resolution of micron or submicron. However, due to the low power of the laboratory micro-CT X-ray source comparing with the one in industrial or medical usage, the gray resolution is usually not satisfactory. The reconstructed micro-CT images suffer low contrast and poor material discrimination. To overcome the weakness of grayscale contrast, we employ the state-of-the-art PCD in the micro-CT system.

PCDs are promising candidates for use in the next generation of x-ray CT scanners, foreseen benefits over conventional energy integrating detectors such as the better trade-off between noise and dose, improved spectral resolution and material distinguishing capabilities. By splitting and collecting photons into several energy bins, new applications are enabled, such as material-selective reconstruction, K-edge imaging, and so on.

For this application, we propose a multi-domain constraint based nonlinear optimization model, which leads to a one-step iterative selective-reconstruction process.

There are mainly three novelties as follows: A. the data fidelity term is based on the Kullback-Leibler distance measurement (I-divergence, KL distance), and lies in the photon counting domain. This design fully adopts the statistical feature of collected photons, and the further derivation achieves a natural transition to channel projection domain. B. the regularization term is based on the Mumford-Shah (MS) functional [4, 5], and lies in the material image domain. This smoothness term takes both gradient sparsity and edge information into account, thus effectively guarantees clear edges and suppresses noise in selective-material images. C. two multi-domain constraints are introduced, which builds bridges among channel projection domain, material projection domain, and material image domain. In this way, the data information in the photon counting domain can be transferred to the material image domain. And the prior knowledge of the material images can also be converted and then works on smoothing the photon or projection data.

**High-resolution spectral-imaging methods.** There is a novel design of a spectral micro-CT system with both optical-magnification and energy-identification mechanisms. For future research, we would like to develop some hardware-driven high-resolution spectral-imaging methods. We will also further optimize the software-development to improve the practical performance.

## References

[1] Jiyang Chu, Liang Li, Zhiqiang Chen, Ge Wang, and Hao Gao. Multi-energy CT reconstruction based on low rank and sparsity with the split-bregman method (MLRSS). pages 2411–2414, 2012.

[2] K. He, J. Sun, and X. Tang. Single image haze removal using dark channel prior. *IEEE transactions on pattern analysis and machine intelligence*, 33(12):2341–2353, 2011.

[3] K. He, J. Sun, and X. Tang. Guided image filtering. *IEEE transactions on pattern analysis and machine intelligence*, 35(6):1397–1409, 2013.

[4] Ming Jiang, Peter Maass, and Thomas Page. Regularizing properties of the Mumford-Shah functional for imaging applications. *Inverse Problems*, 30(3):035007, 2014.

[5] David Mumford and Jayant Shah. Optimal approximations by piecewise smooth functions and associated variational problems. *Communications on pure and applied mathematics*, 42(5):577–685, 1989.

[6] Qian Wang, Yining Zhu, and Hengyong Yu. Locally linear constraint based optimization model for material decomposition. *Physics in Medicine & Biology*, 62(21):8314, 2017.

[7] L. Xu, Q. Yan, Y. Xia, and J. Jia. Structure extraction from texture via relative total variation. *ACM Transactions on Graphics (TOG)*, 31(6):139, 2012.

## A Convex Formulation for Binary Tomography

Ajinkya Kadu

(joint work with Tristan van Leeuwen)

Binary tomography (BT) deals with the recovery of binary images from their tomographic projections. This problem is of particular interest in various forms of tomography, for example, imaging the structure of atomic crystals from electron microscopy. The BT problem is considered to be an NP-hard due to the discrete nature of the solution space. In this report, we present the convex formulation for

the BT problem, which solves the problem in polynomial time. From small-scale experiments, we conjecture that if the BT problem admits a unique solution, then our approach finds it. If it has multiple solutions, then the approach gives an intersection of these solutions.

The outline of the report is as follows: We first describe the BT problem and mention important challenges. Next, we propose the convex formulation from the Lagrangian duality principles. We then demonstrate our approach with small-scale experiments. Finally, we pose some open question regarding this work.

## 1. Binary Tomography

In the binary tomography problem, we are interested in finding an optimal vector of discrete nature whose tomographic projections are given by the observed data. In the simplest form, the BT problem is posed as

$$\text{find} \quad \mathbf{x} \in \mathcal{U}^n \qquad \text{subject to} \quad \mathbf{A}\mathbf{x} = \mathbf{b}, \tag{1}$$

where $\mathcal{U} = \{u_0, u_1\}$ is a discrete set, $\mathbf{A} \in \mathbb{R}^{m \times n}$ represents the tomographic matrix that models the discretized random transform, and $\mathbf{b} \in \mathbb{R}^m$ is the tomographic data. In general, the tomographic data contains noise, and hence, we can never satisfy the constraints in (1) exactly. To handle this issue, we pose the BT problem in a constrained least-squares form:

$$\mathbf{x}^\star \triangleq \underset{\mathbf{x} \in \mathcal{U}^n}{\operatorname{argmin}} \quad \|\mathbf{A}\mathbf{x} - \mathbf{b}\|^2, \tag{2}$$

where $\|\cdot\|$ denotes the Euclidean norm and $\mathbf{x}^\star$ is an optimal solution. There are many challenges well-known to the BT problem. We mention a few of them below:

- constraints are non-convex ($\mathcal{U}$ is a discrete set)
- Large null-space of $\mathbf{A}$ ($m \ll N$)
- solving (2) exactly (i.e., getting $\mathbf{x}^\star$) is not trivial
- Noise in $\mathbf{y}$ affects $\mathbf{x}^\star$
- considered as NP-hard (for m $\leq 3, N > 4$)

The existing algorithms for the BT problem can solve a few of these challenges. The current state-of-the-art algorithms are classified into four main areas: *(i)* Algebraic methods (iterative algorithms similar to Kaczmarz method), *(ii)* Stochastic sampling methods (based on sampling the pdf on the space of discrete images) *(iii)* Relaxation methods, these can be further sub-divided into two classes: *(a)* Convex relaxations (e.g., TV regularization), *(b)* Non-convex relaxations (e.g., level-set method, non-convex regularizers), and *(iv)* Heuristic algorithms (practical methods like DART).

## 2. Convex formulation

In this section, we first derive the convex formulation for an invertible $\mathbf{A}$. Consequently, we can find a convex formulation for all other cases, for example, limited tomography (where $m \ll n$), or tomographic data with Poisson noise.

Let us first reformulate (2) using an auxiliary variable $\boldsymbol{\phi} \in \mathbb{R}^n$:

$$\mathbf{x}^\star \triangleq \underset{\mathbf{x}}{\operatorname{argmin}} \left\{ \min_{\boldsymbol{\phi}} \tfrac{1}{2}\|\mathbf{A}\mathbf{x}-\mathbf{b}\|^2 \quad \text{subject to} \quad \mathbf{x} = \operatorname{sign}(\boldsymbol{\phi}) \right\}, \tag{3}$$

where $\operatorname{sign}(\cdot)$ is a signum function. We can write a Lagrangian for this problem as follows:

$$\mathcal{L}_\rho \triangleq \tfrac{1}{2}\|\mathbf{A}\mathbf{x}-\mathbf{b}\|^2 + \boldsymbol{\nu}^T\left(\mathbf{x} - \operatorname{sign}(\boldsymbol{\phi})\right),$$

where $\boldsymbol{\nu} \in \mathbb{R}^n$ is a Lagrange multiplier, also known as dual variable. This Lagrangian admits a following dual problem:

$$\min_{\boldsymbol{\nu}} \quad \tfrac{1}{2}\|\boldsymbol{\nu} - \mathbf{A}^T\mathbf{y}\|^2_{(\mathbf{A}^T\mathbf{A})^{-1}} + \|\boldsymbol{\nu}\|_1 \tag{4}$$

We first recognize that the dual problem (4) is a convex problem. This dual problem is categorized as least absolute shrinkage and selection operator (LASSO). LASSO has been widely studied in the literature, and many convex optimization methods exist to solve it. Once we get an optimal dual solution $\boldsymbol{\nu}^\star$, the primal solution is retrieved using $\mathbf{x}^\star = \operatorname{sign}(\boldsymbol{\phi}^\star) = \operatorname{sign}(\boldsymbol{\nu}^\star)$. The dual problem for limited tomography case (where $m \ll n$) is given in the following theorem.

**Theorem 1.** *For a limited tomography problem with* $\operatorname{rank}(\mathbf{A}) = m$ $(m \ll n)$*, the dual problem takes the following form:*

$$\min_{\boldsymbol{\mu}\in\mathbb{R}^m} \quad \tfrac{1}{2}\|\boldsymbol{\mu} - \mathbf{y}\|^2 + \|\mathbf{A}^T\boldsymbol{\mu}\|_1.$$

*The primal solution is retrieved using* $\mathbf{x}^\star = \operatorname{sign}\left(\mathbf{A}^T\boldsymbol{\mu}^\star\right)$.

## 3. Small-scale experiments

For demonstration, we perform small-scale experiments on $2\times 2, 3\times 3$ and $4\times 4$ pixels images. For tomographic projections, we work with row-sum, column-sum, diagonal and off-diagonal sums. In all the scenarios, our dual formulation retrieves the solution when there exists a unique solution to the primal problem. In the case of multiple solutions, the dual approach finds the commonalities between the solutions. All the results are tabulated in Table 3. Hence, We conjecture the following from this theorem.

**Conjecture 1.** *For a binary tomography problem with noiseless tomographic projections*

- *If the problem has a unique solution, then the dual approach retrieves it.*
- *If the problem has multiple solutions, then the dual approach retrieves the intersection of all solutions.*

*There is a subclass of the described binary tomography problem that is not NP-hard.*

| | $n$ | total | unique | multiple |
|---|---|---|---|---|
| $m=2$ | 2 | 16 | 14/14 | 2/2 |
| | 3 | 512 | 230/230 | 282/282 |
| | 4 | 65536 | 6902/6902 | 58541/58634* |
| $m=3$ | 2 | 16 | 16/16 | 0/0 |
| | 3 | 512 | 496/496 | 16/16 |
| | 4 | 65536 | 54272/54272 | 10813/11264* |
| $m=4$ | 2 | 16 | 16/16 | 0/0 |
| | 3 | 512 | 512/512 | 0/0 |
| | 4 | 65536 | 65024/65024 | 512/512 |

## 4. Conclusions

In this report, we present a convex program to retrieve binary solution from its tomographic projections. The convex program is based on the dual problem of the constrained least-squares form of the BT problem. From the small-scale experiments, we conjecture that *(i)* If a unique solution then the dual approach retrieves it, *(ii)* If multiple solutions then the dual approach retrieves the intersection of all solutions.

**Open Questions**:

- Does the strong duality hold?
- Proving the conjecture 1.
- Extension to discrete tomography (more than 2 grey levels).

## References

[1] A. Kadu, T. van Leeuwen, *A convex formulation for Binary Tomography*, IEEE Transactions of Computational Imaging 2019 (DOI:10.1109/TCI.2019.2898333)

## An exact inversion formula for cone beam vector tomography using the Laplace equation

Thomas Schuster

(joint work with Alexander Katsevich and Dimitri Rothermel)

Let $\mathbb{B}^3 := \{x \in \mathbb{R}^3 : |x| < 1\}$ be the open unit ball in $\mathbb{R}^3$. We consider the problem of reconsctructing a vector field $\mathbf{f}(x) = \big(\mathbf{f}_1(x), \mathbf{f}_2(x), \mathbf{f}_3(x)\big)^\top$, $x \in \mathbb{B}^3$, from its cone beam Doppler transform

$$[\mathbf{Df}](y(s), \Theta) = \int_0^\infty \mathbf{f}\big(y(s) + t\Theta\big) \cdot \Theta \, \mathrm{d}t, \tag{1}$$

where the source points $y$ are located on a trajectory $\Gamma \subset (\mathbb{R}^3 \backslash \overline{\mathbb{B}^3})$ outside the object and the unit vectors $\Theta \in S^2 := \partial\mathbb{B}^3$ are contained in a cone $\mathcal{C} \subset \mathbb{R}^3$ such that $\mathbb{B}^3 \subset (y + \mathcal{C})$ for every $y \in \Gamma$. Such a source trajectory, e.g., might be given by a circle at the plane $\{x_3 = 0\}$ with radius $r > 1$ and centered about the origin, $\Gamma = rS^2 \cap \{x_3 = 0\}$. We assume that $\Gamma$ has a parametrization $y : I \subset \mathbb{R} \to \mathrm{tr}(\Gamma) \subset \mathbb{R}^3$, $I \ni s \mapsto y(s) \in \mathrm{tr}(\Gamma)$, where $I$ is an interval. Data $g = \mathbf{Df}$ can, e.g., be acquired by ultrasound time-of-flight or Doppler shift measurements, where $\mathbf{f}$ is the velocity of a moving fluid (see [4, 7]) or by electron tomography, where $\mathbf{f}$ is a vector potential of the magnetic field (see [5]).

In two articles from 2013 [2] and 2017 [1] the authors developed an inversion formula for $\mathbf{D}$ which is exact for smooth, solenoidal vector fields and that relies on an important formula of Kazantsev and Schuster (c.f. [2]) which has to be seen as an analogon of Greangeat's famous formula for the classical cone beam transform of scalar functions. We recapitulate these results briefly and then describe an extension that can be used in general convex domains by solving a Dirichlet problem for the Laplace equation.

One key ingredient is the application of the 3D Radon transform and its splitting into a normal and tangential part on the sphere $S^2$. So, let for a vector field $\mathbf{f}$ on $\mathbb{R}^3$ the Radon transform be given as

$$[\mathbf{Rf}](p, \eta) = \int_{\eta^\perp} \mathbf{f}(p\eta + x)\, \mathrm{d}x\,, \qquad p \in \mathbb{R}\,,\ \eta \in S^2.$$

Note that, in contrast to $\mathbf{Df}$, the Radon transform $\mathbf{Rf}$ is again a vector field and not a scalar function. The Radon transform is invertible and the inversion formula is given as

$$\mathbf{f} = -\frac{1}{8\pi^2}\mathbf{R}^* \frac{\partial^2}{\partial p^2}\mathbf{Rf} \tag{2}$$

for sufficiently smooth $\mathbf{f}$. The mapping $\mathbf{R}^*$ is the $L^2$-dual operator to $\mathbf{R}$ which is represented by

$$[\mathbf{R}^*\mathbf{g}](x) = \int_{S^2} \mathbf{g}(x \cdot \eta, \eta)\, \mathrm{d}\eta, \qquad x \in \mathbb{B}^3,$$

and called *backprojection*. For fixed $\eta \in S^2$ we can split $\mathbf{R}$ into a part which is normal and a part which is tangential to the sphere. In this way we obtain the transforms

$$\begin{aligned}
[\mathbf{R}^{(nor)}\mathbf{f}](p, \eta) &= \big(\eta \cdot [\mathbf{Rf}](p, \eta)\big)\eta \\
[\mathbf{R}^{(tan)}\mathbf{f}](p, \eta) &= [\mathbf{Rf}](p, \eta) - [\mathbf{R}^{(nor)}\mathbf{f}](p, \eta)
\end{aligned}$$

representing the normal, respectively tangential, part of $\mathbf{Rf}$. With these notations we are able to formulate the main result of Kazantsev and Schuster from [3].

**Theorem 1.** *Let* $\mathbf{f} \in \mathcal{C}^\infty(\mathbb{B}^3, \mathbb{R}^3)$. *Then*

$$-\int_{S^2} [\mathbf{D}^{(even)}\mathbf{f}](x,\Theta)\delta''(\eta\cdot\Theta)\,\mathrm{d}\Theta = \big(\mathrm{div}_\eta[\mathbf{R}^{(tan)}\mathbf{f}](p,\eta)\big)\big|_{p=\eta\cdot x} + x\cdot\frac{\partial^2}{\partial p^2}[\mathbf{R}^{(tan)}\mathbf{f}](p,\eta)\big|_{p=\eta\cdot x} \tag{3}$$

*Here,* $\mathrm{div}_\eta$ *is the surface divergence on* $S^2$ *and by*

$$[\mathbf{D}^{(even)}\mathbf{f}](y,\Theta) := \frac{[\mathbf{Df}](y,\Theta)+[\mathbf{Df}](y,-\Theta)}{2}$$

*we denote the even part of* $\mathbf{Df}$.

To get injectivity for solenoidal vector fields, i.e. vector fields $\mathbf{f}$ satisfying $\nabla\cdot\mathbf{f} = 0$, the trajectory $\Gamma$ has to fulfill a Tuy condition of order 3, which is a generalization of the classical Tuy condition for scalar cone beam tomography.

**Definition 1** (Tuy condition of order 3)**.** *A trajectory* $\Gamma \subset (\mathbb{R}^3\backslash\overline{\mathbb{B}^3})$ *satisfies a Tuy condition of order* 3*, if any plane that passes* $\mathbb{B}^3$ *intersects the trajectory* $\Gamma$ *in at least* 3 *points that are not located on a line. That means to any* $p \in [-1,1]$ *and* $\eta \in S^2$ *there exist at least* 3 *parameters* $s_i = s_i(p,\eta) \in I$, $i = 1,2,3$ *with*

$$y_1\cdot\eta = y_2\cdot\eta = y_3\cdot\eta\,, \qquad y_i = y_i\big(s_i(p,\eta)\big), \qquad i = 1,2,3$$

*and* $y_1 - y_2$ *and* $y_2 - y_3$ *are not collinear.*

A trajectory $\Gamma$ that satisfies Tuy's condition of order 3 is, e.g., given by three circles of sufficiently large radius $r > 1$ centered about the origin and that are pairwise perpendicular to each other. Applying Tuy's condition and formula (3) yields, after according subtractions,

$$(y_1 - y_2)\cdot\frac{\partial^2}{\partial p^2}[\mathbf{R}^{(tan)}\mathbf{f}](s,\eta) = -\int_{S^2}\big(g(y_1,\Theta) - g(y_2,\Theta)\big)\delta''(\eta\cdot\Theta)\mathrm{d}\Theta, \tag{4a}$$

$$(y_2 - y_3)\cdot\frac{\partial^2}{\partial p^2}[\mathbf{R}^{(tan)}\mathbf{f}](s,\eta) = -\int_{S^2}\big(g(y_2,\Theta) - g(y_3,\Theta)\big)\delta''(\eta\cdot\Theta)\mathrm{d}\Theta, \tag{4b}$$

where $g = \mathbf{D}^{(even)}\mathbf{f}$ and $s = y_i\cdot\eta$. Since $\Gamma$ satisfies Tuy's condition, the system of linear equations (4) is uniquely solvable and we get

$$\frac{\partial^2}{\partial p^2}[\mathbf{R}^{(tan)}\mathbf{f}](p,\eta).$$

After an application of Radon's inversion formula (2) we finally obtain $\mathbf{R}^{(tan)}\mathbf{f}$. The strategy for computing the solenoidal part $\mathbf{f}^s$ of $\mathbf{f}$ from the data $\mathbf{Rf}$ is sketched in Figure 1.

Here,

$$H(\mathrm{div},\mathbb{B}^3) = \big\{\mathbf{f}\in L^2(\mathbb{B}^3)^3 : \langle\mathbf{f},\nabla v\rangle_{\mathbf{L}^2(\mathbb{B}^3)} = 0 \text{ for all } v\in\mathcal{C}_0^\infty(\mathbb{B}^3)\big\}$$

denotes the function space consisting of solenoidal vector fields $\mathbf{f}$. The two parts $\mathbf{f}_1$, $\mathbf{f}_2$ of the inversion formula are essentially computed by applying Radon's inversion formula to $\mathbf{R}^{(tan)}\mathbf{f}$, $\mathbf{R}^{(nor)}\mathbf{f}$, respectively. We remark that the calculation of

$$\begin{array}{ccccccc} \mathbf{Df} \Rightarrow \mathbf{R}^{(tan)}\mathbf{f} = \mathbf{R}^{(tan)}\mathbf{P}_{H(\mathrm{div},\mathbb{B}^3)}\mathbf{f} & \Rightarrow & \mathbf{R}^{(nor)}\mathbf{P}_{H(\mathrm{div},\mathbb{B}^3)}\mathbf{f} & \overset{+}{\Rightarrow} & \mathbf{R}\mathbf{P}_{H(\mathrm{div},\mathbb{B}^3)}\mathbf{f} \\ \Downarrow & & \Downarrow & & \Downarrow \\ \mathbf{f}_1 & & \mathbf{f}_2 & \overset{+}{\Rightarrow} & \mathbf{f}^s = \mathbf{P}_{H(\mathrm{div},\mathbb{B}^3)}\mathbf{f} \end{array}$$

FIGURE 1. Sketch of the inversion procedure

$\mathbf{R}^{(nor)}\mathbf{f}$ from $\mathbf{R}^{(tan)}\mathbf{f}$ is only possible, if the vector field $\mathbf{f}$ is solenoidal. We refer to [3] for details.

We generally assume that $\mathbf{f} \in \mathcal{C}^\infty(\overline{\mathbb{B}^3}, \mathbb{R}^3)$. Solving the system of 2 linear equations (4) gives

$$\partial_p^2[\mathbf{R}^{(tan)}\mathbf{f}](p,\alpha)_{|p=\alpha\cdot x} = \sum_{s_j \in \mathcal{S}_m} \phi(s_j, \mathcal{S}_m) G(s_j, \alpha),$$

where $\mathcal{S}_m$ denotes a triple of points from Tuy's condition,

$$G(s,\alpha) = -\int_{S^2} [\mathbf{D}^{(even)}\mathbf{f}](y(s),\Theta)\delta''(\Theta\cdot\alpha)\,\mathrm{d}\Theta$$

is calculated from the data and $\phi(s_j, \mathcal{S}_m)$ is computed by applying Cramer's rule for solving (4). The first part $\mathbf{f}_1$ can be computed by convolution-backprojection as follows:

$$\begin{aligned} \mathbf{f}_1(x) &= -\frac{1}{8\pi^2}\int_{S^2}\int_I \frac{|\alpha\cdot\dot{y}(s)|}{|x-y(s)|}\delta(\alpha\cdot\beta(s,x))\Phi(s,\alpha)G(s,\alpha)\,\mathrm{d}s\,\mathrm{d}\alpha \\ &= \frac{1}{8\pi^2}\int_I \frac{1}{|x-y(s)|}\int_0^{2\pi}[\Phi_{\theta\theta}(s,\alpha(\theta)) + \Phi(s,\alpha(\theta))] \\ &\quad \times \int_0^{2\pi} \frac{g(y(s), \cos\gamma\,\alpha^\perp(\theta) + \sin\gamma\,\beta)}{\cos^2\gamma}\,\mathrm{d}\gamma\,\mathrm{d}\theta ds, \end{aligned} \tag{5}$$

where $\alpha(\theta) = (\cos\theta, \sin\theta, 0)^\top$, $\beta = (0,0,1)^\top$ and

$$\Phi(s,\alpha) = |\alpha\cdot\dot{y}(s)| \sum_{m:s\in\mathcal{S}_m} \phi(s,\mathcal{S}_m) n_m(x,\alpha).$$

The weights $n_m$ are defined to sum up to 1 and pay tribute to the fact that there might be more than only one triple $\mathcal{S}_m$ satisfying Tuy's condition which is connected to the same plane.

The second part $\mathbf{f}_2$ can be calculated as

$$\begin{aligned} \mathbf{f}_2(x) &= -\frac{1}{8\pi^2}\int_{S^2} \frac{(\Psi(\eta)\cdot e_1)e_3 + (\Psi(\eta)\cdot e_2)e_2}{|\eta - x| + \eta\cdot(\eta - x)}\,\mathrm{d}\eta, \\ \Psi(\eta) &:= \int_{-1}^1 \phi(p)\partial_p^2\mathbf{R}^{(tan)}\mathbf{f}(p,\eta)\,\mathrm{d}p, \end{aligned}$$

where

$$e_1 = \frac{x - (\eta\cdot x)\eta}{|\eta\times x|}, \quad e_2 = \frac{\eta\times x}{|\eta\times x|}, \quad e_3 = \frac{\eta - x}{|\eta - x|}\times\frac{\eta\times x}{|\eta\times x|}$$

and $\phi(p)$ is given by

$$\phi(p) := (1-p^2)\sum_{n\geq 0}\frac{\check{\phi}_n}{\|C_n^{(3/2)}\|^2}C_n^{(3/2)}(p)$$

with appropriate coefficients $\check{\phi}_n$ and Gegenbauer polynomials $C_n^{(3/2)}$.

Whereas $\mathbf{f}_1$ can efficiently be computed by a convolution-backprojection algorithm, $\mathbf{f}_2$ is represented by a costly 3D integral. An alternative and stable computation of $\mathbf{f}_2$ can be performed by solving an appropriate boundary value problem for the Laplace equation. To see this we collect some properties of $\mathbf{f}_1$, $\mathbf{f}_2$ that can be deduced from the specific form of the inversion procedure in Figure 1. For details we refer to [1].

**Lemma 1.** *We have that*

*a)*

$$\nabla\times\mathbf{f}(x) = \nabla\times\mathbf{f}_1(x)\,, \qquad x\in\mathbb{B}^3.$$

*b)*

$$\mathbf{f}_2(x) = \mathbf{f}^s(x) - \mathbf{f}_1(x) = \nabla h(x)\,, \qquad x\in\mathbb{B}^3$$

*for a harmonic function $h$.*

*c) If $\mathbf{f}\in H_0(\mathrm{div},\mathbb{B}^3)$, where*

$$H_0(\mathrm{div},\mathbb{B}^3) = H(\mathrm{div},\mathbb{B}^3)\cap\left\{\mathbf{f}\in\mathbf{H}^1(\mathbb{B}^3) : \mathbf{f}\cdot\nu = 0 \text{ on } \partial\mathbb{B}^3\right\}$$

*(with $\nu(x)$ being the outer unit normal field to $\partial\mathbb{B}^3$), then*

$$[\mathbf{R}^{(nor)}\mathbf{f}](s,\eta)\equiv 0$$

*and hence $\mathbf{f}_2 = 0$.*

Lemma 1 inspires the following algorithm.

**Algorithm for computing $\mathbf{f}_2$.**

a) Compute $\mathbf{f}_1$ by convolution-backprojection as in (5).

b) Compute $[\mathbf{D}\mathbf{f}_1](y(s),\Theta)$ by numeric integration.

c) Subtract $g - \mathbf{D}\mathbf{f}_1 = \mathbf{D}\nabla h$ and observe that

$$[\mathbf{D}\nabla h](y(s),\Theta) = h\big(x_{out}(y(s),\Theta)\big) - h\big(x_{in}(y(s),\Theta)\big) \tag{6}$$

for certain points $x_{in}$, $x_{out}\in\partial\mathbb{B}^3$.

d) Get the Dirichlet data $h_{|_{\partial\mathbb{B}^3}}(\eta) = \mathcal{I}_{\vartheta^*}^{\triangle,3}(\eta)$ by solving the least squares problem

$$\vartheta^* = \arg\min_{\vartheta\in\mathbb{R}^{n\times m}}\sum_{k,l}\left|\mathcal{I}_\vartheta^{\triangle,3}(x_{out}^{k,l}) - \mathcal{I}_\vartheta^{\triangle,3}(x_{in}^{k,l}) - [\mathbf{D}\nabla h](y(s_k),\Theta_l)\right|^2$$

Here $\mathcal{I}_{\vartheta^*}^{\triangle,3}(\eta)$ denotes a cubic spline interpolation function on the unit sphere $S^2 = \partial\mathbb{B}^3$ which is associated with the partition $\triangle$ consisting of $n$ polar angles and $m$ azimuth angles.

e) Solve the Dirichlet problem

$$\begin{aligned} \Delta h(x) &= 0, \qquad x \in \mathbb{B}^3 \\ h(\eta) &= \mathcal{I}_{\vartheta^*}^{\triangle,3}(\eta), \qquad \eta \in \partial\mathbb{B}^3. \end{aligned}$$

f) Compute $\mathbf{f}_2 = \nabla h$.

**Remark 1.** *The algorithm above can easily be extended to general convex domains $D \subset \mathbb{R}^3$. Since the convolution-backprojection formula* (5) *for $\mathbf{f}_1$ does not depend on the specific domain, either, we obtain an inversion procedure for $\mathbf{D}$ on convex domains $D$ which is exact for smooth, solenoidal vector fields. Note, that by* (6) *the* true *harmonic function $h$ can only be determined up to a constant, but that does not affect the algorithm's outcome, since we are only interested in the gradient $\nabla h$.*

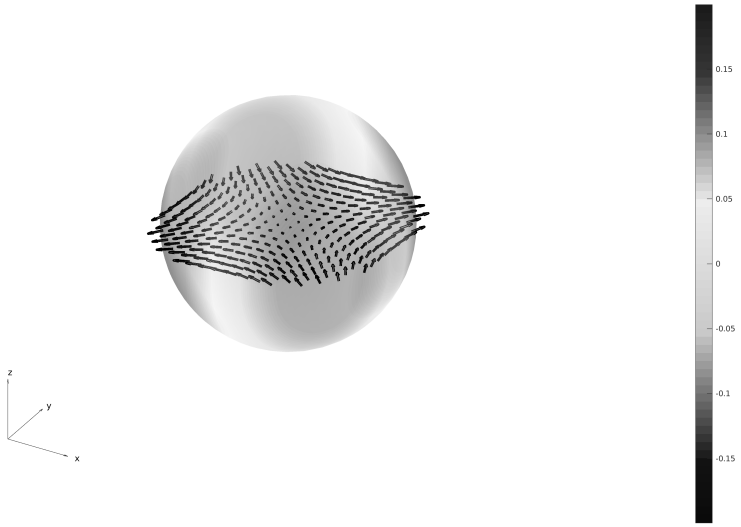


FIGURE 2. Reconstruction of $\mathbf{f}_2$ in the plane $\{x_3 = 0\}$ and Dirichlet data $h_{|_{\partial\mathbb{B}^3}} = \mathcal{I}_{\vartheta^*}^{\triangle,3}$ computed by cubic spline interpolation and solving a least squares problem.

A first numerical test was performed where the algorithm described above has been applied to the solenoidal vector field

$$\mathbf{f}(x) = (x_2, x_1, 0)^\top, \qquad x \in \overline{\mathbb{B}^3}.$$

Direct calculations show that

$$\partial_p^2[\mathbf{Rf}](p,\eta) = \begin{pmatrix} -6\eta_2 p\pi \\ -6\eta_1 p\pi \\ 0 \end{pmatrix}$$

and, applying the inversion formula (2),

$$\mathbf{f}_2 = \frac{2}{5}\begin{pmatrix} x_2 \\ x_1 \\ 0 \end{pmatrix},$$

whence $h(x) = \frac{2}{5}x_1x_2 + const$ follows. Figure 2 depicts the reconstructed $\mathbf{f}_2$ in the plane $\{x_3 = 0\}$ as well as the computed Dirichlet data $\mathcal{I}^{\triangle,3}_{\vartheta^*}(\eta)$ for $\eta \in \partial\mathbb{B}^3$.

Questions, that are currently open, are extensions of the inversion procedure to non-smooth vector fields such as $\mathbf{f} \in \mathcal{D}'(\mathbb{B}^3)$ and to simple Riemannian manifolds.

## References


[1] A. Katsevich, D. Rothermel, and T. Schuster, *An improved exact inversion formula for solenoidal fields in cone beam vector tomography*, Inverse Problems, **33** (2017), Special issue: 100 Years of the Radon transform, 19pp.

[2] A. Katsevich and T. Schuster, *An exact inversion formula for cone beam vector tomography*, Inverse Problems, **29** (2013), 13pp.

[3] S. Kazantsev and T. Schuster, *Asymptotic inversion formulas in 3D vector field tomography for different geometrie*, J. Inv. Ill-Posed Prob., **19** (2011), 769–799.

[4] S.J. Norton, *Tomographic reconstruction of 2-D vector fields: application to flow imaging*, Geophysics Journal, **97** (1988), 161–168.

[5] C. Phatak and D. Gürsoy, *Iterative reconstruction of magnetic induction using Lorentz transmission electron tomography*, Ultramicroscopy, **150** (2015), 54–64.

[6] T. Schuster, *The importance of the Radon transform in vector field tomography*, In *The first 100 years of the Radon Transform*, R. Ramlau, O. Scherzer (Eds.), Springer, 2019.

[7] G. Sparr, K. Stråhlén, K. Lindström and H.W. Persson, *Doppler tomography for vector fields*, Inverse Problems, **11** (1995), 1051–1061.


## Image reconstruction in Compton scattering tomography (CST)


Gaël Rigaud

(joint work with Bernadette N. Hahn)


Compton scattering imaging (CSI) is an arising imaging concept measuring and exploiting the scattering radiation as an object of interest is illuminated by an ionising source. Known as the Compton effect, the phenomena describes the collision/scattering of a photon with an electron leading to a loss of energy of the photon and a change of trajectory. The photon is measured by a camera in terms of energy delivering a precious information on the electron density. The measurement consists then in detecting the scattered photons for different detector positions and different level of energies.

The key information in order to exploit the first-order scattered radiation is given by the Compton formula which describes the loss of energy after a scattering event as

$$E_\omega = \frac{E_0}{1 + \frac{E_0}{511keV}(1 + \cos\omega)} \tag{1}$$

where $\omega$ stands for the scattering angle, $E_\omega$ for the energy of the scattered photon and $E_0$ for the energy of the monochromatic source S. Furthermore, the number of photons scattered **only once** at M and detected at D with energy $E_\omega$, noted $N_c$, satisfies:

$$\frac{d^2N_c}{d\mathbf{x}d\Omega_c} = \frac{I_0 r_e^2}{4} P(\omega) \frac{A_0(\mathbf{s},\mathbf{x})A_\omega(\mathbf{x},\mathbf{d})}{\|\mathbf{s}-\mathbf{x}\|^2\|\mathbf{x}-\mathbf{d}\|^2} n_e(\mathbf{x}), \tag{2}$$

where $n_e$ denotes the electron density, $\Omega_c$ the solid angle, $P(\omega)$ the Klein-Nishina probability and $A_\omega$ represents the attenuation of the photon beam (following from the Beer-Lambert law) along the photon travel at energy $E_\omega$. Due to the Compton formula eq. (1), a detected energy $E_\omega$ in the measured spectrum at D will correspond to scattering events which occured on a point M such that $\widehat{\mathrm{SMD}} = \omega$. This relation leads to specific manifolds, see Figure 1: in 2D, one gets two circular-arcs noted $T^2$, while in 3D one gets a spindle torus (inside or outside part according to the scattering angle) noted $T^3$. Now assuming D to be a *point* detector (sufficiently small) and only first-order scattering, the integration over the whole domain in eq. (2) leads to a generalized Radon transform along the manifold $T^n$ of the electron density $n_e$, *i.e.*

$$N_c(\mathbf{s},\mathbf{d},\omega) \approx \int_{\mathbf{x}\in T^n} \frac{A_0(\mathbf{s},\mathbf{x})A_\omega(\mathbf{x},\mathbf{d})}{\|\mathbf{s}-\mathbf{x}\|^2\|\mathbf{x}-\mathbf{d}\|^2} n_e(\mathbf{x}) d\mathbf{x}.$$

We can thus write the measured spectrum in 2D/3D CST data as weighted Radon transforms along circular-arcs/tori $T^n(\omega, v)$, *i.e.*

$$g(\omega, v) = \int\limits_{x_M \in T^n(\omega,v)} w(x_M,\omega,v) n_e(x_M) dx_M + \epsilon =: \mathcal{T}_w^n n_e(\omega, v) + \epsilon \qquad \text{with } v \in \mathbb{V}$$

with $v$ the movement of the source/detector pair (typically S fixed and D moving along a sphere) and $\epsilon$ some measurement noise.

Our work in [1, 2] addresses the problem of inverting the measured spectrum (modeled by generalized Radon transforms) in order to reconstruct (or at least extract features of) the electron density.

In 2D, the (unweighted) circular-arc Radon transform is strongly related to the standard Radon transform $\mathcal{R}$ using two given $C^\infty$-diffeomorphic mappings $\mathcal{M}_1$ and $\mathcal{M}_2$ so that

$$\mathcal{R}\mathcal{M}_2 = \mathcal{M}_1\mathcal{T}_1^2.$$

Hence we deduce inverse formula as well as some properties (SVD, Sobolev estimates, ...). The problem becomes harder when taking into account the weight function (physical phenomena). In this case, we consider a contour extraction strategy

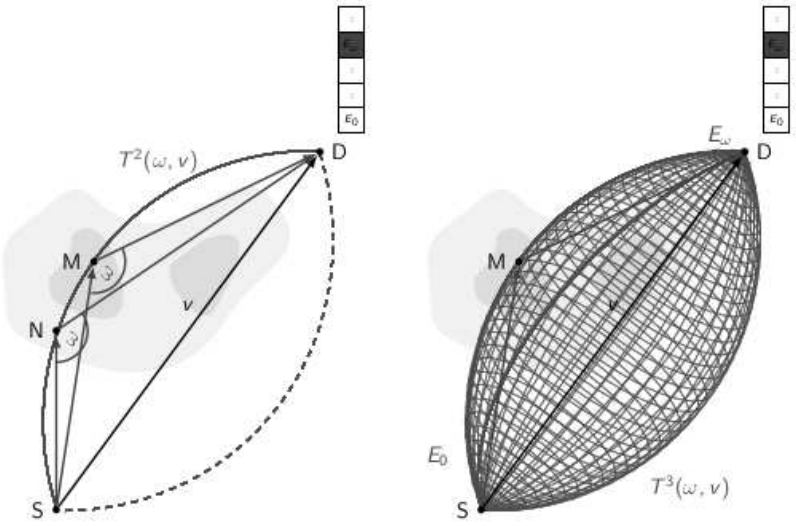


FIGURE 1. Geometry involved in 2D (left) and 3D (right) CST.

in 2D as well as in 3D. Our work motivates the use of filtered backprojection-type reconstruction techniques to address the problem of inverting the generalized Radon transform $\mathcal{T}_w^2$ for $n = 2, 3$.

In particular, in 3D, we extend the results derived by Beylkin in [3] to a different class of isosurfaces. We define a manifold $\mathfrak{M}$ characterized by a function $\phi$ via

$$\mathbf{x} \in \mathfrak{M}(p, \theta) \quad \Longleftrightarrow \quad \phi(\mathbf{x}, \theta) = p, \qquad (p, \theta) \in \Pi \times \Theta$$

with $\dim(\Pi) = 1$ and $\dim(\Theta) = 2$ where its characteristic function $\phi$ satisifies the following conditions:

(1) $\phi(\mathbf{x}, \theta)$ is a real-valued $C^\infty$ function on $\Omega \times \Theta$.
(2) $\left\{ \frac{\nabla_{\mathbf{x}} \phi(\mathbf{x}, \theta)}{\|\nabla_{\mathbf{x}} \phi(\mathbf{x}, \theta)\|}, \theta \in \Theta \right\} = S^2$.
(3) The function $h(\mathbf{x}, \theta)$ in $\Omega \times \Theta$ defined as

$$h(\mathbf{x}, \theta) = |det\left(\nabla_{\mathbf{x}} \phi(\mathbf{x}, \theta), \partial_{\theta_1} \nabla_{\mathbf{x}} \phi(\mathbf{x}, \theta), \partial_{\theta_2} \nabla_{\mathbf{x}} \phi(\mathbf{x}, \theta)\right)|$$

is nowhere 0.
(4) The zero sets of $\{\phi(x, \cdot) - \phi(y, \cdot)\}$, after the change of variable induced by condition (2), is a smooth closed curve on the unit sphere around the vector $(x - y)$ normalized.

Defining the generalized 3D Radon transform along $\phi$,

$$\mathcal{R}_c f(p, \theta) = \int_\Omega c(\mathbf{x}, p, \theta)\ f(x)\ \delta(p - \phi(\mathbf{x}, \theta)) d\mathbf{x}, \quad (p, \theta) \in \Pi \times \Theta,$$

and defining the following *backprojection* operator

$$\mathcal{R}_b^* g(\mathbf{y}) = \int_\Theta b(\mathbf{y}, \theta)\ g(\phi(\mathbf{y}, \theta), \theta)\ h(\mathbf{y}, \theta) d\theta \quad \text{for} \quad \mathbf{y} \in \Omega,$$

then the reconstruction formula is given by

$$\mathcal{K}f := \frac{-1}{8\pi^2}\mathcal{R}_b^*\partial_p^2 g = f + \mathcal{E}f, \qquad \mathcal{R}_c f = g \tag{3}$$

with $b(\mathbf{y},\theta) = (c(\mathbf{y},\phi(\mathbf{y},\theta),\theta))^{-1}$ and $\mathcal{E}$ a continuous integral operator from $L^2(\Omega)$ to $L^2(\Omega)$ with a smooth ($C^\infty$-) kernel.

Assuming that the sought-for function is described by its contours (jumps), the proposed reconstruction formula eq. (3) preserves the contours (position and magnitude) of $f$. In this case, eq. (3) delivers an "*inversion formula*" for piecewise constant functions.

Simulation results for various configurations on synthetic 2D/3D CST data prove the interest of the approach to solve partially in an efficient way the inverse problem associated to Compton scattering.

## References


[1] G. Rigaud, *Compton Scattering Tomography: Feature Reconstruction and Rotation-Free Modality* , SIAM J. Imaging Sci. **10**(4) (2017), 2217–2249.

[2] G. Rigaud and B.N. Hahn *3D Compton scattering imaging and contour reconstruction for a class of Radon transforms* Inverse Problems **34** (2018) 075004 (22pp).

[3] G. Beylkin *The inversion problem and applications of the generalized Radon transform* Communications on Pure and Applied Mathematics **37** (1984) 579–599.


## Real time reconstruction for 4D magnetic particle imaging


Christina Brandt

(joint work with Andreas Hauptmann)


Magnetic particle imaging (MPI) is a new imaging modality which can capture fast dynamic processes in 3D volumes, based on the non-linear response of the magnetic particles to an applied magnetic field [1,2]. Possible medical applications are vascular imaging, device tracking, stem cell imaging and magnetic hyperthermia, see [3] for an overview. However, even in the case of time-lapse data, the standard reconstruction approach consists in static regularization methods such as classical Tikhonov regularization applied to each single time frame [3]. We propose a spatio-temporal regularization which can be efficiently solved using a low rank approximation of the forward operator. We illustrate our approach with real data of a potential application, i.e. real data of a catheter tracking experiment [4,5].

## References


[1] B. Gleich and J. Weizenecker, *Tomographic imaging using the nonlinear response of magnetic particles*, Nature **435** (2005), 1214-1217.

[2] J. Weizenecker, B. Gleich, J. Rahmer, H. Dahnke and J. Borgert, *Three-dimensional real-time in vivo magnetic particle imaging*, Physics in Medicine and Biology, **54** (2009), L1-L10.

[3] T. Knopp, N. Gdaniec, and M. Möddel, *Magnetic particle imaging: from proof of principle to preclinical applications*, Physics in Medicine & Biology, **62** (2017), R124-R178.

[4] J. Haegele, J. Rahmer, B. Gleich, J. Borgert, H. Wojtczyk, N. Panagiotopoulos, T. Buzug, J. Barkhausen, F. Vogt, *Magnetic particle imaging: visualization of instruments for cardiovascular intervention Radiology*, Radiological Society of North America **265** (2012), 933-938.
[5] M. Storath, C. Brandt, M. Hofmann, T. Knopp, J. Salamon, A. Weber and A. Weinmann, *Edge preserving and noise reducing reconstruction for magnetic particle imaging*, IEEE Transactions on Medical Imaging **36** (2017), 74-85.

## Bayesian inversion and uncertainty quantification for $X$-ray transforms

Richard Nickl
(joint work with Francois Monard and Gabriel P. Paternain)

We consider the statistical inverse problem of recovering a function $f : M \to \mathbb{R}$, where $M$ is a smooth compact Riemannian manifold with boundary, from measurements of general $X$-ray transforms $I_a(f)$ of $f$, corrupted by additive Gaussian noise. For $M$ equal to the unit disk with 'flat' geometry and $a = 0$ this reduces to the standard Radon transform, but our general setting allows for anisotropic media $M$ and can further model local 'attenuation' effects – both highly relevant in practical imaging problems such as SPECT tomography. We study a nonparametric Bayesian inference method based on standard Gaussian process priors for $f$. The posterior reconstruction of $f$ corresponds to a Tikhonov regulariser with a reproducing kernel Hilbert space norm penalty that does not require the calculation of the singular value decomposition of the forward operator $I_a$. We prove Bernstein-von Mises theorems for a large family of one-dimensional linear functionals of $f$, and they entail that posterior-based inferences such as credible sets are valid and optimal from a frequentist point of view. In particular we derive the asymptotic distribution of smooth linear functionals of the Tikhonov regulariser, which attains the semi-parametric information lower bound. The proofs rely on an invertibility result for the 'Fisher information' operator $I_a^* I_a$ between suitable function spaces, a result of independent interest that relies on techniques from microlocal analysis. We illustrate the performance of the proposed method via simulations in various settings.

The precise results can be found in the paper [1]. For background on infinite-dimensional statistical models see [2].

### References

[1] F. Monard, R. Nickl, G.P. Paternain, *Efficient Bayesian Nonparametric Inference for $X$-ray transforms*, Annals of Statistics **47** (2019), 1113–1147.
[2] E. Giné, R. Nickl, *Mathematical foundations of infinite-dimensional statistical models*, Cambridge University Press, 2016.

# Regularization by architecture: A deep prior approach for inverse problems

Peter Maass
(joint work with Daniel Otero Baguer, Sören Dittmer and Tobias Kluth)

## 1. The deep prior approach

Deep image priors (DIP) have been recently introduced as a machine learning approach for some tasks in image processing [1,5]. Usually, such machine learning approaches utilize large sets of training data, hence, it was somewhat surprising that deep image priors are based on a single data point $y^\delta$. The task of DIP is to train a network $\varphi_W : X \to X$ with parameters $W$ by minimizing the simple loss function

$$\|A\varphi_W(z) - y^\delta\|^2, \tag{1}$$

for a *fixed* $z$. We are interested in the analysis of DIP approaches and in particular in proving some convergence properties for iteratively minimizing (1). We will do so in the context of inverse problems, which are modeled by a non-linear or linear operator $A : X \to Y$ between Hilbert spaces $X$ and $Y$. Contrary to the applications in image processing mentioned above, we assume, that the range of $A$ is not closed, which implies, that the inversion or any generalized type of inversion is ill-posed [2–4]. Typical examples are compact linear operators or parameter-to-state mappings for partial differential equations.

## 2. Analytic deep prior

In this section we consider linear operators $A$ and aim at rephrasing DIP, i.e. the minimization of (1) with respect to $W$, as an approach for learning optimized Tikhonov functionals. This change of view, i.e. regarding deep inverse priors as an optimization of functionals rather then networks, opens the door for analytic investigations.

**Definition 2.** *Consider a fully connected neural network $\varphi_W : X \to X$ with $L$ layers, whose activation function is a proximal mapping $\mathrm{Prox}_{\alpha\lambda R}$ with respect to a convex functional $R : X \to \mathbb{R}$, i.e.*

$$\varphi_W(z) = x^L, \tag{2}$$

*where*

$$x^{k+1} = \operatorname*{Prox}_{\alpha\lambda R}(Wx^k + b) \tag{3}$$

*and $x^0 = z$. Further assume that $W \in \mathcal{L}(X, X)$ can be decomposed as $W = I - B^*B$ with a bounded operator $B : X \to Y$ and that the bias satisfies $b = \lambda B^* y^\delta$. We define the associated Tikhonov functional $J_B(x) = \frac{1}{2}\|Bx - y^\delta\|^2 + \alpha R(x)$ and assume that a unique minimizer $x(B) = \arg\min J_B(x)$ exists. We call this setting*

*an analytic deep prior if $W$, resp. $B$, is trained from a single data point $y^\delta$ by gradient descent applied to*

$$\min_B \|Ax(B) - y^\delta\|^2. \tag{4}$$

We examine the training process for computing $W$, resp. $B$, in the setting of such analytic deep prior models. If we assume that the output $\varphi_W(z)$ of the network converges to $x(B)$, this can be either regarded as training a neural network or as determining an optimized Tikhonov functional.

For some specific examples, such as if we assume the unrealistic case that $x^+ = u_k$, where $u_k$ is a singular function of $A$ ($A$ having a singular value decomposition $\{(u_i, \sigma_i, v_i)\}_i$), we can analytically compute the update steps for $B$

$$B^{\ell+1} = B^\ell - c_\ell v_k u_k^* \tag{5}$$

We further assume, that the measurement noise in $y^\delta$ is in the direction of this singular function, i.e. $y^\delta = (\sigma_k + \delta)v_k$.

A similar example is illustrated in the following section but considering arbitrary noise instead. We can see that the final result for the matrix $B$ contains some patterns that match the update from Equation 5.

## 3. Numerical experiments

3.1. **Academic example.** We now apply the analytic deep image prior to solve a linear inverse problem posed via the integral operator and the proximal operator induced by $R(x) = \frac{1}{2}\|x\|^2$. We choose $x^\dagger \in \mathbb{R}^n$ to be one of its singular vectors $u$ and set the noisy data $y^\delta = A_n x^\dagger + \tau$ with $\tau \sim \mathcal{N}(0, \sigma^2 \mathbb{1}_n)$ and $\sigma$ equals 10% of the largest coefficient of $y^\dagger$.

We aim to recover $x^\dagger$ from $y^\delta$ considering the setting established in Def. 2. For most of the choices of $\alpha$, except if it is too small which causes computations to be highly unstable, the training of $B$ converges to a matrix $B_{opt}$, such that $x(B_{opt})$ has a smaller true error than the standard Tikhonov reconstruction $x_T$, see Figure 3.1. This is due to the fact that the Tikhonov approach tends to over smooth the reconstructions. The analytic deep prior approach seems in principle to behave differently and shows some promising results.

3.2. **Magnetic particle imaging.** In this subsection we apply the DIP network (U-Net) described by [1] for solving the reconstruction problem in magnetic particle imaging (MPI) [6–8] for a measured linear operator and two different scanned phantoms. Table 1 shows a comparison with reconstructions via Kaczmarz with $\ell_2$ regularization and via proximal gradient descent for $\ell_1$ regularization. Each of the two phantoms used consisted of two parallel lines of different length. On one phantom 2mm apart and on the other 4mm apart.

We would like to point out that of these methods only the DIP is capable of correctly separating the two lines in the case of the 2mm phantom.
For further information and more plots see our arXiv preprint [9].

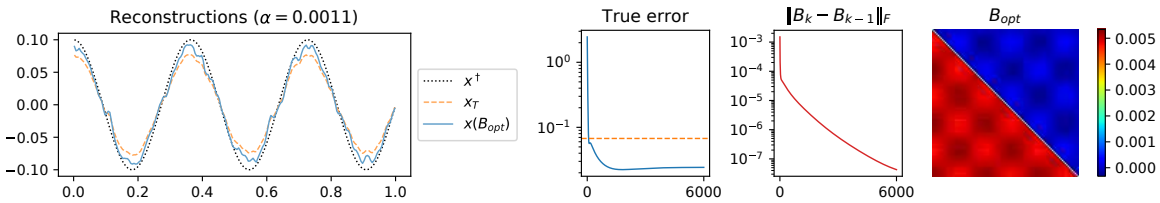


FIGURE 1. Reconstructions for fixed $\alpha$. The broken line in the second plot indicates the true error of the standard Tikhonov solution $x_T$. In the third plot one can check that $B$ indeed converges to some matrix $B_{opt}$, which is shown in the last plot. The networks were trained with the standard gradient descent method and a learning rate of 0.0011 over 6000 training iterations.

TABLE 1. Reconstructions for "4mm" and "2mm" phantom. Pictures taken at University Medical Center Hamburg-Eppendorf by T. Kluth.

| Phantom | Kaczmarz with $\ell_2$ | $\ell_1$ | DIP |
|---|---|---|---|
| 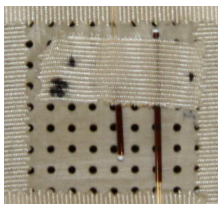 | 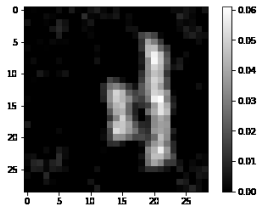 | 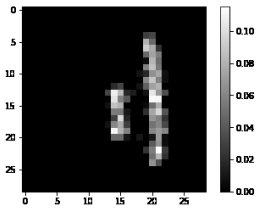 | 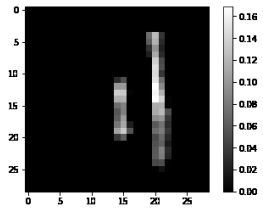 |
| 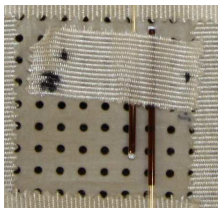 | 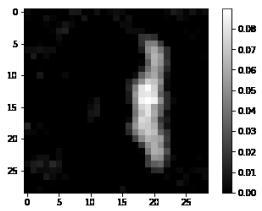 | 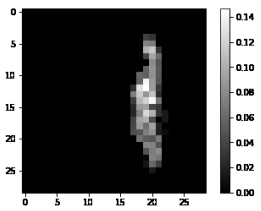 | 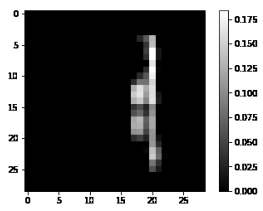 |

The authors would like to thank P. Szwargulski and T. Knopp from the University Medical Center Hamburg-Eppendorf for their support in conducting the experiments.

## REFERENCES

[1] Ulyanov, D., Vedaldi, A., Lempitsky, V.S.: Deep image prior. arXiv preprint arXiv:1711.10925 (2017)
[2] Engl, H.W., Hanke, M., Neubauer, A.: Regularization of inverse problems, *Mathematics and its Applications*, vol. 375. Kluwer Academic Publishers Group, Dordrecht (1996)
[3] Rieder, A.: Keine Probleme mit inversen Problemen: eine Einführung in ihre stabile Lösung. Vieweg, Wiesbaden (2003)
[4] Louis, A.K.: Inverse und schlecht gestellte Probleme. Vieweg+Teubner Verlag, Wiesbaden (1989)
[5] Van Veen, D., Jalal, A., Price, E., Vishwanath, S., Dimakis, A.G.: Compressed sensing with deep image prior and learned regularization. arXiv preprint arXiv:1806.06438 (2018)

[6] Gleich, B., Weizenecker, J.: Tomographic imaging using the nonlinear response of magnetic particles. Nature **435**(7046), 1214–1217 (2005)
[7] Knopp, T., Gdaniec, N., Möddel, M.: Magnetic particle imaging: from proof of principle to preclinical applications. Physics in Medicine and Biology **62**(14), R124 (2017)
[8] Kluth, T.: Mathematical models for magnetic particle imaging. Inverse Problems **34**(8), 083001 (2018).
[9] Dittmer, S., Kluth, T., Maass, P., Otero Baguer, D.: Regularization by architecture: A deep prior approach for inverse problems. arXiv preprint arXiv:1812.03889 (2018)

## Electrical impedance tomography and virtual X-rays

Samuli Siltanen

Electrical impedance tomography (EIT) is a non-invasive imaging method. EIT is based on feeding electric currents into a physical body through electrodes placed on the surface of the body and measuring the resulting voltage potentials at the electrodes. The aim is to recover the electric conductivity distribution inside the body; this in turn is useful information in medical imaging and nondestructive testing.

The mathematical model of EIT is the *inverse conductivity problem* introduced by Alberto Calderón in [1]. More precisely, consider the elliptic equation

$$\nabla \cdot \sigma \nabla u = 0 \quad \text{in } \Omega, \tag{1}$$

where $u(x)$ represents the electric potential and $0 < c \leq \sigma(x) \leq C$ represents the conductivity. In theoretical work it is more convenient to consider voltage-to-current measurements instead of current-to-voltage Applying a known voltage on the boundary of the region $\Omega \subset \mathbb{R}^2$ corresponds to the Dirichlet boundary condition

$$u = f \quad \text{on } \partial\Omega, \tag{2}$$

and knowledge of the resulting current density distribution gives rise to the Neumann boundary condition

$$\sigma \frac{\partial u}{\partial \nu} = g \quad \text{on } \partial\Omega. \tag{3}$$

Thus, the physical interpretation of the Dirichlet-to-Neumann map $\Lambda_\sigma$ is knowledge of the resulting current distributions on the boundary of $\Omega$ corresponding to all possible voltage distributions on the boundary.

In [2] we showed that using complex geometrical optics (CGO) solutions and a novel Fourier transform technique one can extract from $\Lambda_\sigma$ information about the wavefront set of $\sigma$. The information can approximately be interpreted as on one-dimensional X-ray projection image of the singularities of $\sigma$.

Measurement noise prevents the computation of high-resolution tomographic profiles of $\sigma$ in practice. The Fourier transform involved in the construction needs to be so heavily windowed that the resulting profiles are blurred beyond simple interpretation. However, we believe that machine learning can be applied for further processing and application of EIT tom, for example, diagnosing stroke.

In our future research we will study the proposed CGO solution technique as a nonlinear feature extraction step before machine learning. The following benefits are expected:

- Smaller network is enough for good reconstruction
- Less training data is needed for learning
- Better interpretability (less black-box)
- Robustness against random or hostile noise

## References

[1] A. P. Calderón, *On an inverse boundary value problem*, In Seminar on Numerical Analysis and its Applications to Continuum Physics, Soc. Brasileira de Matemàtica (1980), pp.65–73.
[2] A. Greenleaf, M. Lassas, M. Santacesaria, S. Siltanen and G. Uhlmann, *Propagation and recovery of singularities in the inverse conductivity problem*, Analysis and PDE **11**(8) (2018), 1901–1943.

## Dynamic reconstruction in tomographic microscopy

Rajmund Mokso

(joint work with Viktor Nikitin, Marcus Carlsson and Fredrik Andersson )

X-ray tomographic microscopy may be performed with conventional X-ray sources or using synchrotron radiation. In the first case the cone-beam geometry is considered for the reconstruction algorithms, while in the latter we are working in parallel beam geometry. Another specificity of synchrotron X-ray imaging is the high speed. Individual angular projections are acquired on a ms time-frame and the entire tomographic dataset in a fraction of a second. This enables time resolved studies of dynamic processes at the microsecond spatial and sub-second temporal resolution. The data production rate is large and consequently the tomographic reconstruction must be fast to keep up. Despite this fast acquisition In dynamic tomography the sample is often evolving quicker, giving rise to motion artefact. We developed a new method for handling changes in the structure of the sample during the acquisition process. The method is based on decomposition into basis functions in the time domain.

Three classes of methods were developed earlier. The first class of methods is based on estimating a priori information about the actual motion [1–3] . The second class of methods for suppressing motion artifacts takes into account regularization in a non-local fashion. The methods analyze the similarity between corresponding patches at different time steps, even if the patches have moved to another location [4]. The third class of methods for four-dimensional tomographic reconstruction is built upon the concept of compressed sensing, which employs sparsity promoting algorithms [5, 6] . In this work, we use the concept of compressed sensing in the way that data in the temporal direction is represented by a linear combination of appropriate basis functions, and the $L_1$ norm minimization is performed for the gradient in both spatial and temporal variables. The choice of basis functions depends on the motion structure inside the object and can be

determined according to measured data. For solving the obtained non-smooth regularization problem, we adopt the primal-dual Chambolle-Pock algorithm [7]. Our motivation were mainly time resolved tomographic datasets acquired with fast synchrotron based X-ray tomographic microscopy. In these datasets part of the sample is unstable during the acquisition due to the dynamic nature of the imaged processes, such as rheology of liquid foams.

## 1. Time domain decomposition

Let $f(x, y, z, t)$ be a function which represents a three-dimensional object dynamically changing in time $t$. The object is rotated continuously and projection data is measured for angles $\theta$ and for the radial direction $s$. The projection operator is then described by integration over the lines through the object state at time $t$, which is connected to the rotation angle $\theta$. We assume a linear connection between the angle $\theta$ and the time $t$, i.e. $\theta = \alpha t$, where the parameter $\alpha$ in practice is related to the speed of rotation and the detector exposure time. The projection operator $\mathcal{R}_\alpha : \mathbb{R}^3 \times [0, T] \to \mathbb{R}^2 \times S^1$ where $S^1$ denotes the unit circle, is defined by

$$\mathcal{R}_\alpha f(s, z, \theta) = \iiint f(x, y, z, t)\delta(x\cos\theta + y\sin\theta - s)\delta(\theta - \alpha t)dx\,dy\,dt. \tag{1}$$

The corresponding adjoint operator $\mathcal{R}^*_\alpha : \mathbb{R}^2 \times S^1 \to \mathbb{R}^3 \times [0, T]$ is defined as follows

$$\mathcal{R}^*_\alpha g(x, y, z, t) = \iint g(\theta, s, z)\delta(x\cos\theta + y\sin\theta - s)\delta(\theta - \alpha t)ds\,d\theta. \tag{2}$$

The inverse problem of recovering the function $f$ from the measurements $g = \mathcal{R}_\alpha f$ has plenty of possible solutions. The non-uniqueness is caused by the fact that at each particular time frame $t$ there exist only one projection related to the angle $\theta = \alpha t$, which is surely not enough to recover a unique object structure. In this case, regularization can be used to introduce assumptions on the solution. The traditional approach to finding a solution $f_o$ is by minimising the data fidelity term as

$$f_o = \arg\min_f \left\{ \frac{1}{2} \|\mathcal{R}_\alpha f - g\|_2^2 \right\}. \tag{3}$$

This term is commonly used in static tomography where the object does not change during 180 degrees rotation. Since the cost function is quadratic, one can use gradient-based methods such as the standard least-squares iteration scheme, or the conjugate gradient least-squares scheme with a faster rate of convergence. It is also common to use tomography specific methods. Indeed, recovering the object structure from a limited number of the measured projection angles can be done by algebraic reconstruction methods which does not operate with data along the time axis and, consequently, could produce a big number of possible solutions for (3). To reduce the number of possible solutions we introduce an additional assumption on the object movement. Let us assume that the motion at each concrete space

sample $(x, y, z)$ can be approximated by a linear combination of a small number of basis functions $\{\varphi_j(t)\}_{j=0}^{M-1}$, i.e.,

$$f(x, y, z, t) \approx \sum_{j=0}^{M-1} \mathsf{f}_j(x, y, z)\varphi_j(t), \tag{4}$$

where $\mathsf{f} = \{\mathsf{f}_j(x, y, z)\}_{j=0}^{M-1}$ are decomposition coefficients. In this case an approximation to $f$ with respect to the $t$-variable, for each fixed $x, y, z$, lies in a (low-dimensional) subspace $\mathcal{W} = \text{span}\{\varphi_0(t), \ldots, \varphi_{M-1}(t)\}$. The choice of basis functions $\varphi_j$ for better approximation depends on the motion structure. As a straightforward example, one can choose the Fourier basis with a low number of coefficients to represent slow motions, and a high number of coefficients to represent rapid motions. Other possible functions for representation include Haar wavelets, Heaviside step functions. We first applied the method to liquid foam rheology [8], the next step is optimise the method (the basis functions) to reconstruct tomographic images of periodically changing samples such as the dynamics of lungs.

## References


[1] Van Nieuwenhove, Vincent and De Beenhouwer, Jan and Vlassenbroeck, Jelle and Moesen, Maarten and Brennan, Mark and Sijbers, Jan, *Registration based SIRT: A reconstruction algorithm for 4D CT*, Online e-journal of nondestructive testing (2017)

[2] Kabus, Sven and Klinder, Tobias and Murphy, Keelin and van Ginneken, Bram and Lorenz, Cristian and Pluim, Josien P, *Evaluation of 4D-CT lung registration*, International Conference on Medical Image Computing and Computer-Assisted Intervention (2009), 747–754.

[3] Hahn, Bernadette, *Efficient algorithms for linear dynamic inverse problems with known motion*, Inverse Problems **30** (2014), 035008

[4] Kazantsev, Daniil and Thompson, William M. and Lionheart, William R. and Van Eyndhoven, Geert and Kaestner, Anders P. and Dobson, Katherine J. and Withers, Philip J. and Lee, Peter D, Inverse problems and imaging, **9** (2015), 447–467

[5] Ritschl, Ludwig and Sawall, Stefan and Knaup, Michael and Hess, Andreas and Kachelrieß, Marc, *Iterative 4D cardiac micro-CT image reconstruction using an adaptive spatio-temporal sparsity prior*, Physics in Medicine & Biology **57** (2012), 1517

[6] Wu, Haibo and Maier, Andreas and Fahrig, Rebecca and Hornegger, Joachim, *Spatial-temporal total variation regularization (STTVR) for 4D-CT reconstruction*, Medical Imaging 2012: Physics of Medical Imaging **8313**, (2012), 83133J

[7] Chambolle, Antonin and Pock, Thoma, *A first-order primal-dual algorithm for convex problems with applications to imaging*, Journal of mathematical imaging and vision **40** (2011), 120–145

[8] Nikitin, Viktor and Carlsson, Marcus and Andersson, Fredrik and Mokso, Rajmund, *Four-dimensional tomographic reconstruction by time domain decomposition*, IEEE Transaction on Computational Imaging **1** (2019)

## Image reconstruction by deep learning and splitting

Xiaoqun Zhang
(joint work with Jiulong Liu and Tao Kuang)

Image reconstruction from downsampled and corrupted measurements, such as fast MRI [1] and CT reconstruction with incomplete data, is mathematically ill-posed inverse problem. Although sparse regularization approaches are largely applied in these kind of problems, it remains challenging to obtain images with high quality. Motivated by recent achievements of deep learning networks for imaging inverse problems, we aim to propose a method utilize neural network for challenging image reconstruction problems. We propose to train a network to learn from intermediate images of classical reconstruction procedure, i.e. the intermediate images that satisfy the data consistence will be fed into some chosen denoising networks or generative networks for removing artifact in each iterative stage. The proposed approach involves only techniques of conventional image reconstruction and usual image representation/denoising deep network learning. Extensive experiments on MRI reconstruction applied with both stack auto-encoder networks and generative adversarial nets demonstrate the efficiency and accuracy of the proposed method compared with other image reconstruction algorithms.

Specifically, we denote the input dataset for a network $\boldsymbol{x} = \{\boldsymbol{x}_k\}_{k=1}^m$ with the corresponding ground truth $\tilde{\boldsymbol{x}} = \{\tilde{\boldsymbol{x}}_k\}_{k=1}^m$ where $m$ is the number of samples. In image reconstruction inverse problems, we denote the corresponding measurements $\boldsymbol{y} = \{\boldsymbol{y}_k\}_{k=1}^m$ for $\boldsymbol{y}_k = A\boldsymbol{x}_k$ where $A$ is a known forward operator. Our idea is to solve the following problem with a deep learning regularization

$$\min_{\boldsymbol{x},\theta} L_H(\boldsymbol{x},\theta) + J(\boldsymbol{x}),$$

$$\max_{\theta_d} \min_{\theta_g,\boldsymbol{x}} L_G(\boldsymbol{x},\theta_g,\theta_d) + J(\boldsymbol{x})$$

where

$$J(\boldsymbol{x}) = \eta(\sum_{i=1}^m \|A\boldsymbol{x}_i - \boldsymbol{y}_i\|_2^2 + \mu\|\mathcal{D}\boldsymbol{x}_i\|_1)$$

and $L_H$ and $L_G$ are the cost function for a denoising network with parameters set $\theta$; and GAN with parameters sets $\theta_g$, $\theta_d$ respectively.

The above model is solved based on ADMM method for variable splitting:

$$\begin{cases} \boldsymbol{z}^{k+1} = \arg\min_{\boldsymbol{z}} J(\boldsymbol{z}) + \frac{\rho}{2}\|\boldsymbol{x}^k - \boldsymbol{z} + \boldsymbol{b}^k\|_2^2 \\ \begin{cases} \theta^{k+1} = \arg\min_{\theta} L_H(\boldsymbol{x}^k,\theta), & \text{(AutoEncoder)}; \\ (\theta_g^{k+1},\theta_d^{k+1}) = \arg\max_{\theta_d}\min_{\theta_g} L_G(\boldsymbol{x}^k,\theta_g,\theta_d), & \text{(GAN)} \end{cases} \\ \boldsymbol{x}^{k+1} = \arg\min_{\boldsymbol{x}} L_H(\boldsymbol{x},\theta^{k+1}) + \frac{\rho}{2}\|\boldsymbol{x} - \boldsymbol{z}^{k+1} + \boldsymbol{b}^k\|_2^2 \\ \boldsymbol{b}^{k+1} = \boldsymbol{b}^k + (\boldsymbol{x}^{k+1} - \boldsymbol{z}^{k+1}) \end{cases}$$

We perform the experiments on MRI reconstruction from downsampled measurements. The MRI data are generated by partial Fourier transform of different

sampling patterns and Gaussian noise corruption. In our experiments, the MRI image dataset is from ADNI (Alzheimer's Disease Neuroimaging Initiative) of which 300 slices of size $192 \times 160$ are used for training and 21 slices are used for inferring. In order to demonstrate the flexibility of our approach, we implement three kinds of networks for MRI reconstruction, i.e. SCAE [2], SNLAE [3] and GAN [4]. Figure 1 presents the results with a 1D random sampling pattern of rate 25%. We observe that in the noise-free case, the reconstructed images by our proposed methods including SCAE, SNLAE and GAN, and by ADMM-net [5] have better spatial resolution and achieve higher PSNR and SSIM. In the case of noise level 10% and with measurements of very low sampling rate, our method with the three networks achieve better performance compared to ADMM-net.

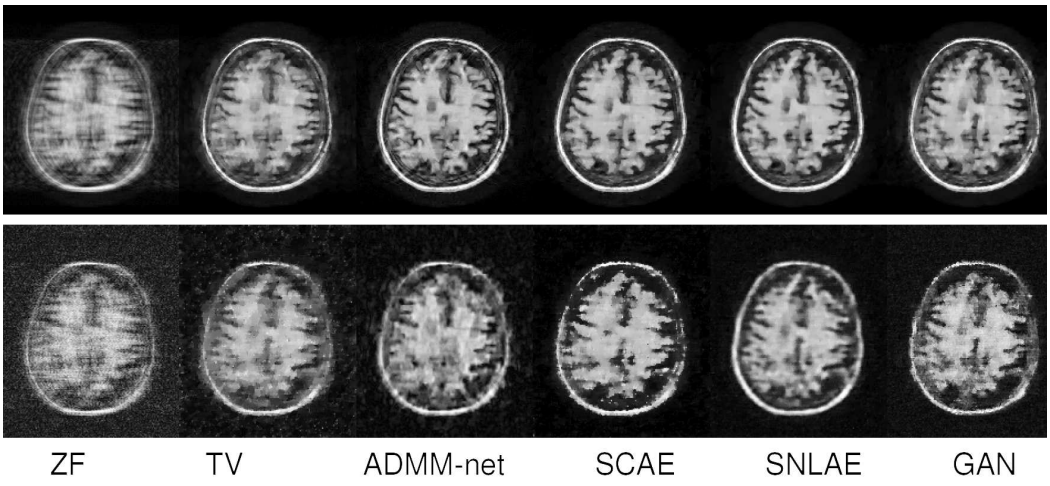


FIGURE 1. MRI reconstruction results. Sampling pattern and rate: 1D random with 25%; The first row: noise free; The second row: 10% noise.

The proposed model is also tested on a low dose CT reconstruction problem. It is demonstrated in Figure 2 that the outer loop iteration reconstruction from 60 noisy (1%) projections of one slice of $192 * 192$ trend to be of better quality and higher PSNR along the iterative regularization.

As a conclusion, we developed a variational image reconstruction method which integrated image representation network and classical iterative image reconstruction. The proposed model exhibits flexibility of choosing classical reconstruction method and powerful deep representation network. The application on MRI image reconstruction showed the effectiveness of the proposed method and it is also clear that the proposed model can be easily extended to other applications.

The main results of this report was published in [6].

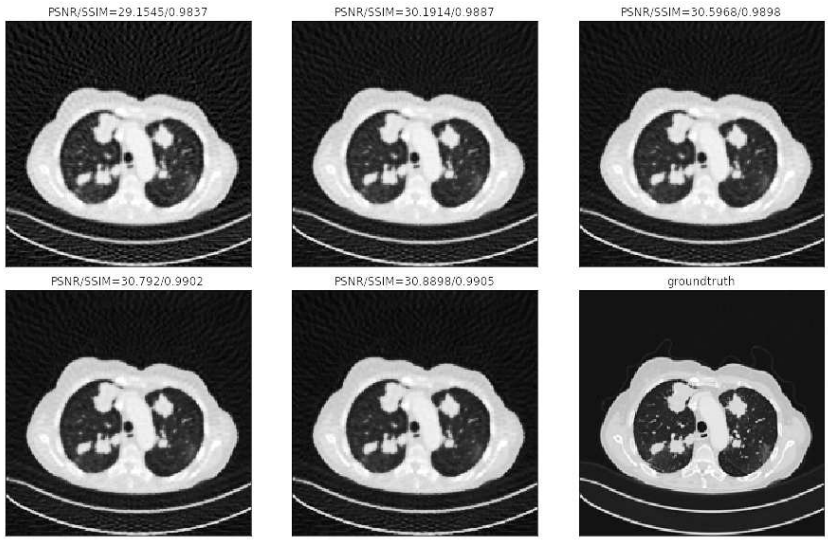


FIGURE 2.

## REFERENCES

[1] M. Lustig, D. Donoho, and J. M. Pauly. Sparse mri: The application of compressed sensing for rapid mr imaging. *Magnetic resonance in medicine*, 58(6):1182–1195, 2007.

[2] J. Masci, U. Meier, D. Cireşan, and J. Schmidhuber. Stacked convolutional auto-encoders for hierarchical feature extraction. In *International Conference on Artificial Neural Networks*, pages 52–59. Springer, 2011.

[3] R. Wang and D. Tao. Non-local auto-encoder with collaborative stabilization for image restoration. *IEEE Transactions on Image Processing*, 25(5):2117–2129, 2016.

[4] I. Goodfellow, J. Pouget-Abadie, M. Mirza, B. Xu, D. Warde-Farley, S. Ozair, A. Courville, and Y. Bengio. Generative adversarial nets. In *Advances in neural information processing systems*, pages 2672–2680, 2014.

[5] J. Sun, H. Li, Z. Xu, et al. Deep admm-net for compressive sensing mri. In *Advances in Neural Information Processing Systems*, pages 10–18, 2016.

[6] J. Liu and T. Kuang and Z. Zhang *Image Reconstruction by Splitting Deep Learning Regularization from Iterative Inversion*, *MICCAI* 2018.

## Electron Tomography

HOLGER KOHR

*Cryogenic Electron Tomography* (cryo-ET) is currently the only imaging technology that yields sub-nanometer resolution 3D images of unstructured biological samples (cells or subcellular structures) in their natural environments. Projection images are acquired by illuminating a ∼100 nm thick sample with a parallel electron beam, using optics to magnify the scattered wavefield, and record incident electrons on a flat detector. Due to the relatively low electron flux, the imaging properties of the microscope can be described in terms of the quantum mechanical interference of *a single electron* with the sample and with itself. In addition, electron sources in modern microscopes have very good monochromaticity: at an acceleration voltage

of 300 kV, the energy spread of electrons is usually less than 0.5 eV. These two properties allow to employ the stationary Schrödinger equation [1]

$$\left(-\frac{\hbar^2}{2m_\mathrm{e}}\Delta + e\,V(\boldsymbol{x})\right)\psi_\mathrm{e}(\boldsymbol{x}) = E_\mathrm{e}\,\psi_\mathrm{e}(\boldsymbol{x}), \quad \boldsymbol{x} = (x, y, z) \tag{1}$$

to describe the interaction of an electron with energy $E_\mathrm{e}$ interacting with the electrostatic potential $V$ describing the specimen.

The trajectory of electrons in a microscope only deviates very little from the vertical axis. This enables a simplification to (1) known as *small angle or paraxial approximation* [1]: The wavefield $\psi_\mathrm{e}$ of the electron can be written as

$$\psi_\mathrm{e}(\boldsymbol{x}) = \psi(\boldsymbol{x})\,\mathrm{e}^{\mathrm{i}kz}, \quad k = \frac{\sqrt{2m_\mathrm{e}E_\mathrm{e}}}{\hbar},$$

with a function $\psi$ that varies slowly in $Z$ direction in the sense that $|\partial^2\psi/\partial z^2| \ll |k\,\partial\psi/\partial z|$. This approximation simplifies (1) to

$$\frac{\partial}{\partial z}\psi = \left(\frac{\mathrm{i}}{2k}\,\Delta' + \mathrm{i}\sigma V\right)\psi, \quad \Delta' = \frac{\partial^2}{\partial x^2} + \frac{\partial^2}{\partial y^2}, \quad \sigma = \frac{m_\mathrm{e}e}{k\hbar^2}. \tag{2}$$

To find a closed form expression for the wavefield at the exit plane of the specimen (called *exit wave*), it is a common assumption that the propagation term $\mathrm{i}/(2k)\,\Delta'\psi$ can be neglected compared to the interaction term $\mathrm{i}\sigma V\psi$. Under this so-called *projection assumption*, (2) can be integrated, yielding

$$\psi(\boldsymbol{x}', z) = \exp\left(\mathrm{i}\,\sigma\int_{-\infty}^{z} V(\boldsymbol{x}', t)\,\mathrm{d}t\right). \tag{3}$$

In other words, under the projection assumption, the total phase shift to the electron wave caused by the specimen is proportional to the *projected potential*

$$PV(\boldsymbol{x}') = \int_{\mathbb{R}} V(\boldsymbol{x}', t)\,\mathrm{d}t \tag{4}$$

described by the ray transform operator $P$.

Finally, for biological samples it is common to assume that this phase shift is small compared to $2\pi$, such that the exit wave can be approximated as

$$\psi(\boldsymbol{x}', z) = 1 + \mathrm{i}\,\sigma\int_{-\infty}^{z} V(\boldsymbol{x}', t)\,\mathrm{d}t. \tag{5}$$

also known as *weak phase object approximation*. For an analysis of the ranges of validity of the various approximations, see [1].

After interacting with the specimen, the electron wave propagates through the magnifying optics and hits the detector, whose pixels record electron events to form an image of the specimen. The quantum mechanical probability density of an electron hitting the detector at a location $\boldsymbol{x}'$ is given by the intensity $|\psi(\boldsymbol{x}', z_\mathrm{d})|^2$ of the wave at the detector plane $z = z_\mathrm{d}$. Using all mentioned approximations, together with free-space propagation of the electron wave and the phase shift

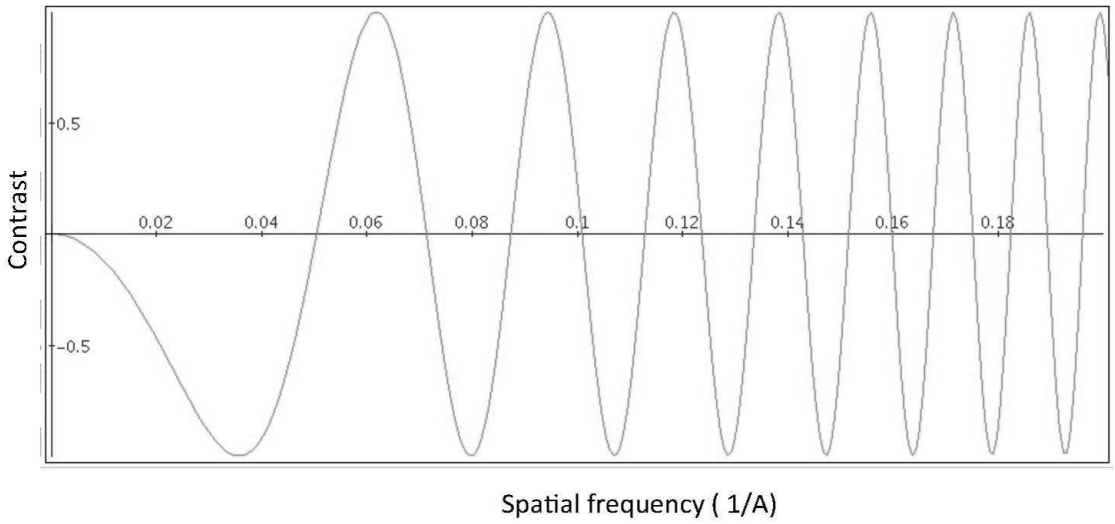


FIGURE 1. Plot of a typical CTF. Image from Wikipedia article "Contrast Transfer Function". License: CC-BY-SA 4.0.

introduced by the lenses, one can identify the term that depends linearly on the projected potential as a convolution

$$p(\boldsymbol{x}') = |\psi(\boldsymbol{x}', z_{\mathrm{d}})|^2 - 1 \approx \big[\mathrm{PSF} * PV\big](\boldsymbol{x}'), \tag{6}$$

with a 2D point spread function whose Fourier transform $\mathrm{CTF}(\boldsymbol{\xi}') = \widehat{\mathrm{PSF}}(\boldsymbol{\xi}')$ is known as *contrast transfer function*. The CTF is a radial function of the form

$$\mathrm{CTF}(\boldsymbol{\xi}') = \sin\left(-\frac{\Delta f}{2k}|\boldsymbol{\xi}'|^2 - \chi(\boldsymbol{\xi}')\right), \tag{7}$$

where $\Delta f$ is the *defocus*, i.e., the amount of underfocus of the objective lens, and $\chi$ is a phase function describing higher-order aberrations [3]. A typical CTF is depicted in Figure 1.

Projection images are finally formed by having many electrons interact with the sample and impinge on the detector, thereby generating many realizations of a random variable distributed according to the probability density $p$ in (6). In cryo-ET, the number of electrons per pixel and projection is typically in the range $20 \sim 40$, resulting in Poisson noise and very low SNR. Finally, tomographic views are gained by rotating the sample around a fixed axis,

$$p(\alpha, \boldsymbol{x}') = \big[\mathrm{PSF} * PV_\alpha(\cdot)\big](\boldsymbol{x}'), \tag{8}$$

where $V_\alpha$ is the electrostatic potential of the specimen rotated by an angle $\alpha$ around the positive $Y$ axis.

A limitation of the CTF model (7) is that it assumes the specimen to be at defocus $\Delta f$ everywhere and thus infinitesimally thin. For thick (more than $\sim$200 nm) or tilted specimens, this has been recognized as a significant limitation, and various adaptions to the CTF model have been suggested to accommodate for this effect. One of the most recent propositions is that of a 3D CTF [3]: by switching the order of projection and 2D convolution in (6), one can introduce

a $z$ dependency in the CTF through a linear offset to the nominal defocus $\Delta f$, resulting in

$$\mathrm{CTF}_{3\mathrm{D}}(\boldsymbol{\xi}', z) = \sin\left(-\frac{\Delta f + z}{2k}|\boldsymbol{\xi}'|^2 - \chi(\boldsymbol{\xi}')\right). \tag{9}$$

With this 3D CTF model, one can derive an analogon to the Fourier slice theorem by taking the Fourier transform of (6). For the 2D CTF model, the Fourier slice theorem states that the Fourier transform of a projection image is equal to a 2D slice of the rotated 3D Fourier transform of the potential $V$ at $\xi_z = 0$, multiplied with the CTF. In contrast, the 3D CTF model yields [3]

$$\widehat{p}(\boldsymbol{\xi}') = \frac{\mathrm{i}}{2}\widehat{V}\left(\boldsymbol{\xi}', -\frac{|\boldsymbol{\xi}'|^2}{2k}\right)\mathrm{e}^{-\frac{\mathrm{i}\Delta f}{2k}|\boldsymbol{\xi}'|^2 - \chi(\boldsymbol{\xi}')} - \frac{\mathrm{i}}{2}\widehat{V}\left(\boldsymbol{\xi}', \frac{|\boldsymbol{\xi}'|^2}{2k}\right)\mathrm{e}^{\frac{\mathrm{i}\Delta f}{2k}|\boldsymbol{\xi}'|^2 + \chi(\boldsymbol{\xi}')}. \tag{10}$$

This relation is closely connected to the corresponding theorem for the Born approximation [4], where the Fourier transform is evaluated on half spheres instead of parabolas. Developing reconstruction methods based on the forward model (10) has the potential to overcome resolution loss due to varying defocus for thick or tilted specimens.

## References


[1] M. Vulović et al, *When to use the projection assumption and the weak-phase object approximation in phase contrast cryo-EM*, Ultramicroscopy **136** (2014).

[2] D. Fanelli and O. Öktem, *Electron tomography: a short overview with an emphasis on the absorption potential model for the forward problem*, Inverse Problems **24** (2008).

[3] L. Voortman et al, *Fast, spatially varying CTF correction in TEM*, Ultramicroscopy **118** (2012).

[4] F. Natterer, *An Error Bound for the Born Approximation*, Inverse Problems **20** (2004).


## Lamé Parameter Estimation from Static Displacement Field Measurements


Ekaterina Sherina

(joint work with Wolfgang Drexler, Simon Hubmer, Lisa Krainz, Andreas Neubauer, Otmar Scherzer and Julian Schmid)


### 1. Introduction

Frequently, one is interested in *quantifying elastic material parameters* of tissues inside an object, which is especially important in Medicine. For instance, palpation is used by medical doctors to detect tissues of abnormal stiffnesses. However, palpation is not quantitative, and moreover, malignant and healthy tissues can feel quite similar. To detect such differences, one uses quantitative elastography. Elastography can be performed on top of any volumetric imaging technique by recording successive images and evaluating the displacement data between the images. Afterwards, it is possible to quantitatively reconstruct the elastic material parameters from the obtained internal displacement data. For an extended

overview on parameter identification and different reconstruction methods in quantitative elastography, see, for example, [1,2] and the references in [3]. In this work, we consider the inverse problem of *quantitative elastography with internal measurements* consisting in estimating the spatially varying *Lamé parameters* from a *single static* displacement field measurement induced by external forces.

## 2. Mathematical Model

We consider the model of *linearized elasticity*, which was chosen in accordance with the physical experiments performed at the Medical University of Vienna (Lisa Krainz, Julian Schmid, Wolfgang Drexler) and which is a valid model for small displacements applied to a sample. Given body forces $f$, applied displacement $g_D$, surface traction $g_T$ and Lamé parameters $\lambda$ and $\mu$, the forward problem of linearized elasticity with displacement-traction boundary conditions consists in finding the internal displacement $u$ satisfying

$$\begin{aligned} -\operatorname{div}(\sigma(u)) &= f\,, \quad \text{in } \Omega\,, \\ u\,|_{\Gamma_D} &= g_D\,, \\ \sigma(u)\vec{n}\,|_{\Gamma_T} &= g_T\,, \end{aligned} \tag{1}$$

where $\vec{n}$ is an outward unit normal vector of $\partial\Omega$ and the stress tensor $\sigma$ defining the stress-strain relation in $\Omega$ is defined by $\sigma(u) := \lambda\ \operatorname{div}(u)\, I + 2\mu\ \mathcal{E}(u)$, where $\mathcal{E}(u) := \frac{1}{2}\left(\nabla u + \nabla u^T\right)$ is called the strain tensor and $I$ is the identity matrix. There exists a unique weak solution of (1). For details, see [3].

## 3. The Inverse Problem

Let the assumptions from [3] hold and let $u^\delta \in L^2(\Omega)^N$ be a measurement of the true displacement field $u$ satisfying $\left\|u - u^\delta\right\|_{L^2(\Omega)} \leq \delta$, where $\delta \geq 0$ is the noise level. Given the model of linearized elasticity (1) in the weak form, the problem is to find the Lamé parameters $\lambda, \mu$. We introduce the parameter-to-solution map

$$\begin{aligned} F : \mathcal{D}(F) := \left\{(\lambda,\mu) \in L^\infty(\Omega)^2 \,|\, \lambda \geq 0\,,\ \mu \geq \underline{\mu} > 0\right\} &\to L^2(\Omega)^N\,, \\ (\lambda,\mu) &\mapsto u(\lambda,\mu)\,. \end{aligned} \tag{2}$$

where $u(\lambda,\mu)$ is the solution of the variational problem, and consider the classical inverse problems theory for solving the nonlinear operator equation $F(\lambda,\mu) = u$. We investigate the Landweber iteration both analytically and numerically. First, we study the forward model operator $F$, and derive the Frèchet derivative and its adjoint, which are needed to implement the Landweber iteration. Then, we verify the *(strong) nonlinearity condition* from [4] in an infinite dimensional setting, which is the basic assumption guaranteeing convergence of Landweber iteration and other iterative regularization methods for solving inverse problems. For the extended analysis and definitions we refer to [3].

## 4. Experimental Data

In the scope of this work, we are interested in estimating the elastic parameters of prepared silicone or agarose gel samples using quantitative elastography, based on dual imaging with Optical Coherence (OCT) and Photoacoustic (PAT) Tomography to investigate the potential of this combined modality.

**Workflow.** We take the two-step approach in solving the problem from experimental data, which consists in calculating the displacement field from successively taken images of the sample using a OCT/PAT imaging system and estimating the Lamé parameters from the derived displacement data. First, a number of samples are prepared from silicone or agarose gel. The samples are different in structure: uniform or layered, with or without inclusion, such that those parts differ in the values of the elastic moduli. Furthermore, all samples are made rotationally symmetric (cylindrical with spherical or cylindrical inclusions). In our experiments, the background substance contains highly light reflective Titanium dioxide particles, and the inclusion is colored by light absorbing Indian ink. The complementary nature of OCT and PAT allows to capture distinct material features. Second, each sample is imaged using a OCT/PAT system before and after compression by a micrometer screw gauge. Then, each 3D dataset is averaged over a number of slices, relying on the axisymmetry of the sample, and a 2D image is obtained. The displacement is calculated from two 2D images using a suitable optical flow algorithm based on the movement of the particles with OCT and of the boundaries with PAT inside the sample.

**Displacement Field**. We made a proof of principle to verify that the model equations indeed describe the experiments. For a uniform sample with known elastic parameters, a sparse displacement field was manually estimated from the brightest large particles on two images from the experiment, and compared to a displacement found by solving the forward problem (1) with the same parameters. A zoomed-in comparison of the two displacement fields is depicted in Figure 1.

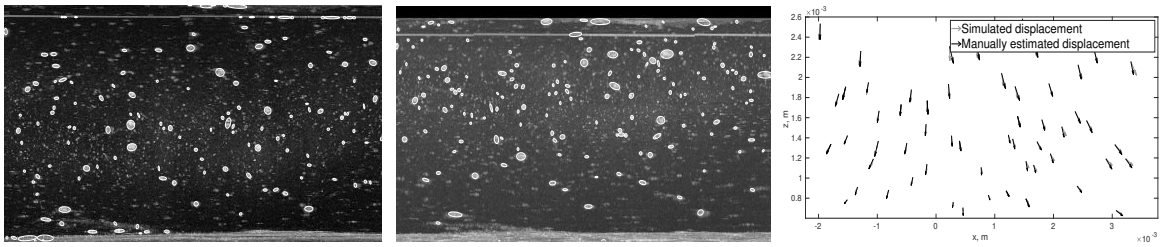


Figure 1. Images of the sample before (left) and after (center) compression. Overlay of displacement fields (right).

## 5. Results

Finally, we present numerical reconstructions of elastic parameters from simulated and experimental data. Examples of reconstructing Lamé parameters from a single noisy displacement field simulated from the forward problem can be found in [3].

One example of reconstructed Lamé parameters from experimental data, obtained from a sample with one spherical inclusion, is depicted in Figure 2.

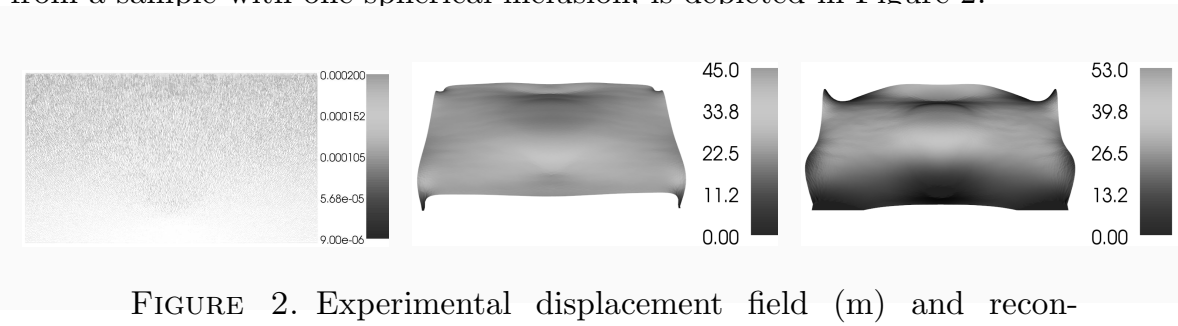


FIGURE 2. Experimental displacement field (m) and reconstructed Lamé parameters $\lambda, \mu$ (kPa).

## REFERENCES

[1] M.M. Doyley, *Model-based elastography: a survey of approaches to the inverse elasticity problem*, Physics in Medicine and Biology **57** (2012), 35–73.

[2] H.T. Banks, S. Hu, Z.R. Kenz, *A Brief Review of Elasticity and Viscoelasticity for Solids*, Advances in Applied Mathematics and Mechanics **3** (2011), 1–51.

[3] S. Hubmer, E. Sherina, A. Neubauer and O. Scherzer, *Lamé Parameter Estimation from Static Displacement Field Measurements in the Framework of Nonlinear Inverse Problems*, SIAM Journal on Imaging Sciences **11** (2018), 1268–1293.

[4] M. Hanke, A. Neubauer, O. Scherzer, *A convergence analysis of the Landweber iteration for nonlinear ill-posed problems*, Numerische Mathematik **72** (1995), 21–37.

## Learned image reconstruction for high-resolution tomographic imaging

ANDREAS HAUPTMANN

(joint work with Jonas Adler, Simon Arridge, Paul Beard, Marta Betcke, Ben Cox, Nam Huynh, Felix Lucka, Vivek Muthurangu and Jennifer Steeden)

Mathematically, the task of reconstructing a tomographic image from measurement data is formulated as an inverse problem: given the unknown (image) of interest $f_{\text{true}} \in X$, the measured data $g \in Y$, and a forward operator $\mathcal{A} : X \to Y$, then the forward problem is modelled by the simple equation

$$g = \mathcal{A}(f_{\text{true}}) + \delta g,$$

where $\delta g \in Y$ denotes some noise in the observation. The inverse problem aims to recover $f_{\text{true}}$ from the measurement of $g$. This is typically an ill-posed task which is conventionally approached through the design of a reconstruction operator based on knowledge of the forward and adjoint mappings and an explicit regularisation. However, in a learning based approach, the idea is to find a mapping $\mathcal{F}_\theta^\dagger$ parametrized by $\theta$ that is simple to design and faster to apply.

In this work we combine conventional and learning based frameworks, and differentiate between two fundamentally different approaches:

i.) Model enforced: Direct reconstruction followed by learning based post-processing. In this approach image reconstruction is carried out using a simple/fast inversion step, and post-processing is used to remove artefacts and noise. In this case we are given a reconstruction operator $\mathcal{A}^\dagger : Y \to X$, then our *inverse mapping* is given by $\mathcal{F}_\theta^\dagger = \mathcal{G}_\theta \circ \mathcal{A}^\dagger$ where $\mathcal{G}_\theta : X \to X$ is typically a sophisticated convolutional neural network (CNN).

ii.) Model based learning and reconstruction: In this approach the forward and adjoint operators of the imaging problem are used directly in the inverse algorithm. Here we learn an iterative update $f_{k+1} = G_\theta(\nabla d(g, \mathcal{A}(f_k)), f_k)$, where $d(g, \mathcal{A}(f_k))$ denotes the data-fit and $G_\theta : X \times X \to X$ is typically a simple CNN.

In the following we present some examples for both approaches, with a specific focus on application to experimental and clinical data.

## 1. Spatio-temporal reconstructions in magnetic resonance imaging

In MRI one obtains the measurement $g$ as the Fourier transform of $f$. Ideally, a stable reconstruction can be obtained by inverse Fourier transformation of fully sampled k-space data, but in cardiac imaging a full k-space sampling can only be obtained during cardiac gated breath-hold and especially sick and very young patients find breath-holding difficult. Thus, real-time sequences with highly undersampled data are required to achieve sufficient acceleration factors ($13\times$ in our application).

As shown in [1] a convolutional neural network is well suited for inverse problems, such as MRI, where the normal operator $\mathcal{A}^*\mathcal{A}$ is of convolutional type. In our study [2], we extend this approach to a 3D (2D plus time) setting and investigate both reconstruction quality, and clinical relevance of the reconstruction.

The specific CNN was trained using synthetic training data created from previously obtained spatio-temporal reconstructions acquired under breath-hold. The trained CNN is then used to reconstruct prospectively acquired real-time, tiny Golden Angle (tGA) radially sampled free breathing data from 10 new patients. Clinical relevance was determined by calculating ventricular volumes from the reconstructed data. Results show that clinical measures of reconstructions from real-time data are not statistically significantly different from gold-standard, cardiac gated, breath-hold techniques and in particular outperform established compressed sensing approaches.

In this setting, the model-enforced approach (i) of reconstruction and post-processing works particularly well due to the additional temporal dimension. The sampling pattern has been chosen, such that aliasing artefacts are incoherent in time and hence appear as noise-like structures over temporal slices. Consequently, the network only needs to learn how to combine the information from each temporal slice and denoise by interpolation in time. In contrast to pure denoising in spatial dimension, where structures need to be recovered from prior information obtained from the training data and hence could lead to a stronger bias in reconstruction.

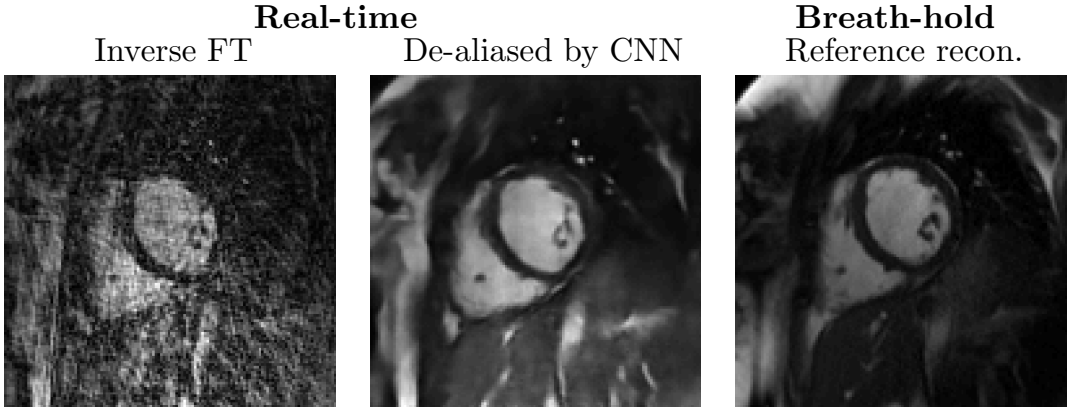


FIGURE 1. Reconstructions of prospectively acquired real-time measurements in comparison to breath-hold reference of the same patient (right)

## 2. Learned iterative reconstruction for limited-view photoacoustic tomography

As discussed in the previous example direct reconstruction and post-processing can perform sufficiently well, but is ultimately limited by the information contained in the initial reconstruction. This limitation will have a considerable influence in limited-view geometries, without temporal information. Motivated by [3] we investigated in [4] a possibility to learn an iterative reconstruction algorithm for 3D high resolution limited-view photoacoustic tomography, following the model-based approach (ii) of learning an iterative reconstruction algorithm.

In this application we consider only the linear part that is typically modeled by the following initial value problem for the wave equation

$$(\partial_{tt} - c^2\Delta)p(\mathbf{x}, t) = 0, \quad p(\mathbf{x}, t = 0) = f(\mathbf{x}), \quad \partial_t p(\mathbf{x}, t = 0) = 0$$

The measurement is then modeled as a linear operator $\mathcal{M}$ acting on the pressure field $p(\mathbf{x}, t)$ restricted to the boundary of the computational domain $\Omega$ and a finite time window: $g = \mathcal{M}\, p_{|\partial\Omega\times(0,T)}$. This defines a linear mapping $\mathcal{A}f = g$ from initial pressure in the domain to time-series on the boundary.

The simulation of the forward operator and its adjoint is computationally demanding and hence, in contrast to [3], learning of the iterative reconstruction algorithm needs to follow a greedy approach, i.e. each iterate is learned separately and to the best possible state given the result of the previous iterate:

$$\min_{\theta_k} \|G_{\theta_k}(\nabla d(g, \mathcal{A}f_k), f_k) - f_{true}\|, \text{ given } f_k = G_{\theta_{k-1}}(\nabla d(g, \mathcal{A}f_{k-1}), f_{k-1}).$$

Additionally, for further improvements in speed we propose in [5] to use a faster, but approximate forward model instead. In particular, when the measurement points lie on a plane ($z = 0$) outside the support of $f$, the pressure there can be related to $f$ by

$$g(x, y, t) = \frac{1}{c^2}\mathcal{F}_{k_x,k_y}\left\{\left\{\mathcal{C}_\omega\left\{B(k_x, k_y, \omega)\tilde{f}(k_x, k_y, \omega)\right\}\right\}\right\}, \tag{1}$$

where $\tilde{f}(k_x, k_y, \omega)$ is obtained from $\hat{f}(\mathbf{k})$ via the dispersion relation $(\omega/c)^2 = k_x^2 + k_y^2 + k_z^2)$ and $\hat{f}(\mathbf{k}) = \mathcal{F}_{\mathbf{x}}\{f(\mathbf{x})\}$ is the 3D Fourier transform of $f(\mathbf{x})$. $\mathcal{C}_\omega$ is a cosine transform from $\omega$ to $t$. The weighting factor, $B(k_x, k_y, \omega)$ contains an integrable singularity which means evaluation on a rectangular grid, so that the FFT can be used to calculate the Fourier transforms efficiently, leads to aliasing in $g(x, y, t)$. To control the degree of aliasing, we set a certain amount of components of $B$ to zero. We then can use Eq. 1, as a fast mapping from the measured data $g$ to an estimate of $f$ and vice versa.

The networks in the iterative reconstruction are trained on a set of segmented lung vessels from human CT scans and with some modifications applied to in-vivo measurements of a human hand. Results show that the iterative approach does outperform post-processing at the cost of longer computations times, but significantly faster than classical iterative schemes. Combined with the fast approximate model, we can achieve a speed-up of factor 32 compared to classical total variation reconstructions.

## References

[1] Kyong Hwan Jin, Michael T McCann, Emmanuel Froustey, and Michael Unser. Deep convolutional neural network for inverse problems in imaging. *IEEE Transactions on Image Processing*, 26(9):4509–4522, 2017.

[2] Andreas Hauptmann, Simon Arridge, Felix Lucka, Vivek Muthurangu, and Jennifer A Steeden. Real-time cardiovascular mr with spatio-temporal artifact suppression using deep learning–proof of concept in congenital heart disease. *Magnetic resonance in medicine*, 81(2):1143–1156, 2019.

[3] Jonas Adler and Ozan Öktem. Solving ill-posed inverse problems using iterative deep neural networks. *Inverse Problems*, 33(12):124007, 2017.

[4] Andreas Hauptmann, Felix Lucka, Marta Betcke, Nam Huynh, Jonas Adler, Ben Cox, Paul Beard, Sebastien Ourselin, and Simon Arridge. Model-based learning for accelerated, limited-view 3-d photoacoustic tomography. *IEEE transactions on medical imaging*, 37(6):1382–1393, 2018.

[5] Andreas Hauptmann, Ben Cox, Felix Lucka, Nam Huynh, Marta Betcke, Paul Beard, and Simon Arridge. Approximate k-space models and deep learning for fast photoacoustic reconstruction. In *International Workshop on Machine Learning for Medical Image Reconstruction*, pages 103–111. Springer, Cham, 2018.

## Decomposition of Dynamic MR Data for Cell Tracking Purposes

Meike Kinzel

(joint work with Martin Burger)

For many clinical applications the tracking of fast dynamics in 4D MR data is of major interest. Since their behavioral observation can help diagnosing even early stages of neural diseases, this also includes the tracking of immune cells in the brain over time. An idea to achieve this goal slicewise is to assume that the single time series are superpositions of background and motion. Considering a matrix

$D \in \mathbb{R}^{nm\times t}$ which consists of $t$ vectorized $n\times m$-images of a time series, this means to impose the relation

$$L + S =: A(L,S) = D, \tag{1}$$

for matrices $L, S \in \mathbb{R}^{nm\times t}$. Additionally assuming $D$ to be corrupted by additive Gaussian noise $\varepsilon \sim N(0,\sigma^2)$, then leads to the model

$$A(L,S) + \varepsilon = D. \tag{2}$$

From a cell tracking point of view one is now interested in finding the matrices $L, S$ which most likely generated a given time series matrix D, respectively in solving the inverse problem. Following the well-established maximum a posteriori approach this can be realized by minimizing a functional $J$ which consists of the Gaussian noise adapted data fidelity term and some prior on the minimizing arguments, namely $L$ and $S$. Taking into account the anticipation of a decomposition into background and motion one can follow the choice of priors introduced by Otazo et al. [1]. Penalizing $L$ by its nuclear norm, this matrix is asked to have a preferably low rank and therefore implicitly forced to have only a few linear independent columns. Since these columns correspond to the images of the time series this involves the prior background information. Simultaneously penalizing $S$ by its 1-norm then allows to apply the prior information on the movement of small cells which are expected to have a sparse vectorized representation in $\mathbb{R}^{nm\times t}$. Thus, the solution of the inverse problem to (2) can be found by minimizing

$$J(L,S) = \frac{1}{2}||L + S - D||_2^2 + \lambda_L||L||_* + \lambda_S||S||_1. \tag{3}$$

Considering only the sparse part $S$ then enables the identification of moving cells.

To directly decompose even raw MR data, Otazo et al. furthermore proposed to proceed analog for a vectorized k-space matrix D and the modified forward operator

$$A(L,S) \coloneqq E(L + S),$$

where E denotes the acquisition operator. This introduces the additional benefit of being able to reconstruct even highly undersampled data.

We present the application of the introduced theory on real data and naturally extend this approach to further decompositions for artifact reduction. Moreover, we discuss the possibility of imposing certain properties on the background respectively the low rank part $L$ by modifying the singular value decomposition via its underlying scalar product.

## References

[1] R. Otazo, E. Candès, D. Sodickson, *Low-rank plus sparse matrix decomposition for accelerated dynamic MRI with separation of background and dynamic components*, Magnetic Resonance in Medicine **73** (2014)

## The Inverse Problem of Magnetorelaxometry Imaging

Janic Föcke
(joint work with Daniel Baumgarten and Martin Burger)

Recently there are several novel techniques in the field of human biology and medicine, that make use of magnetic nanoparticles. These particles have quite unique properties: They are made of two components: a magnetic core and a nonmagnetic shell. The nonmagnetic shell prevent reactions of magnetic core with the surrounding tissue, e.g. rejections or allergic reactions. The magnetic core provides a magnetization for the particles, hence it can be manipulated with the use of external magnetic fields. This behavior is exploited by novel treatment methods as Magnetic Hyperthermia or drug targeting (compare [2] for references). However the presence of the magnetic particles with its properties also let these particles act as a contrast agent. Here Magnetorelaxometry Imaging allows for 2D and 3D reconstruction of the particle distribution.

### 1. The Mechanics of MRXI

Due to its core magnetization, the particles can be aligned by an external magnetic field. This circumstance is used by MRXI in two distinct phases: During the excitation phase an external magnetic field is active. The magnetic particles in the region of interest begin rotating due to its core magnetization. It takes a short period of time until all particles reach a stable, aligned state. Then the relaxation phase is started by switching og the external magnetic fields. Since no external field holds the particles in their aligned state, they start to reorientate in random directions. However, due to magnetization of the core, the particles induce a weak magnetic field. The alignment of the particles amplifies this magnetic field, so it measurable from an external point. After a short period of time all particles are in a random state and no magnetic response is measurable. Both phases define one run of MRXI. To gain spatial information, multiple coils with different position and/or magnetization profiles are activated subsequently.

### 2. Mathematical Model of MRXI

The forward operator model is based on the work of [1, 3] as is translated into a mathematical framework, c.f. [2]. Let $w \in \Omega$ a point in the region of interest $\Omega \subset \mathbb{R}^3$. An activation coil $\alpha = (\varphi_\alpha, I_\alpha)$ is a set of a conductor coil path $\varphi_\alpha$ and a corresponding current $I_\alpha$. The sensors $\sigma = (\sigma_x, \sigma_n)$ consist of a sensor position $\sigma_x$ and a normal $\sigma_n$. Then we define a linear operator $\mathbf{K}_\alpha$ that describes the magnetic response in $\sigma$ for an excitation field $\mathbf{B}_\alpha^{\text{coil}}$ and a underlying particle distribution $c \in \mathbf{L}(\Omega, \mathbb{R}_{\geq 0})$:

$$\mathbf{K}_\alpha \colon c \to \left[ \sigma \to \sigma_n \cdot \int_\Omega \left( \frac{3(\sigma_x - w) \otimes (\sigma_x - w)}{|\sigma_x - w|^5} - \frac{\mathbf{I}}{|\sigma_x - w|^3} \right) \mathbf{B}_\alpha^{\text{coil}}(w)\ c(w)\ dw \right].$$

The classical model for the excitation coil $\mathbf{B}_\alpha^{\text{coil}}$ is defined by the Biot-Savart-Law:

$$\mathbf{B}_\alpha^{\text{coil}} \colon w \to \int_0^{L_\alpha} \varphi_\alpha'(s) \times \left( \frac{w - \varphi_\alpha(s)}{|w - \varphi_\alpha(s)|^3} \right) \, ds$$

where $L_\alpha$ is the length of the parameterized conductor coil $\varphi_\alpha$.

## 3. Idealized Model of MRXI

By approximating the coil loop $\varphi_\alpha(s)$ by its midpoint $y_\alpha$ we introduce an idealized coil, hence

$$\mathbf{B}_\alpha^{\text{coil}} \colon w \to \int_0^{L_\alpha} \varphi_\alpha'(s) \times \left( \frac{w - y_\alpha}{|w - y_\alpha|^3} \right) \, ds = \eta_\alpha \times \left( \frac{w - y_\alpha}{|w - y_\alpha|^3} \right)$$

with $\eta_\alpha = \int_0^{L_\alpha} \varphi_\alpha'(s) \, ds$. It is shown in [2], that this model has an equivalent PDE formulation

$$\mathbf{K} \colon c \to \left[ \sigma \to -16\pi^2 \sigma_n \cdot \nabla_{\sigma_x} U(\sigma_x; y, \eta) \right]$$

where $U(\cdot; y, \eta)$ is the unique solution of

$$-\Delta U = \nabla \cdot (cA)$$

with $A(x) = \eta \times \nabla\gamma(x - y)$ decaying at infinity and $\gamma$ the fundamental solution of the Laplace equation. For a full-field activation of any $y \in \mathcal{O} \subset \mathbb{R}^3 \setminus \Omega$ with two linear independent orientations $\eta_1$ and $\eta_2$ it is shown, that this guarantees a unique solution of the given inverse problem. Finally this property and shown examples promote a random activation scheme.

## References

[1] D. Baumgarten, M. Liehr, F. Wiekhorst, U. Steinhoff, P. Münster, P. Miethe, L. Trahms, J. Haueisen, *Magnetic nanoparticle imaging by means of minimum norm estimates from remanence measurements*, Med. Biol. Eng. Comput. **46** (2008), 1177–85.

[2] J. Foecke, D. Baumgarten, M. Burger, *The inverse problem of magnetorelaxometrz imaging*, Inverse Problems **34** (2018) 115008.

[3] M. Liebl, U. Steinhoff, F. Wiekhorst, J. Haueisen, L. Trahms, *Quantitative imaging of magnetic nanoparticles by magnetorelaxometry with multiple excitation coils*, Phys. Med. Biol. **59** (2014) 6607.

## Towards a mathematical theory of seismic tomography on Mars

Joonas Ilmavirta
(joint work with Maarten V. de Hoop and Vitaly Katsnelson)

The InSight lander brought a seismometer [7] on Mars in late 2018. One of the goals of the mission is to find the interior structure of the planet using a single seismometer to the extent possible. This talk will outline three different methods to reconstruct a radial model of the (upper) mantle for a single ideal seismometer. This is only a small step towards a more complete mathematical understanding of seismic planetary exploration, and a number of new inverse problems arise.

There is a practical need of solving some very hard inverse problems on Mars, and there is a mathematical theory of seismic inverse problems. My goal is to interpolate between these two to take steps towards a mathematical theory of seismic planetary exploration.

The slides of the talk are available on my homepage:
`http://users.jyu.fi/~jojapeil`

### 1. Things we know

In order to prove anything with a single measurement point, we need to make strong structural assumptions. A reasonable leading order assumption is that the planet is spherically symmetric and can therefore be described be wave speeds (different for different polarizations) that depend only on the distance to the center.

Variations in wave speed can be seen as non-Euclidean geometry, where waves — or singularities of solutions to the wave equation — travel along geodesics according to Fermat's principle and distance is measured in travel time. Geometrization in this spirit gives us access to tools in differential geometry. A geometrically convenient assumption on the radial model is that it satisfies the so-called Herglotz condition. The wave speeds in the Preliminary Reference Earth Model [4] satisfy this condition apart from the core–mantle boundary and the vanishing shear wave speed in the liquid outer core. We expect at least the upper mantle of Mars to satisfy the condition.

The problem is to find the wave speed profile from some ideal measurements at a single point. One can use correlations in ambient noise, the spectrum of free oscillations, and meteorite impacts [2]. This gives three ways to find the desired quantity from independent data sets, which gives credibility to conclusions drawn about the Martian mantle from InSight data, whether or not the methods of proof are practically applicable to the real data.

The spectral method is based on a recent result on spectral rigidity in spherical symmetry [3], and upon linearization all three boil down to inverting a certain Abel transform [1]. Abel transforms arise naturally when consider geodesic X-ray and broken ray transforms in spherical symmetry. In a broken ray transform one integrates over rays that reflect on the boundary and potentially other interfaces, and in some situations the rays need to be periodic.

## 2. Things we do not know

Very little can be proven beyond spherical symmetry at this point. A natural approach is to study small lateral inhomogeneities in terms of perturbation theory.

All of the methods mentioned above have to do with travel times of seismic waves, and linearization of travel time leads to ray transforms. However, the geometry is not smooth, and reflections and refractions occur at various interfaces. Therefore it is important to bring the study of geometrical inverse problems to settings with conormal singularities in the geometry itself. Broken ray transforms in a ball with rays reflecting off a core have been analyzed [5, 6], but they assume data everywhere on the surface. The theory of periodic broken ray transforms can currently only deal with very specific geometries, and fundamental geometrical analysis is needed before one can begin to tackle the inverse problems.

Planetary exploration calls for analysis of X-ray transforms with "half-partial data", where the integrals of a function are known over all geodesics with one endpoint in a small open subset of the boundary but the other endpoint is free to vary across the entire boundary. Then one would like to determine the function everywhere, not only close to the small accessible set which corresponds to a measurement array deployed by a lander.

These problems are hard, but only a small sample of the various inverse problems arising in the context of seismology with a single seismometer. A longer problem list can be found in the slides of the talk, and working towards a more complete theory will certainly reveal much more that we ought to solve.

## References

[1] M. V. de Hoop, J. Ilmavirta, *Abel transforms with low regularity with applications to X-ray tomography on spherically symmetric manifolds*, Inverse Problems, 33(12):124003, 2017. Special issue "100 Years of the Radon Transform".

[2] M. V. de Hoop, J. Ilmavirta, *Spectral and travel time tomography on Mars with InSight*, in preparation.

[3] M. V. de Hoop, J. Ilmavirta, V. Katsnelson, *Spectral rigidity for spherically symmetric manifolds with boundary*, preprint 2017.

[4] A. M. Dziewonski, D. L. Anderson, *Preliminary reference earth model*, Physics of the Earth and Planetary Interiors, 25(4):297–356, 1981.

[5] J. Ilmavirta, G. P. Paternain, *Broken ray tensor tomography with one reflecting obstacle*, preprint 2018.

[6] J. Ilmavirta, M. Salo, *Broken ray transform on Riemann surface with a convex obstacle*, Communications in Analysis and Geometry, 24(2):379–408, 2016.

[7] P. Lognonné, W. B. Banerdt, D. Giardini, et al., *SEIS: Insight's Seismic Experiment for Internal Structure of Mars*, Space Science Reviews, 215: 12, 2019.

## Regularized image reconstruction for hyperspectral X-ray and neutron tomography

Jakob S. Jørgensen

(joint work with Daniil Kazantsev, Martin S. Andersen, William R. B. Lionheart, Peter Lee and Philip J. Withers)

We gave an introduction to hyperspectral X-ray and neutron tomography enabled by novel photon-counting detectors with high energy resolution. Such data provides information about characteristic absorption peaks, which may allow one to identify individual materials that conventional detectors cannot distinguish. However, due to few counts the tomography data in each energy channel can be extremely noisy, which prevents simple channelwise reconstruction by conventional methods such as filtered back-projection (FBP).

We presented a novel reconstruction method for hyperspectral tomography, which jointly reconstructs all energy channels using parallel level sets to encourage joint smoothing directions. The proposed method is a generalisation of the parallel level sets method [3] which has been used in bi-modal reconstruction [1, 4, 5] using one known channel as a reference to guide reconstruction of a second unknown channel. Our principal novel idea is to jointly reconstruct multiple unknown channels by selecting reference channels from which to propagate structure in an adaptive and stochastic way while preferring channels with a high data signal-to-noise ratio. The variational reconstruction problem was solved using the Fast Iterative Shrinkage Thresholding Algorithm (FISTA) [2] implemented in MATLAB. Numerical results were shown to demonstrate the performance of the method in comparison with existing spectral CT reconstruction methods, including channelwise total variation and total nuclear variation. Some of the results presented are published in [6].

### References

[1] C. Bathke, T. Kluth, C. Brandt and P. Maaß, *Improved image reconstruction in magnetic particle imaging using structural a priori information*, International Journal on Magnetic Particle Imaging **3** (2017), 1–10.

[2] A. Beck and M. Teboulle, *A fast iterative shrinkage-thresholding algorithm for linear inverse problems*, SIAM Journal on Imaging Science **2** (2009), 183–202.

[3] M. J. Ehrhardt and S. R. Arridge, *Vector-valued image processing by parallel level sets*, IEEE Transactions on Image Processing **23** (2014), 9–18.

[4] M. J. Ehrhardt, K. Thielemans, L. Pizarro, D. Atkinson, S. Ourselin, B. F. Hutton and S. R. Arridge, *Joint reconstruction of PET-MRI by exploiting structural similarity*, Inverse Problems **31** (2014), 015001.

[5] M. J. Ehrhardt and M. M. Betcke, *Multicontrast MRI reconstruction with structure-guided total variation*, SIAM Journal on Imaging Science **9** (2016), 1084–1106.

[6] D. Kazantsev, J. S. Jørgensen, M. S. Andersen, W. R. B. Lionheart, P. Lee and P. J. Withers, *Joint image reconstruction method with correlative multi-channel prior for x-ray spectral computed tomography*, Inverse Problems **34** (2018), 064001.

## Singular artifacts in incomplete data x-ray tomography

Jürgen Frikel
(joint work with Leise Borg, Jakob Sauer Jørgensen and Eric Todd Quinto)

### 1. Introduction

Computed x-ray tomography (CT) is by now on of the standard imaging techniques in many areas, including materials science and medical imaging. Its principle is based on the collection of x-ray measurements along lines that are distributed all around the object and a subsequent reconstruction of an image representing the interior of the object. Such reconstructions can be obtained quite accurately and efficiently by the standard filtered backprojection algorithm (FBP) (cf. [7]) if the data set is complete, i.e., if the measurements are available along all possible lines in the plane.

However, if the data is incomplete, then some features of the original object cannot be reconstructed reliably (are invisible) and artifacts can be generated by the reconstruction algorithm (cf. [7, 10]). This happens in all incomplete data situations, such as limited angle tomography, interior or exterior tomography as well as in new scanning setups as described in [2]. In order to facilitate a proper interpretation of reconstructed images and to understand how the reconstruction procedure can be possibly improved, it is essential to derive precise characterizations of reconstructions for all incomplete data situtations.

In our work we analyze FBP type reconstructions from arbitrary incomplete data and provide characterizations of visible singularities and artifacts using the powerful framework of microlocal anaylsis. The presented results were obtained in our recent work [1] and they generalize characterizations in [3, 5, 8, 10] that primarily analyze the limited angle situation.

### 2. Mathematical setup

As a mathematical model for the measurement process in x-ray CT we consider the Radon transform $R : L^2(\Omega) \to L^2(S^1 \times \mathbb{R})$ that integrates functions $f \in L^2(\Omega)$ (where $\Omega \subset \mathbb{R}^2$ is the closed unit disk) along lines $L(\theta, p)$ that we parametrize by $(\theta, p) \in S^1 \times \mathbb{R}$. That is, $Rf(\theta, p)$ is a line integral representing a measurement along a single x-ray line. In incomplete data CT problems, the measurements $Rf(\theta, p)$ are not available for all $(\theta, p) \in S^1 \times \mathbb{R}$ but only for $(\theta, p) \in A \neq S^1 \times \mathbb{R}$, where $A$ is a proper subset of $S^1 \times \mathbb{R}$. Hence, we model the incomplete data by

$$g_A(\theta, p) = 1_A \cdot Rf(\theta, p),$$

where $1_A$ denotes the characteristic function of $A$.

Since in many practical situations the reconstructions are still obtained through the use of the classical FBP algorithm (cf. [9]), we analyze reconstructions of the form

$$Bg_A = R^* P g_A,$$

where $R^*$ is the backprojection operator ($L^2$-adjoint of $R$) and $P = 1/4\pi\sqrt{-\partial^2/\partial p^2}$ can be interpreted as a filter operator. It is well known that $f = Bg_A = R^*Pg_A$ if the data is complete. However, if the data is incomplete, this equality does not hold.

In order to understand what we reconstruct from incomplete data, we use the notion of the wavefront set provided by the framework of microlocal analysis. Here, the wavefront set $\mathrm{WF}(f)$ of a function (or distribution) $f$ is defined as the set of all singularities of $f$ given by tuples $(x, \xi) \in \mathbb{R}^2 \times (\mathbb{R}^2 \setminus 0)$, where $x$ denotes the location and $\xi$ the direction of a singularity (cf. [4]). In this work, we present characterizations of the wavefront set $\mathrm{WF}(Bg_A)$.

In the formulation of our results we will call a singularity $(x, \xi) \in \mathrm{WF}(f)$ visible if $(x, \xi) \in \mathrm{WF}(f) \cap \mathrm{WF}(Bg_A)$ and invisible if $(x, \xi) \in \mathrm{WF}(f) \setminus \mathrm{WF}(Bg_A)$. If $(x, \xi) \in \mathrm{WF}(Bg_A) \setminus \mathrm{WF}(f)$, the singularity $(x, \xi)$ will be called a singular artifact.

## 3. Main results

The first theorem states a well known paradigm in the mathematical tomography and characterizes visible and invisible singularities of $f$. In particular, it shows that visible singularities correspond to the interior of $A$, $\mathrm{int}(A)$, whereas the invisible singularities correspond to the exterior of $A$, $\mathrm{ext}(A)$.

**Theorem 1** (see, e.g., [1,6,10])**.** *If $(\theta, p) \in \mathrm{int}(A)$, then all singularities of $f$ normal to the line $L(\theta, p)$ are visible (and $Bg_A$ contains no singular artifacts normal to the line $L(\theta, p)$). On the other hand, if $(\theta, p) \in \mathrm{ext}(A)$, then all singularities of $f$ normal to the line $L(\theta, p)$ are invisible.*

The following results characterize (singular) artifacts and show that they arise from boundary points $(\theta, p) \in \mathrm{bd}(A)$. More importantly, they show that singular artifacts can be object-dependent and object-independent, and that they can occur only on lines or curves.

**Theorem 2** ( [1, Theorem 3.7])**.** *Let $(\theta_0, p_0) \in \mathrm{bd}(A)$. Then:*

*(1) If $f$ has a singularity normal to $L(\theta_0, p_0)$, then artifacts can be generated along the line $L(\theta_0, p_0)$ (streak artifact), i.e., $\mathrm{WF}(Bg_A) \setminus \mathrm{WF}(f)$ contains singularities $(x, \xi)$ with locations $x$ that are distributed along the line $L(\theta_0, p_0)$ and the corresponding directions $\xi$ are given by the normals to this line. Such artifacts are generated by a singularity of $f$ and, in this sense, they are object-dependent.*

*(2) If $\mathrm{bd}(A)$ is not smooth at $(\theta_0, p_0)$, then $Bg_A$ can have a streak artifact along $L(\theta_0, p_0)$ independent of $f$. If $Rf(\theta_0, p_0) \neq 0$ and $\mathrm{bd}(A)$ has a corner at $(\theta_0, p_0)$, then $Bg_A$ does have a streak artifact all along $L(\theta_0, p_0)$.*

The previous theorem characterizes the streak artifacts in reconstructions from arbitrary incomplete CT data, and it generalizes the characterizations in [3, 5].

**Theorem 3** ( [1, Theorem 3.5])**.** *Let $(\theta_0, p_0) \in \mathrm{bd}(A)$ and assume $\mathrm{bd}(A)$ is given by the smooth curve $p = p(\theta)$ (with finite slope) near $(\theta_0, p_0)$. If $f$ is smooth normal to $L(\phi_0, p_0)$ and $Rf(\phi_0, p_0) \neq 0$, then an object-independent artifact curve*

*$\theta \mapsto x_b(\theta)$ will appear in $Bg_A$, where*

$$x_b(\theta) = p(\theta)\theta + p'(\theta)\theta^{\perp} .$$

For precise formulations, more details and numerical examples we refer to [1].

## References


[1] L. Borg, J. S. Jørgensen, J. Frikel and E. T. Quinto, *Analyzing reconstruction artifacts from arbitrary incomplete x-ray CT Data*, SIAM J. Imaging Sciences 11.2 (2018), 2786–2814.

[2] L. Borg, J. S. Jørgensen, J. Frikel and J. Sporring, *Reduction of variable-truncation artifacts from beam occlusion during in situ x-ray tomography*, Measurement Science and Technology 28.12 (2017), 124004.

[3] J. Frikel and E. T. Quinto, *Characterization and reduction of artifacts in limited angle tomography*, Inverse Problems 29 (2013), 125007.

[4] L. Hörmander, *The analysis of linear partial differential operators. I*, Distribution theory and Fourier analysis, Reprint of the second (1990) edition [Springer, Berlin], Classics in Mathematics, Springer-Verlag, Berlin, 2003, pp. x+440.

[5] A. I. Katsevich, *Local Tomography for the Limited-Angle Problem*, Journal of Mathematical Analysis and Applications 213.1 (1997), 160–182.

[6] P. Kuchment, K. Lancaster and L. Mogilevskaya, *On local tomography*, Inverse Problems 11 (1995), 571–589.

[7] F. Natterer, *The mathematics of computerized tomography*, Reprint of the 1986 original, Classics in Mathematics 32, Society for Industrial and Applied Mathematics (SIAM), Philadelphia, PA, 2001, pp. xviii+222.

[8] L. V. Nguyen, *How strong are streak artifacts in limited angle computed tomography?*, Inverse Problems 31 (2015), 055003.

[9] X. Pan, E. Y. Sidky and M. Vannier, *Why do commercial CT scanners still employ traditional, filtered back-projection for image reconstruction?*, Inverse Problems 25 (2009), 123009.

[10] E. T. Quinto, *Singularities of the X-ray transform and limited data tomography in $\mathbb{R}^2$ and $\mathbb{R}^3$*, SIAM Journal on Mathematical Analysis 24 (1993), 1215–1225.


## Sonic reflection imaging without low frequencies

Frank Natterer

Our model problem for sonic imaging in the strip $\Omega : \{x \in R^n : 0 \le x_n \le D\}$ is the wave equation

$$\frac{\partial^2 u}{\partial^2 t}(x,t) = c^2(x)(\Delta u(x,t) + \delta(x-s)q(t))$$

$$g_s(x',t) = u(x',D,t)$$

$$c(x) = c_0/(1+f(x)).$$

Here, $n = 2, 3$, $\delta$ is the $n$-dimensional Dirac-function, q is the source wavelet, $D > 0, 0 \le t \le T, x' \in Rn-1, s = (s', D)$ is the source position, $c(x)$ is the speed of sound in $\Omega$ and $c_0$ is the ambient sound speed. What we want to determine from the data function $g_s$ is the speed of sound $c$, i. e. the function $f$.

The emphasis of this talk is on the source wavelet $q$. It has been shown in [3] that the Fourier transform $\hat{f}$ can be determined from reflection data in 2D only outside two circles around $(\pm k, 0)$ touching the origin, $k$ the smallest wavenumber

the presence of which is sufficiently strong in the spectrum of $q$. The resulting difficulties in medical and seismic applications are described in [2], [4], [9]. In [6], [5] it has been shown that the missing low frequency problem can be mitigated by using reflectors. We follow [6] here.

We place a reflector - a simple metal plate - at the lower boundary $x_n = 0$ of $\Omega$ and solve the inverse problem in the Born approximation, following [8]. All we need is the plane wave decomposition of the free space Green's function, see e.g. [7], and the method of images to compute the Green's function for the reflector boundary condition. By numerical examples with the Kaczmarz algorithm we corroborate that such a reflector really compensates for the lack of low frequencies in the source wavelet. A possible applications to ultrasound mammography is suggested in [9].

Finally we consider the special case of layered media. We show by Fourier analysis that the lack of low frequencies can also be compensated for by making the aperture larger. Again numerical results with the Kaczmarz method demonstrate the validity of this approach. This technique is widely used in Falling Weight Deflectometry [1].

## References

[1] Cai, Y. , Pan, E., and Sangghaleh, A.: Inverse calculation of elastic moduli in cross-anisotropic and layered pavements by system identification method, Inverse Problems in Science and Engineering **23**, 717-735 (2015).
[2] Claerbout, J.: Fundamentals of Geophysical Data Processing. McGraw-Hill (1976).
[3] Mora, P.: Inversion = migration + tomography, Geophysics **54**, 1575-1586 (1989).
[4] Minkoff, S. E. and Symes, W. W.: Full waveform inversion of marine reflection data in the plane-wave domain, Geophysics **62**, 540-553 (1997).
[5] Natterer, F.: Ultrasound tomography with a mirror, Phys. Med. Biol. **55** N275-N279 (2010).
[6] Natterer, F.: Reflectors in wave equation imaging, Wave Motion 2008.
[7] Natterer, F. and Wübbeling, F.: Mathematical Methods in Image Reconstruction, p 49. SIAM, Philadelphia (2001)
[8] Nolan, C. J., Cheney, M., Dowling, T., and Gaburro, R.: Enhanced angular resolution from multiply scattered waves, Inverse Problems **22**, 1817-1834 (2006).
[9] Richter, K: Clinical amplitude/velocity reconstructive imaging (CARI) - a new sonographic method for detecting breast lesions, British J. Radiol. **68** 375–384 (1995).

*Reporters: Victoria Hutterer, Meike Kinzel*

# Participants

**Prof. Dr. Gaik Ambartsoumian**
Department of Mathematics
University of Texas at Arlington
P. O. Box 19408
Arlington, TX 76019-0408
UNITED STATES

**Prof. Dr. Simon R. Arridge**
Department of Computer Science
University College London
Gower Street
London WC1E 6BT
UNITED KINGDOM

**Dr. Sebastian Banert**
Department of Mathematics
KTH
100 44 Stockholm
SWEDEN

**Dr. Marta M. Betcke**
Department of Computer Science
University College London
Gower Street
London WC1E 6BT
UNITED KINGDOM

**Prof. Dr. Jan Boman**
Matematiska Institutionen
Stockholms Universitet
106 91 Stockholm
SWEDEN

**Prof. Dr. Christina Brandt**
Department Mathematik
Universität Hamburg
Bundesstrasse 55
20146 Hamburg
GERMANY

**Prof. Dr. Martin Burger**
Department Mathematik
Universität Erlangen-Nürnberg
Cauerstrasse 11
91058 Erlangen
GERMANY

**Prof. Dr. Julianne Chung**
Department of Mathematics
Virginia Tech
Blacksburg, VA 24061-0123
UNITED STATES

**Dr. Matias Courdurier**
Facultad de Matématicas
Pontificia Universidad Católica de Chile
Avda. Vicuna Mackenna 4686, Macul
Estación Central Santiago
CHILE

**Prof. Dr. Laurent Desbat**
TIMC - IMAG
Faculté de Medicine
Université de Grenoble
38706 La Tronche Cedex
FRANCE

**Prof. Dr. David V. Finch**
Department of Mathematics
Oregon State University
Kidder Hall 368
Corvallis, OR 97331-4605
UNITED STATES

**Janic Föcke**
Department Mathematik
Universität Erlangen-Nürnberg
Cauerstrasse 11
91058 Erlangen
GERMANY

**Dr. Lena Frerking**
Philips Research
Forschungslaboratorium Hamburg
Röntgenstrasse 22
22335 Hamburg
GERMANY

**Prof. Dr. Jürgen Frikel**
Department of Computer Science
and Mathematics
OTH Regensburg
Galgenbergstrasse 32
93053 Regensburg
GERMANY

**Dr. Rim Gouia-Zarrad**
Department of Mathematics and
Statistics
College of Arts and Sciences
American University of Sharjah
P.O. Box 26666
Sharjah
UNITED ARAB EMIRATES

**Christine Grathwohl**
Fakultät für Mathematik
Institut für Angewandte und
Numerische Mathematik
Karlsruher Institut für Technologie
(KIT)
Englerstrasse 2
76131 Karlsruhe
GERMANY

**Prof. Dr. Bernadette Hahn**
Mathematisches Institut
Lehrstuhl für Mathematik IX
Universität Würzburg
Am Hubland
97074 Würzburg
GERMANY

**Prof. Dr. Markus Haltmeier**
Department of Mathematics
University of Innsbruck
Technikerstraße 13
6020 Innsbruck
AUSTRIA

**Dr. Andreas Hauptmann**
Department of Mathematics
University College London
Gower Street
London WC1E 6BT
UNITED KINGDOM

**Dr. Victoria Hutterer**
Institut für Industriemathematik
Universität Linz
Altenberger Strasse 69
4040 Linz
AUSTRIA

**Dr. Joonas Ilmavirta**
Department of Mathematics and
Statistics
University of Jyväskylä
P.O. Box 35
40014 Jyväskylä
FINLAND

**Dr. Jiahua Jiang**
Department of Mathematics
Virginia Tech
225 Stanger Street
Blacksburg, VA 24061
UNITED STATES

**Prof. Dr. Ming Jiang**
School of Mathematical Sciences
Peking University
5 Yi He Yuan Street
Beijing 100 871
CHINA

**Dr. Jakob Jorgensen**
School of Mathematics
The University of Manchester
Oxford Road
Manchester M13 9PL
UNITED KINGDOM

**Ajinkya Kadu**
Mathematisch Instituut
Universiteit Utrecht
Budapestlaan 6
P. O. Box 80.010
3508 TA Utrecht
NETHERLANDS

**Prof. Dr. Alexander Katsevich**
Department of Mathematics
University of Central Florida
Orlando, FL 32816-1364
UNITED STATES

**Melina Kienle Garrido**
Fakultät für Mathematik
Universität Würzburg
Emil-Fischer-Strasse 30
97074 Würzburg
GERMANY

**Meike Kinzel**
Institute for Computational and
Applied Mathematics
University of Münster
Orleans-Ring 10
48149 Münster
GERMANY

**Dr. Tobias Kluth**
Fachbereich 3 - Mathematik und
Informatik
Zentrum für Technomathematik
Universität Bremen
Postfach 330 440
28344 Bremen
GERMANY

**Dr. Holger Kohr**
Advanced Technology Group
Materials and Structural Analysis
Division
Thermo Fisher Scientific
5 Achtseweg Noord
5651 GG Eindhoven
NETHERLANDS

**Prof. Dr. Venkateswaran Krishnan**
Tata Institute of Fundamental Research
Centre for Applicable Mathematics
Post Bag No. 6503, GKVK Post Office
Sharada Nagar, Chikkabommasandra
Bengaluru 560 065
INDIA

**Prof. Dr. Arpád Kurusa**
Bolyai Institute
University of Szeged
Aradi Vertanuk Tere 1
6720 Szeged
HUNGARY

**Prof. Dr. Alfred K. Louis**
FR 6.1 - Mathematik
Universität des Saarlandes
66041 Saarbrücken
GERMANY

**Prof. Dr. Peter Maaß**
Fachbereich 3 - Mathematik und
Informatik
Zentrum für Technomathematik
Postfach 330 440
28344 Bremen
GERMANY

**Prof. Dr. Andreas Maier**
Chair of Computer Science 5
(Pattern Recognition)
Universität Erlangen-Nürnberg
Martensstrasse 3
91058 Erlangen
GERMANY

**Prof. Dr. Rajmund Mokso**
MAX IV Laboratory
University of Lund
Box 117
221 00 Lund
SWEDEN

**Prof. Dr. Dr.h.c. Frank Natterer**
Institut für Numerische und
Angewandte Mathematik
Universität Münster
Einsteinstrasse 62
48149 Münster
GERMANY

**Prof. Dr. Richard Nickl**
Statistical Laboratory
Centre for Mathematical Sciences
Wilberforce Road
Cambridge CB3 0WA
UNITED KINGDOM

**Prof. Dr. Eric Todd Quinto**
Department of Mathematics
Tufts University
503 Boston Avenue
Medford, MA 02155
UNITED STATES

**Prof. Dr. Ronny Ramlau**
Industrial Mathematics Institute
Johannes Kepler University
Altenberger Strasse 69
4040 Linz
AUSTRIA

**Annika B. Richter**
Mathematisches Institut
Lehrstuhl für Mathematik IX
Universität Würzburg
Am Hubland
97074 Würzburg
GERMANY

**Prof. Dr. Andreas Rieder**
Fakultät für Mathematik
Institut für Angewandte und
Numerische Mathematik
Karlsruher Institut für Technologie
(KIT)
Englerstrasse 2
76131 Karlsruhe
GERMANY

**Dr. Gaël Rigaud**
Institut für Mathematik, LST X
Universität Würzburg
Emil-Fischer-Strasse 30
97074 Würzburg
GERMANY

**Prof. Dr. Otmar Scherzer**
Institut für Mathematik
Universität Wien
Oskar-Morgenstern-Platz 1
1090 Wien
AUSTRIA

**Prof. Dr. Carola-Bibiane Schönlieb**
Department of Applied Mathematics and
Theoretical Physics (DAMTP)
Centre for Mathematical Sciences
Wilberforce Road
Cambridge CB3 0WA
UNITED KINGDOM

**Prof. Dr. John C. Schotland**
Department of Mathematics
University of Michigan
Ann Arbor, MI 48109-1109
UNITED STATES

**Prof. Dr. Thomas Schuster**
Fachrichtung Mathematik
Universität des Saarlandes
Postfach 151150
66041 Saarbrücken
GERMANY

**Dr. Ekaterina Sherina**
Institut für Mathematik
Universität Wien
Oskar-Morgenstern-Platz 1
1090 Wien
AUSTRIA

**Prof. Dr. Samuli Siltanen**
Department of Mathematics and Statistics
University of Helsinki
P.O. Box 68
00014 University of Helsinki
FINLAND

**Jonas Vogelgesang**
Fakultät für Mathematik und Informatik
Universität des Saarlandes
Postfach 151150
66041 Saarbrücken
GERMANY

**Dr. Anne Wald**
Fakultät für Mathematik und Informatik
Universität des Saarlandes
Postfach 151150
66041 Saarbrücken
GERMANY

**Dr. Qian Wang**
Department of Mathematics
University of Lowell
One University Avenue
Lowell, MA 01854
UNITED STATES

**Prof. Dr. Xiaoqun Zhang**
Institute of Natural Sciences, Rm. 349
Shanghai Jiao Tong University
No. 6 Science Building
800, Dongchuan Road
Shanghai 200 240
CHINA